

DTIC FILE COPY

1

Large-Angle Elastic and Inelastic  
Scattering of  $\pi^+$  and  $\pi^-$   
from  $^{28}\text{Si}$  and  $^{40}\text{Ca}$

by

MICHAEL PAUL SNELL, B.S.

DTIC  
ELECTE  
FEB 22 1990  
S D D

THESIS

Presented to the Faculty of the Graduate School of

The University of Texas at Austin

in Partial Fulfillment

of the Requirements

for the Degree of

MASTER OF ARTS

DISTRIBUTION STATEMENT A

Approved for public release  
Distribution Unlimited

THE UNIVERSITY OF TEXAS AT AUSTIN

May 1989

AD-A218 163

90 02 21 086

**REPORT DOCUMENTATION PAGE**

Form Approved  
OMB No. 0704-0188

1a. REPORT SECURITY CLASSIFICATION <b>UNCLASSIFIED</b>		1b. RESTRICTIVE MARKINGS <b>NONE</b>	
2a. SECURITY CLASSIFICATION AUTHORITY		3. DISTRIBUTION/AVAILABILITY OF REPORT <b>APPROVED FOR PUBLIC RELEASE; DISTRIBUTION UNLIMITED.</b>	
2b. DECLASSIFICATION/DOWNGRADING SCHEDULE		4. PERFORMING ORGANIZATION REPORT NUMBER(S)	
4. PERFORMING ORGANIZATION REPORT NUMBER(S)		5. MONITORING ORGANIZATION REPORT NUMBER(S) <b>AFIT/CI/CIA- 89-083</b>	
6a. NAME OF PERFORMING ORGANIZATION <b>AFIT STUDENT AT UNIV OF TEXAS AT AUSTIN</b>	6b. OFFICE SYMBOL <i>(If applicable)</i>	7a. NAME OF MONITORING ORGANIZATION <b>AFIT/CIA</b>	
6c. ADDRESS (City, State, and ZIP Code)		7b. ADDRESS (City, State, and ZIP Code) <b>Wright-Patterson AFB OH 45433-6583</b>	
8a. NAME OF FUNDING/SPONSORING ORGANIZATION	8b. OFFICE SYMBOL <i>(If applicable)</i>	9. PROCUREMENT INSTRUMENT IDENTIFICATION NUMBER	
8c. ADDRESS (City, State, and ZIP Code)		10. SOURCE OF FUNDING NUMBERS	
		PROGRAM ELEMENT NO.	PROJECT NO.
		TASK NO.	WORK UNIT ACCESSION NO.
11. TITLE (Include Security Classification) <b>(UNCLASSIFIED)</b> <b>Large-Angle Elastic and Inelastic Scattering of <math>\pi^+</math> and <math>\pi^-</math> from <math>^{28}\text{Si}</math> and <math>^{40}\text{Ca}</math></b>			
12. PERSONAL AUTHOR(S) <b>Michael Paul Snell</b>			
13a. TYPE OF REPORT <b>THESIS/DISSERTATION</b>	13b. TIME COVERED FROM _____ TO _____	14. DATE OF REPORT (Year, Month, Day) <b>1989 May</b>	15. PAGE COUNT <b>87</b>
16. SUPPLEMENTARY NOTATION <b>APPROVED FOR PUBLIC RELEASE IAW AFR 190-1 ERNEST A. HAYGOOD, 1st Lt, USAF Executive Officer, Civilian Institution Programs</b>			
17. COSATI CODES		18. SUBJECT TERMS (Continue on reverse if necessary and identify by block number)	
FIELD	GROUP	SUB-GROUP	
19. ABSTRACT (Continue on reverse if necessary and identify by block number)			
20. DISTRIBUTION/AVAILABILITY OF ABSTRACT <input checked="" type="checkbox"/> UNCLASSIFIED/UNLIMITED <input type="checkbox"/> SAME AS RPT. <input type="checkbox"/> DTIC USERS		21. ABSTRACT SECURITY CLASSIFICATION <b>UNCLASSIFIED</b>	
22a. NAME OF RESPONSIBLE INDIVIDUAL <b>ERNEST A. HAYGOOD, 1st Lt, USAF</b>		22b. TELEPHONE (Include Area Code) <b>(513) 255-2259</b>	22c. OFFICE SYMBOL <b>AFIT/CI</b>

TITLE: Large-Angle Elastic and Inelastic Scattering of  $\pi^+$  and  $\pi^-$  from  $^{28}\text{Si}$  and  $^{40}\text{Ca}$

AUTHOR: Michael Paul Snell, B.S., Captain, USAF

DATE: May 1989, 87 pgs

DEGREE: Master of Arts

MAJOR: Physics

INSTITUTION: University of Texas at Austin

ABSTRACT:

*Calcium 40*  
*Si (+) Pi (-)*  
Differential cross sections were measured for  $\pi^+$  and  $\pi^-$  elastic scattering of  $^{40}\text{Ca}$  and  $^{28}\text{Si}$  at incident pion energies ranging from 100 to 260 MeV at a scattering angle of  $175^\circ$ . Differential cross sections were also measured for  $\pi^+$  and  $\pi^-$  inelastic scattering to the  $2^+$ , 1.78 MeV,  $4^+$ , 4.62 MeV, and  $3^-$ , 6.88 MeV states of  $^{28}\text{Si}$  at incident pion energies of 130, 180, and 226 MeV and scattering angles between  $115^\circ$  and  $175^\circ$  in  $6^\circ$  increments. The data are compared to previously obtained forward angle data through  $120^\circ$  and agree quite well. The data show a generally flat angular dependence for angles greater than  $100^\circ$ . Several theoretical codes are reviewed for their ability to predict large angle scattering. Coordinate-space and momentum-space models generally thought to be sufficient for predicting forward angle scattering have proved to be inappropriate for use at large angles. A new phenomenological delta-hole model, currently under modification, shows a greatly enhanced ability to predict scattering at back angles.

90 02 21 086

To Ginger and Casey Jo, for all  
the times I couldn't be around.



Accession For	
NTIS CRA&I	<input checked="" type="checkbox"/>
DTIC TAB	<input type="checkbox"/>
Unannounced	<input type="checkbox"/>
Justification	
By	
Distribution/	
Availability Codes	
Dist	Avail and/or Special
A-1	

## Acknowledgements

First, I thank my advisor, Professor C. Fred Moore, for his help and support during my years as his graduate student. Special thanks go to Dr. Kalvir Dhuga for allowing me to use his experimental data for the subject of this thesis and for his constant help and discussions throughout the analysis of the data and the preparation of this thesis. Also, I thank Dr. Jack Ritchie for his reviewing this thesis and his comments. Extra thanks go to the MP10 staff at Los Alamos for their help in such areas as administration, computing, and housing. My sincerest appreciation to Colonel James Head who, kindly and cleverly, provided me this opportunity to return to my studies. Finally, I should like to extend my appreciation to Allen Williams who told me how things work at Los Alamos and to Dr. Chris Morris who told me how things *ought* to work at Los Alamos.

This thesis is submitted to the Committee on 27 April 1989.

# Contents

<b>1</b>	<b>Introduction</b>	<b>1</b>
<b>2</b>	<b>Experimental Apparatus and Procedure</b>	<b>13</b>
2.1	EPICS Channel and Spectrometer . . . . .	13
2.2	Detector System and Beam Monitoring . . . . .	24
2.3	Data Acquisition and Event Analysis . . . . .	27
<b>3</b>	<b>Data Reduction and Results</b>	<b>36</b>
3.1	Peak Extraction of Missing Mass Spectra . . . . .	36
3.2	Cross Section Calculations . . . . .	38
3.3	Data Presentation . . . . .	48
<b>4</b>	<b>Summary</b>	<b>68</b>
<b>5</b>	<b>Appendix</b>	<b>70</b>
<b>6</b>	<b>References</b>	<b>84</b>

## List of Figures

1	Feynman representation of pion-nucleon interactions using the nucleon and the $\Delta(1232)$ as intermediate states. . . . .	2
2	Total cross sections for $\pi^+p$ , $\pi^-p$ , and $pp$ scattering as a function of lab kinetic energy $T_\pi$ . . . . .	4
3	Fits to the $^{16}\text{O}(\pi^\pm, \pi^\pm)^{16}\text{O}$ angular distributions for $T_\pi = 114$ MeV using various coordinate-space and momentum-space models. . . . .	9
4	Fit to the $^{16}\text{O}(\pi^+, \pi^+)^{16}\text{O}$ angular distribution for $T_\pi = 162$ MeV using a delta-hole model in the local density approximation. . . . .	10
5	Fit to the $^{16}\text{O}(\pi^+, \pi^+)^{16}\text{O}$ angular distribution for $T_\pi = 162$ MeV using a modified delta-hole model in the local density approximation. . . . .	11
6	Experimental Area A of the Los Alamos Meson Physics Facility (LAMPF) facility. . . . .	14
7	A side-on view of the Energetic Pion Channel and Spectrometer (EPICS) at LAMPF. . . . .	16
8	The EPICS channel and its optical mode. . . . .	18
9	Top view of the circular magnet in place in the system. . . . .	19
10	The EPICS spectrometer. . . . .	22
11	Schematic view of the EPICS spectrometer optics and detector system. . . . .	23
12	Assembly view of the EPICS front chamber. . . . .	25

13	Block diagram of the electronics for the EPICS data acquisition system. . . . .	29
14	On-line time-of-flight histogram. . . . .	32
15	On-line $x_{tgt}$ histogram. . . . .	33
16	On-line $y_{tgt}$ histogram. . . . .	34
17	Typical Q-value spectrum. . . . .	35
18	An example of a fit to the Ca data for an incident pion energy of $T_{\pi}=170$ MeV. . . . .	39
19	An example of a fit to the Si data for an incident pion energy of $T_{\pi}=100$ MeV. . . . .	40
20	Acceptance curve for scan of $\delta$ , settings for the pion elastic scattering yield from $^{12}\text{C}$ . . . . .	43
21	Hydrogen normalization curves for $\pi^{-}$ at $\theta_{lab} = 120^{\circ}$ . . . . .	46
22	Hydrogen normalization curves for $\pi^{+}$ at $\theta_{lab} = 130^{\circ}$ and $150^{\circ}$ . . . . .	47
23	Energy distribution of the differential cross sections for $\pi^{+}$ and $\pi^{-}$ elastic scattering from $^{40}\text{Ca}$ at the angle $\theta_{cm} = 175^{\circ}$ . . . . .	50
24	Energy distribution of the differential cross sections for $\pi^{+}$ and $\pi^{-}$ elastic scattering from $^{28}\text{Si}$ at the angle $\theta_{cm} = 175^{\circ}$ . . . . .	51
25	Energy distribution of the differential cross sections for $\pi^{+}$ and $\pi^{-}$ inelastic scattering to the $2^{+}$ , 1.78 MeV excited state of $^{28}\text{Si}$ at the angle $\theta_{cm} = 175^{\circ}$ . . . . .	52
26	Energy distribution of the differential cross sections for $\pi^{+}$ and $\pi^{-}$ inelastic scattering to the $4^{+}$ , 4.62 MeV excited state of $^{28}\text{Si}$ at the angle $\theta_{cm} = 175^{\circ}$ . . . . .	53



27	Energy distribution of the differential cross sections for $\pi^+$ and $\pi^-$ inelastic scattering to the $3^-$ , 6.88 MeV excited state of $^{28}\text{Si}$ at the angle $\theta_{cm} = 175^\circ$ . . . . .	54
28	Angular distribution of the differential cross sections for $\pi^+$ elastic scattering from $^{28}\text{Si}$ at the energy $T_\pi=130$ MeV. . . . .	55
29	Angular distribution of the differential cross sections for $\pi^+$ elastic scattering from $^{28}\text{Si}$ at the energy $T_\pi=180$ MeV. . . . .	56
30	Angular distribution of the differential cross sections for $\pi^+$ elastic scattering from $^{28}\text{Si}$ at the energy $T_\pi=226$ MeV. . . . .	57
31	Angular distribution of the differential cross sections for $\pi^+$ inelastic scattering to the $2^+$ , 1.78 MeV level of $^{28}\text{Si}$ at the energy $T_\pi=130$ MeV. . . . .	58
32	Angular distribution of the differential cross sections for $\pi^+$ inelastic scattering to the $2^+$ , 1.78 MeV level of $^{28}\text{Si}$ at the energy $T_\pi=180$ MeV. . . . .	59
33	Angular distribution of the differential cross sections for $\pi^+$ inelastic scattering to the $2^+$ , 1.78 MeV level of $^{28}\text{Si}$ at the energy $T_\pi=226$ MeV. . . . .	60
34	Angular distribution of the differential cross sections for $\pi^+$ inelastic scattering to the $4^+$ , 4.62 MeV level of $^{28}\text{Si}$ at the energy $T_\pi=130$ MeV. . . . .	62
35	Angular distribution of the differential cross sections for $\pi^+$ inelastic scattering to the $4^+$ , 4.62 MeV level of $^{28}\text{Si}$ at the energy $T_\pi=180$ MeV. . . . .	63

36	Angular distribution of the differential cross sections for $\pi^+$ inelastic scattering to the $4^+$ , 4.62 MeV level of $^{28}\text{Si}$ at the energy $T_\pi=226$ MeV. . . . .	65
37	Angular distribution of the differential cross sections for $\pi^+$ inelastic scattering to the $3^-$ , 6.88 MeV level of $^{28}\text{Si}$ at the energy $T_\pi = 130$ MeV. . . . .	66
38	Angular distribution of the differential cross sections for $\pi^+$ inelastic scattering to the $3^-$ , 6.88 MeV level of $^{28}\text{Si}$ at the energy $T_\pi = 180$ MeV. . . . .	67
39	Angular distribution of the differential cross sections for $\pi^+$ inelastic scattering to the $3^-$ , 6.88 MeV level of $^{28}\text{Si}$ at the energy $T_\pi = 226$ MeV. . . . .	68

## List of Tables

1	EPICS channel specifications. . . . .	18
2	EPICS channel beam pion flux and composition. . . . .	21
3	EPICS spectrometer specifications. . . . .	25
4	Tabular values of the measured and calculated parameters used to determine the acceptance curve. . . . .	72
5	Tabular values of the measured and calculated parameters used to determine the hydrogen normalization curves. . . . .	73
6	Tabular values of the measured and calculated parameters used to determine an energy distribution of the differential cross sections for $\pi^+$ and $\pi^-$ elastic scattering from $^{40}\text{Ca}$ . . . .	74
7	Tabular values of the measured and calculated parameters used to determine an energy distribution of the differential cross sections for $\pi^+$ and $\pi^-$ elastic scattering from $^{28}\text{Si}$ . . . .	75
8	Tabular values of the measured and calculated parameters used to determine an energy distribution of the differential cross sections for $\pi^+$ and $\pi^-$ inelastic scattering to the $2^+$ , 1.78 MeV state of $^{28}\text{Si}$ . . . . .	76
9	Tabular values of the measured and calculated parameters used to determine an energy distribution of the differential cross sections for $\pi^+$ and $\pi^-$ inelastic scattering to the $4^+$ , 4.62 MeV state of $^{28}\text{Si}$ . . . . .	77

10	Tabular values of the measured and calculated parameters used to determine an energy distribution of the differential cross sections for $\pi^+$ and $\pi^-$ inelastic scattering to the $3^-$ , 6.88 MeV state of $^{28}\text{Si}$ . . . . .	78
11	Tabular values of the measured and calculated parameters used to determine an angular distribution of the differential cross sections for $\pi^+$ elastic scattering and inelastic scattering to the $2^+$ , 1.78 MeV state of $^{28}\text{Si}$ at $T_\pi=130$ MeV. . . . .	79
12	Tabular values of the measured and calculated parameters used to determine an angular distribution of the differential cross sections for $\pi^+$ inelastic scattering to the $4^+$ , 4.62 MeV and $3^-$ , 6.88 MeV states of $^{28}\text{Si}$ at $T_\pi=130$ MeV. . . . .	80
13	Tabular values of the measured and calculated parameters used to determine an angular distribution of the differential cross sections for $\pi^+$ elastic scattering and inelastic scattering to the $2^+$ , 1.78 MeV state of $^{28}\text{Si}$ at $T_\pi=180$ MeV. . . . .	81
14	Tabular values of the measured and calculated parameters used to determine an angular distribution of the differential cross sections for $\pi^+$ inelastic scattering to the $4^+$ , 4.62 MeV and $3^-$ , 6.88 MeV states of $^{28}\text{Si}$ at $T_\pi=180$ MeV. . . . .	82
15	Tabular values of the measured and calculated parameters used to determine an angular distribution of the differential cross sections for $\pi^+$ elastic scattering and inelastic scattering to the $2^+$ , 1.78 MeV state of $^{28}\text{Si}$ at $T_\pi=226$ MeV. . . . .	83

16 Tabular values of the measured and calculated parameters used to determine an angular distribution of the differential cross sections for  $\pi^+$  inelastic scattering to the  $4^+$ , 4.62 MeV and  $3^-$ , 6.88 MeV states of  $^{28}\text{Si}$  at  $T_\pi=226$  MeV. . . . . 84

# 1 Introduction

In 1935, Yukawa, who was studying the strong interactions in nuclear and particle physics, suggested that the strong nuclear binding forces would be mediated by the virtual exchange of a particle whose mass lies midway between that of the electron and that of the proton [Yu-35]. This mass was estimated from the range of the nucleon-nucleon interaction, and the particle has come to be known as the  $\pi$ -meson or *pion*. Since its detection in 1947 [La-47] and subsequent production in 1948 at the University of California Radiation Laboratory [Ga-48] the pion has been used extensively as a hadronic probe in experimental nuclear physics. This work is primarily being performed at three currently existing "meson factories": the Tri-University Meson Physics Facility (TRIUMF) in Canada, the Swiss Institute for Nuclear Research (SIN) in Switzerland, and the Los Alamos Meson Physics Facility (LAMPF) in the United States.

The pion is a spin zero, isospin one ( $J^{\pi} = 0^{-}, T = 1$ ) particle existing in three charge states. The  $\pi^{+}$  and  $\pi^{-}$  have a mass of 139.6 MeV while the  $\pi^{0}$  has a mass of 135.0 MeV. This makes the pion the lightest known strongly interacting particle, and, as a boson, can be absorbed or created in nuclear interactions (which is intrinsic to its role as a mediator of the nuclear force). The pion's many attributes make it a most interesting and useful probe of nuclear research allowing for the corroboration of data found with other probes as well as providing experimental results unobtainable by other, more conventional probes.

The first of these properties has already been alluded to, that being its existence in three charge states. From this, the comparison of  $\pi^+$  and  $\pi^-$  interactions provides an exceptional means of verifying the accuracy of descriptions of Coulomb distortion effects in the scattering of hadrons from nuclei. Because of the different charge states pions can also be used in single-charge-exchange (SCX) and double-charge-exchange (DCX) scattering experiments, the latter of which can lead to nuclear levels with  $T$  and  $T_z$  values unobtainable with  $T = \frac{1}{2}$  hadronic probes such as protons.

Because the pion can be absorbed by the nucleus we can study the differences in neutron and proton distributions in the nucleus yielding useful information about nucleon correlations within the nucleus. This sensitivity arises because of the difference in the isospin structure of the  $\pi^+p(\pi^-n)$  and  $\pi^+n(\pi^-p)$  systems. The pion's light mass also makes the theoretical treatment of pion-nucleus scattering much easier in that recoil effects, projectile structure, and projectile-target particle exchange are not as important nor as difficult to handle as in other hadron-nucleus interactions.

There is yet another attribute the pion possesses that make it a most attractive nuclear probe, that being the production of baryon resonances during the interaction process. These *resonances* represent short-lived quantum-mechanical bound states of one or more fundamental particles. Figure 1 shows a diagram of various pion-nucleon interactions using as intermediate states both the nucleon and one of the most prominent of these pion-induced resonances, the  $\Delta(1232)$ . Consider Figure 2, which shows a summary of measured total cross sections for  $\pi^\pm p$  as a function of the kinetic energy of

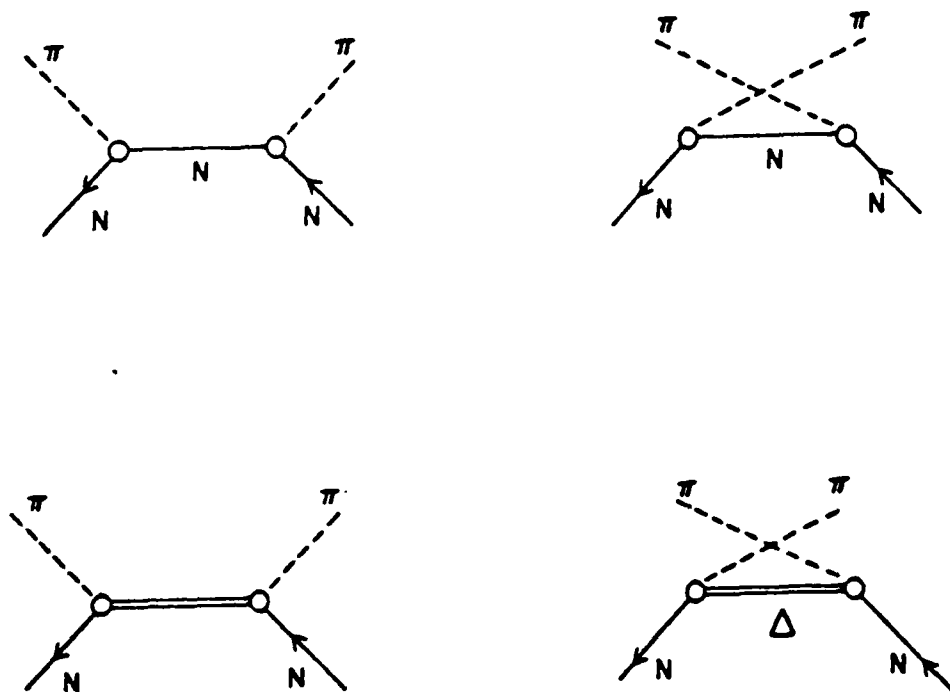


Figure 1: Feynman representation of pion-nucleon interactions using the nucleon and the  $\Delta(1232)$  as intermediate states [Ei-80].



the incident pion,  $T_\pi$  within the energy range  $0 < T_\pi < 2$  GeV [Ba-68]. This figure also contains the pp interaction cross section for comparison and thus exhibits the difference between the  $\pi$ N interaction and the nucleon-nucleon interaction. This difference is especially prominent in the region  $100 < T_\pi < 300$  MeV where the spectrum is dominated by a resonance which occurs when the phase shift of the  $l = 1$  ( $p$ -wave),  $J = \frac{3}{2}$ ,  $T = \frac{3}{2}$  partial wave rises through  $90^\circ$  at  $T_\pi = 195$  MeV. (By decomposing the differential cross sections into partial waves the resonances displayed in the spectra are represented by phase shifts, the largest of which is the shift described above.) The notation for this resonance (in the form  $P_{2T,2J}$ ) is  $P_{3,3}$  and corresponds to a pion-proton mass of 1232 MeV. Hence, the resonant state  $\Delta(1232)$  represents an unstable particle which decays into  $\pi + N$  in a  $P_{33}$  wave.

The  $\Delta(1232)$  resonance plays an important role in pion-nucleus scattering. Theoretical descriptions of pion-nucleus elastic and inelastic scattering, where one treats nuclear transitions in the Born approximation, involves the basic pion-nucleon interaction. Therefore, the energy, spin, and isospin dependences of the pion-nucleus interaction result from the energy, spin, and isospin dependences of the pion-nucleon interactions, which is dominated by the formation of the  $\Delta(1232)$  resonance. So, to understand the role of the pion as a probe of nuclear structure we must know something of pion-nucleus scattering in the region of this resonance.

The center-of-mass *differential cross section* for unpolarized elastic scat-

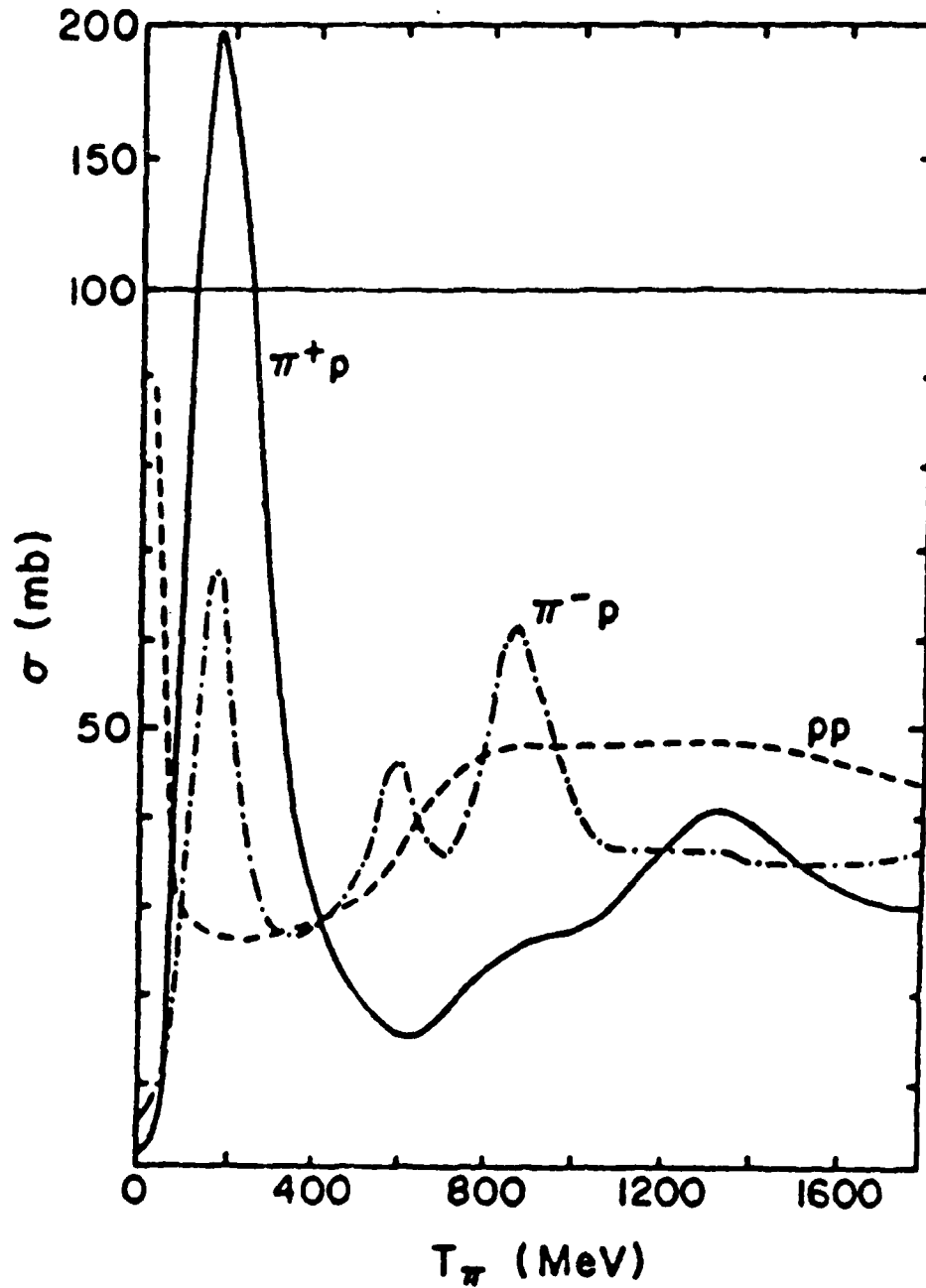


Figure 2. Total cross sections for  $\pi^+p$  (solid line) and  $\pi^-p$  (dot-dashed line) scattering as a function of lab kinetic energy  $T_\pi$ . For comparison the total  $pp$  cross section (dashed line) [He-58] is shown. Note change in vertical scale.

tering is given by [Ei-80]

$$\frac{d\sigma}{d\Omega} = \frac{1}{2} \sum_{\text{spins}} |f_{\beta\alpha}|^2 \quad (1)$$

where the sum is over the spin projections of the nucleon in the initial and final states. We also define,  $f_{\beta\alpha}$ , the *elastic scattering amplitude* as

$$f_{\beta\alpha} = -(2\pi)^2 m T_{ba} \equiv -\frac{m}{2\pi} \langle \mathbf{p}', \beta | T | \mathbf{p}, \alpha \rangle \quad (2)$$

where  $m$  is the reduced mass for the meson and nucleon and  $\mathbf{p}'$ ,  $\mathbf{p}$  are the initial and final pion momenta. Invariance under rotations in space and parity limit the form of  $f_{\beta\alpha}$  to

$$f_{\beta\alpha}(E, \hat{\mathbf{p}}, \hat{\mathbf{p}}') = f(E, \theta) + g(E, \theta) i \boldsymbol{\sigma} \cdot \mathbf{n} \quad (3)$$

where  $\boldsymbol{\sigma}$  are the Pauli spin matrices,  $\theta$  is the angle between  $\hat{\mathbf{p}}$  and  $\hat{\mathbf{p}}'$ , and  $\mathbf{n}$  is the vector

$$\mathbf{n} = \frac{(\mathbf{p} \times \mathbf{p}')}{|\mathbf{p} \times \mathbf{p}'|}.$$

The differential cross section can now be written as

$$\frac{d\sigma}{d\Omega}(E, \theta) = |f(E, \theta)|^2 + |g(E, \theta)|^2. \quad (4)$$

The amplitude in Eqn. 3 can be expanded in partial waves by expanding the functions  $f$  and  $g$  separately as

$$\begin{aligned} f(E, \theta) &= \sum_{l=0}^{\infty} [(l+1)f_{l+}(E) + lf_{l-}(E)] P_l(\cos \theta) \\ g(E, \theta) &= \sum_{l=0}^{\infty} [f_{l+}(E) - f_{l-}(E)] P'_l(\cos \theta) \sin \theta \end{aligned} \quad (5)$$

in terms of the Legendre functions  $P_l(x)$ ,  $x = \cos \theta$ , and their  $x$ -derivatives  $P'_l(x) = (d/dx)P_l(x)$ . The partial-wave amplitudes are defined for orbital angular momentum  $l$  and total angular momentum  $J = l \pm \frac{1}{2}$  of the pion-nucleon system. The function  $f_{l\pm}(E)$  is expressed in terms of two *real* quantities: the phase shift  $\delta_{l\pm}(E)$  and the inelasticity parameter  $\eta_{l\pm}(E)$ , in the form

$$f_{l\pm}(E) = \frac{(\eta_{l\pm}(E) \exp 2i\delta_{l\pm}(E) - 1)}{2ip}. \quad (6)$$

For purely elastic scattering  $\eta = 1$  and is  $0 \leq \eta < 1$  otherwise.

As mentioned previously, for  $100 \leq T_\pi \leq 300$  MeV, pion-nucleon scattering is dominated by the  $\Delta(1232)$  resonance, thus the largest phase shift in this energy range is  $\delta_{3,3}^1$ . Therefore, from Eqn. 4 we can write differential cross sections for  $\pi^\pm p$  elastic and SCX scattering as

$$\begin{aligned} \frac{d\sigma}{d\Omega}(\pi^+ p \rightarrow \pi^+ p) &= (4 \cos^2 \theta + \sin^2 \theta) |\alpha_{3,3}^1|^2, \\ \frac{d\sigma}{d\Omega}(\pi^- p \rightarrow \pi^- p) &= \frac{1}{9} (4 \cos^2 \theta + \sin^2 \theta) |\alpha_{3,3}^1|^2, \\ \frac{d\sigma}{d\Omega}(\pi^+ p \rightarrow \pi^0 n) &= \frac{2}{9} (4 \cos^2 \theta + \sin^2 \theta) |\alpha_{3,3}^1|^2, \end{aligned} \quad (7)$$

where  $\alpha_{3,3}^1$  is the partial-wave amplitude. These cross sections lead us to some important cross section ratios, namely

$$\begin{aligned} \frac{\sigma_T(\pi^+ p)}{\sigma_T(\pi^- p)} &= 3, \\ \frac{\sigma(\pi^+ p)}{\sigma(\pi^- p)} &= 9, \\ \frac{\sigma(\pi^+ p)}{\sigma(\text{SCX})} &= \frac{9}{2}. \end{aligned} \quad (8)$$

These ratios are in agreement with the experimental total cross sections shown in Fig. 2 and other pion-nucleon data taken at energies near the peak of the  $\Delta(1232)$  resonance. So if we assume that only the  $\alpha_{3,3}^1$  partial-wave amplitude contributes to pion-nucleon scattering in this energy range, then using this regional dominance we can obtain simple, transparent expressions for pion-nucleus scattering.

Over the past several years many theoretical models have been developed for describing pion-nucleus scattering. These models most generally fall into one of three categories. The first of these categories contains various models calculated in coordinate space and making use of the assumption that the pion-nucleon interaction can be very closely approximated by a zero-range interaction. Most of these models find their roots in an approach developed by Kisslinger [Ki-55] which has served as the basis for the majority of the phenomenological work in the field. A second type of model utilizes a microscopic momentum-space approach which includes an exact treatment of relativistic kinematics, an improved treatment of dispersive effects, and exact performance of the Fermi-averaging integral [Jo-83, Li-79]. This last feature allows for exact calculation of the formation, propagation, and decay of the delta.

These two types of models differ from the third model, the delta-hole approach [Hi-77, Le-82], in that the phenomenology is incorporated through higher-order terms in the multiple-scattering theory rather than a phenomenological delta-hole interaction. The delta-hole model *assumes* that the dominant mode of interaction of a pion with the nucleus is to excite a nucleon to

a delta, with a corresponding hole in the nucleon state. The influence of the nuclear medium on the  $\pi N\Delta$  vertex and on the delta itself is then treated. It is this model that has recently achieved the most success at describing a variety of data from pion-nucleus interactions.

While all three models have had great success at accurately describing pion-nucleus scattering at forward angles, i.e.  $0^\circ \leq \theta < 90^\circ$ , none have been able to reproduce such results at larger angles, i.e.  $90^\circ \leq \theta < 180^\circ$ . Indeed, for scattering at backward angles these models give strongly divergent predictions. Figure 3 shows a comparison of theoretical predictions employing several coordinate-space and momentum-space models of varying degrees of sophistication [Dh-85]. The experimental data shown in the figure is a composite of forward-angle data [Al-80, In-78] and backangle data [Dh-85] of  $\pi^+$  and  $\pi^-$  scattering from  $^{16}\text{O}$  at 114 MeV. Calculations with coordinate-space models such as PIRK [Ei-74, Co-80], shown in Fig. 3(a) and PIESDEX 1 and 2 [Gr-84], shown in Fig. 3(b) and (c), are totally inadequate at large angles. The first- and second-order field-theoretic momentum-space models [Jo-83], shown in Fig. 3(d) and (e), give an improved, yet still inadequate, representation. A second momentum-space model [Li-79], shown in Fig. 3(f), while accurate through  $120^\circ$ , fails like the rest at very large angles.

Figures 4 and 5 show the results for  $\pi^+$  elastic scattering from  $^{16}\text{O}$  at 162 MeV and its comparison to a local density approximation to the delta-hole model [Ka-86], and a modification of that model which includes many of the features that have been included in the momentum-space approaches [Dh-88]. One sees that while the first model gives an excellent fit to the data

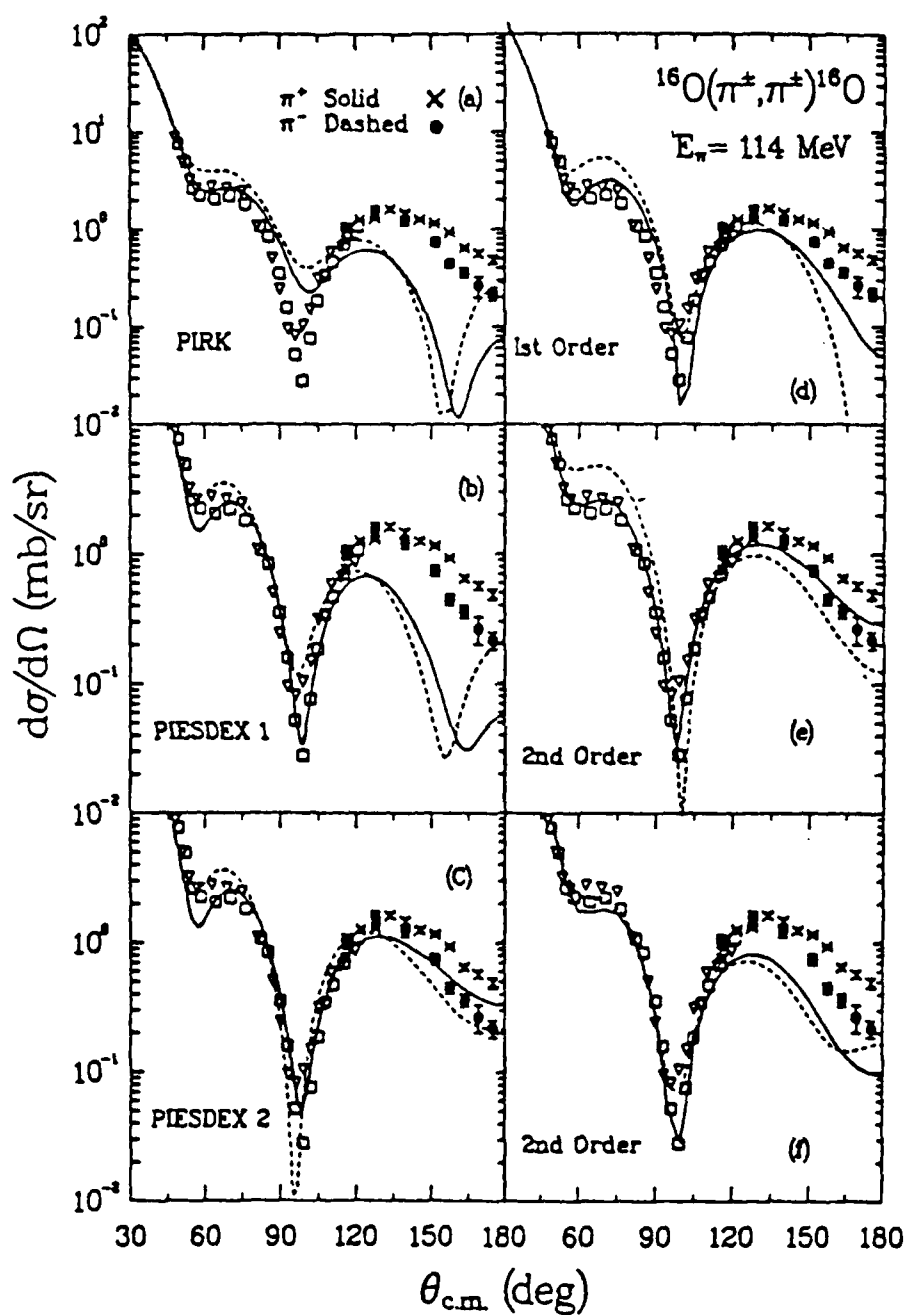


Figure 3: Fits to the  $^{16}\text{O}(\pi^\pm, \pi^\pm)^{16}\text{O}$  angular distributions for  $T_\pi = 114$  MeV using various coordinate-space and momentum-space models as described in the text. (a) [Co-80], (b) and (c) [Gr-84], (d) and (e) [Jo-83], (f) [Li-79].

in the forward angles it suffers badly at backangles. The improvements made in the second model help greatly in the backangle predictions, however they also introduce disagreement around the minimum at  $90^\circ$ .

Only a few experiments have been performed where pion-nucleus scattering cross sections have been measured at large angles in this energy region [Ba-82, Ch-79] and thus, very little is known about large angle scattering phenomena. It is then important to measure backangle scattering because the mechanisms are often quite different from those responsible for forward scattering. While forward scattering is primarily diffractive, other mechanisms may become apparent at backward angles, such as important off-shell effects, where the diffractive contribution is small. In addition, large angle scattering is often a very stringent test for theoretical models. Therefore, if we are to continue to modify theoretical models such that we have a better understanding of the scattering process it is necessary to acquire much more data at large angles than is now available.

Section 2 of this thesis describes the experimental facility and procedure used to acquire the data. Section 3 describes the extraction of differential cross sections from the various missing mass spectra. This chapter also contains the presentation of the data acquired which consists of the first detailed measurements of: (1) energy distributions of large-angle  $\pi^\pm$  elastic scattering from  $^{40}\text{Ca}$  at  $175^\circ$ , (2) energy distributions of large-angle ( $115^\circ \leq \theta \leq 175^\circ$ )  $\pi^\pm$  elastic and inelastic scattering (first three excited states) from  $^{28}\text{Si}$  at  $175^\circ$ , and (3) angular distributions of large-angle  $\pi^\pm$  elastic and inelastic scattering (first three excited states) from  $^{28}\text{Si}$  at energies  $T_\pi = 130, 180, 226$  MeV.



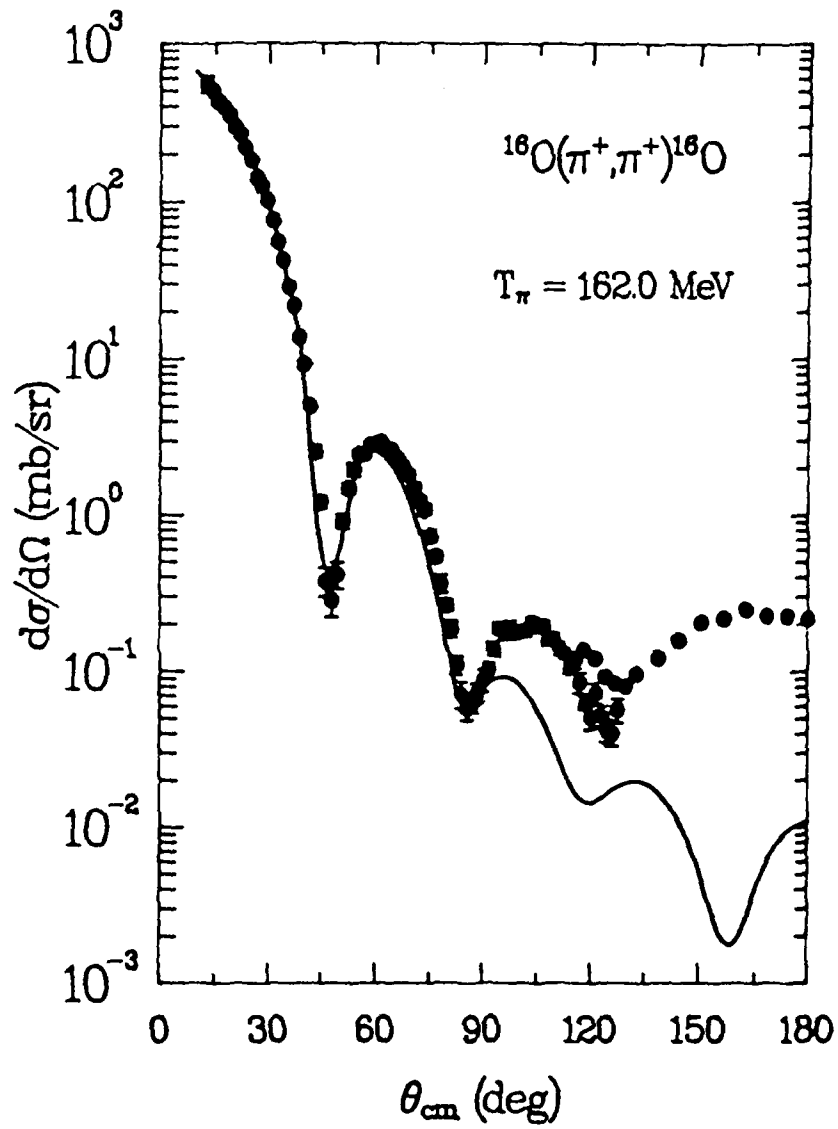


Figure 4: Fit to the  $^{16}\text{O}(\pi^+, \pi^+)^{16}\text{O}$  angular distribution for  $T_\pi = 162 \text{ MeV}$  using a delta-hole model in the local density approximation.

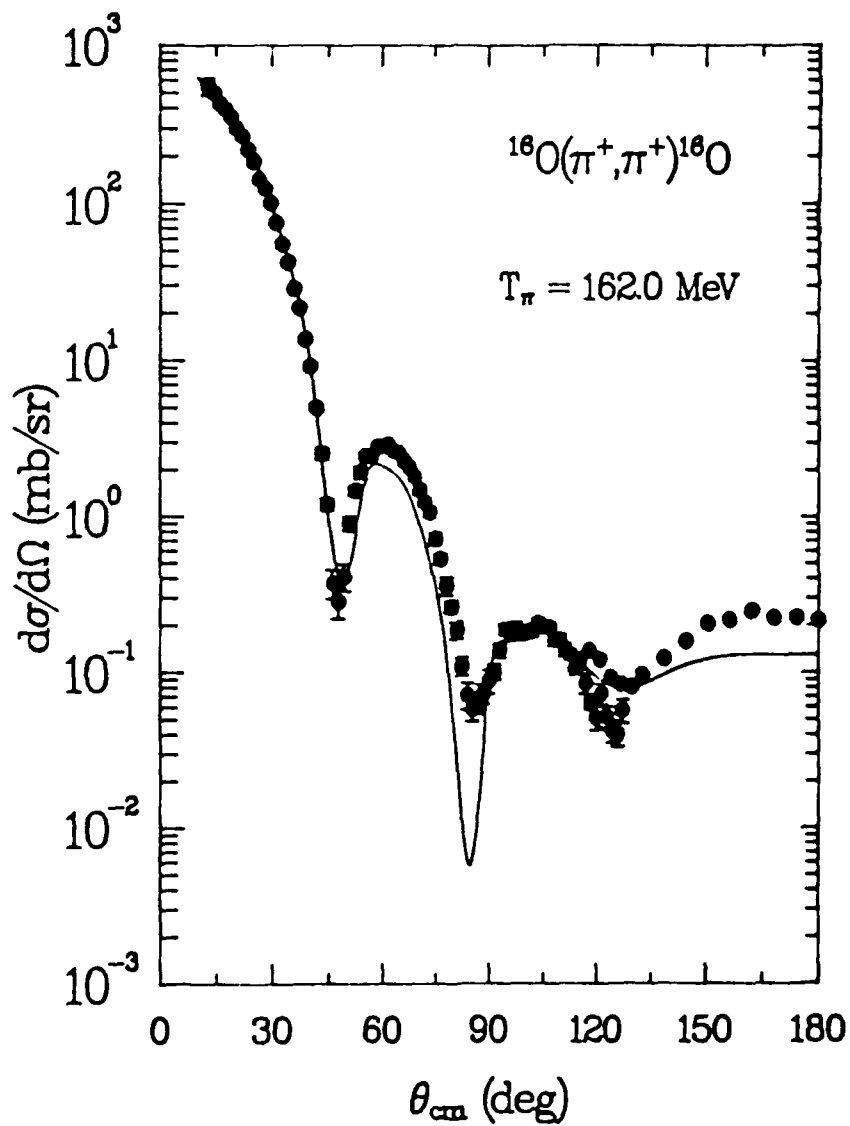


Figure 5: Fit to the  $^{16}\text{O}(\pi^+, \pi^+)^{16}\text{O}$  angular distribution for  $T_\pi = 162 \text{ MeV}$  using a modified delta-hole model in the local density approximation.

## 2 Experimental Apparatus and Procedure

The experiment described in this thesis was performed using the Energetic Pion Channel and Spectrometer (EPICS) system at the Clinton P. Anderson Meson Physics Facility in Los Alamos, New Mexico (LAMPF). This facility consists of an 800-MeV linear accelerator capable of accelerating  $H^+$  and  $H^-$  ions and several experimental areas used in nuclear structure and nuclear chemistry studies. The beam, which was designed with an average current of 1 mA at a duty factor of 6-12%, impinges on a graphite target in one of the target areas producing pions and other secondary particles. Figure 6 is a drawing of Experimental Area A at LAMPF, the area where EPICS is located  $35^\circ$  off of the beam line [Li-77]. The figure shows the location of the graphite target, A-1, as well as EPICS and other experimental stations within area A. The references [Li-77, Li-72, Al-77] give further descriptive information on LAMPF.

### 2.1 EPICS Channel and Spectrometer

EPICS was originally designed to perform studies of pion-induced excitation of nuclear levels over the energy range of the  $\Delta(1232)$  pion-nucleon resonance. The system provides good energy resolution ( $<100$  keV) and good angular resolution ( $<10$  mrad), with a scattering range that extends from 0 to  $175^\circ$ . The entire EPICS system consists of three main parts: (1) a high intensity, high resolution pion beam channel capable of delivering a large, dispersed beam on target, (2) a scattering chamber designed specifically to obtain

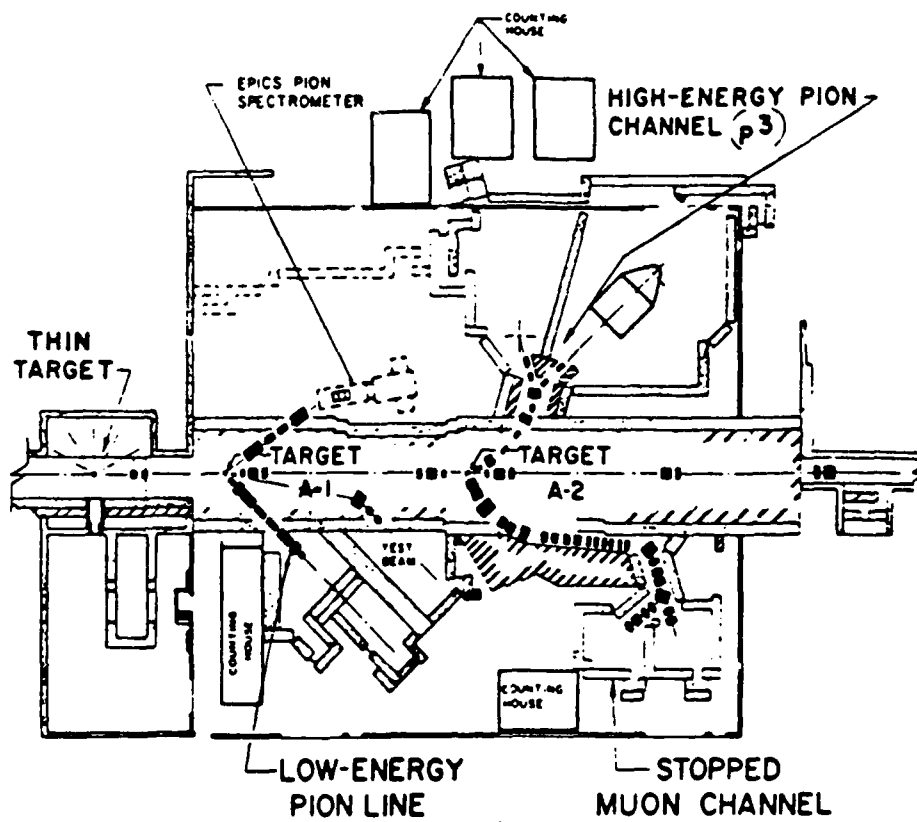


Figure 6: Experimental Area A of the Los Alamos Meson Physics Facility (LAMPF) facility.

large angle data, and (3) a momentum analyzing spectrometer which rotates in the horizontal plane. Figure 7 gives a side-on view of the entire apparatus, each component of which is described below.

The EPICS channel, shown in greater detail in Fig. 8, is made up of several elements: four dipole magnets (BM01–BM04), three multipole focussing magnets (FM01–FM03), and four adjustable collimating jaws (FJ01–FJ04). The length of the channel's flight path, 15.24 m, is long enough to propagate pions of a maximum kinetic energy of 300 MeV, yet short enough to allow an appreciable flux of 70 MeV pions before too great a fraction decays in the channel. The bending magnets are responsible for spreading the beam to give a dispersion in momentum so that specific energy and momentum selections can be made. While the beam is dispersed in this way the pion's momentum is correlated to its position in the dispersed beam. The optical paths in the horizontal and vertical profiles differ such that at the first focal plane the beam profile is horizontally spread while being vertically focussed as shown in the optical mode of Fig. 8. The focussing magnets contain three different windings: half-sextupoles on the top and bottom and a quadrupole. These magnets are used for removing higher-order aberrations of the channel optics. Finally, the collimating jaws are used to control the phase space and flux of the channel beam. The last of these, FJ04, having pairs of both horizontal and vertical jaws, determines the channel's momentum acceptance, the vertical size of the beam at the target, and the horizontal divergence of the beam. With all four jaws fully open the channel characteristics are those shown in Table 1, which leads to a pion flux and composition shown in

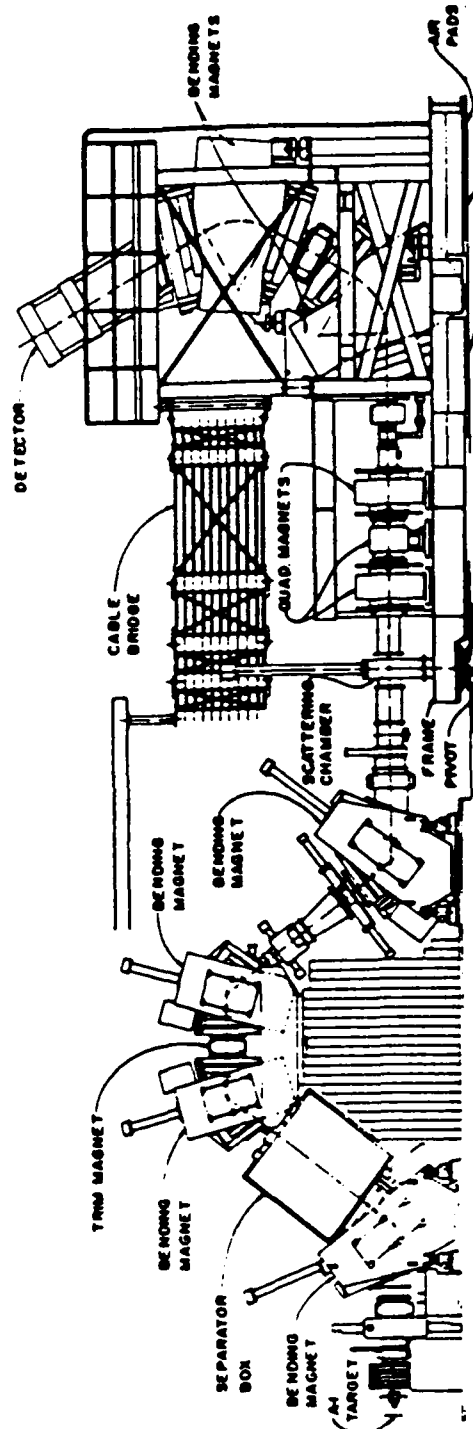


Figure 7: A side-on view of the Energetic Pion Channel and Spectrometer (EPICS) at LAMPF.

Solid angle	3.4 msr
$\Delta p/p$	2%
Beam diameter (horizontal)	8 cm
Beam diameter (vertical)	20 cm
Beam divergence (horizontal)	<10 mrad
Beam divergence (vertical)	100 mrad
Energy range	70-300 MeV

Table 1: EPICS channel specifications [LA-80].

Table 2.

The pion beam delivered by the channel enters a scattering chamber where the beam impinges upon a selected target. The design of the particular scattering chamber at EPICS allows an increase in the scattering angular range (normally limited by available floor space) from previous chambers. An important characteristic of the design is a spectrometer solid angle that is independent of scattering angle. This is achieved by placing a circular-pole magnet at the spectrometer pivot point. This magnet bends both the incoming pion beam and the scattered pions in such a way as to cause pions scattered near  $180^\circ$  at the target to enter the spectrometer when it is located at an angle near  $120^\circ$  on the floor. A top view of this magnet, in place in the system, is shown in Fig. 9. It has 1 m diameter circular poles, a 25 cm pole gap, and a maximum magnetic field in excess of 15 kG. A more complete description can be found in the reference [Bu-86].

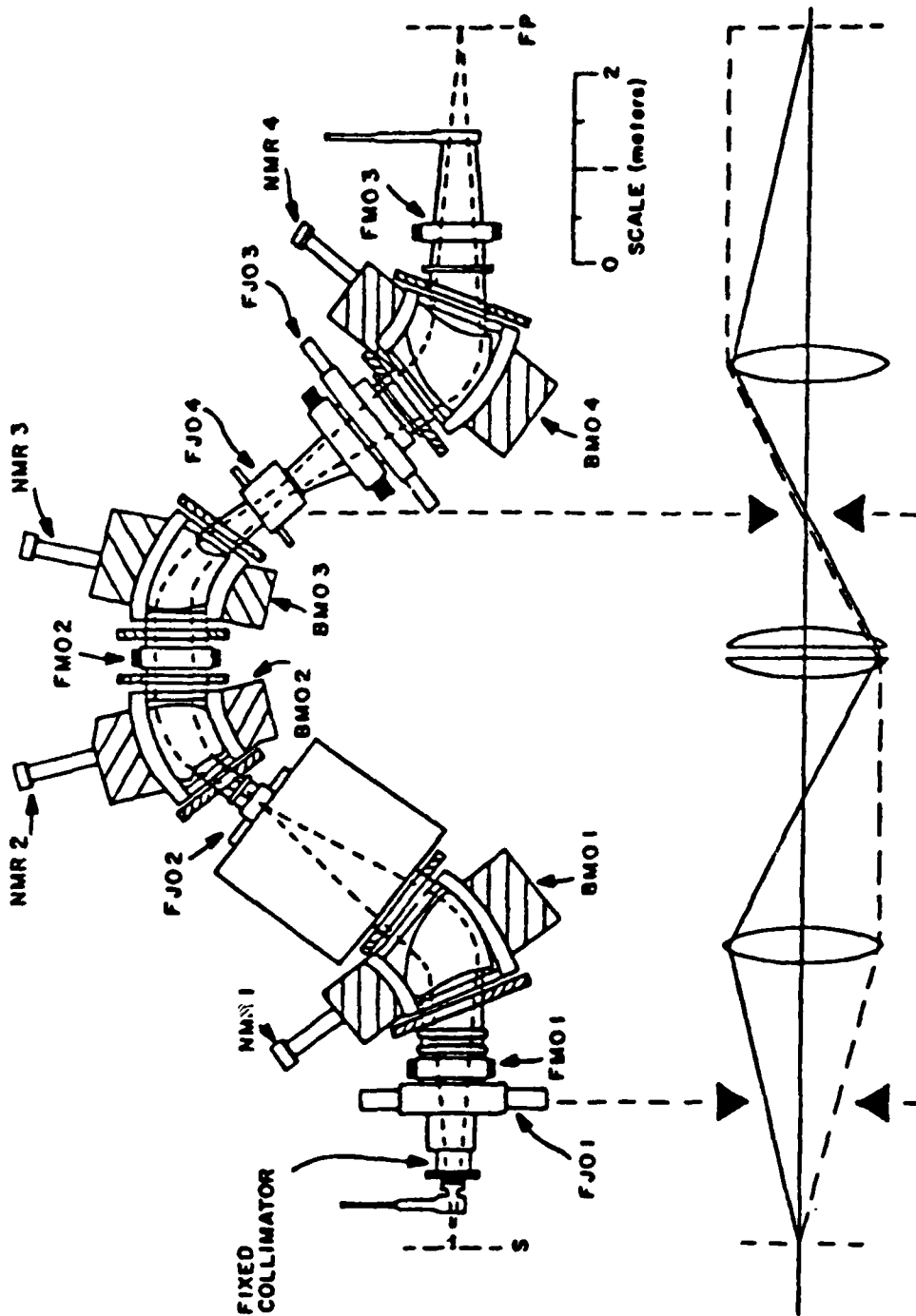


Figure 8: The EPICS channel and its optical mode. The solid (dashed) line illustrates the optics for the vertical (horizontal) plane [Th-77].



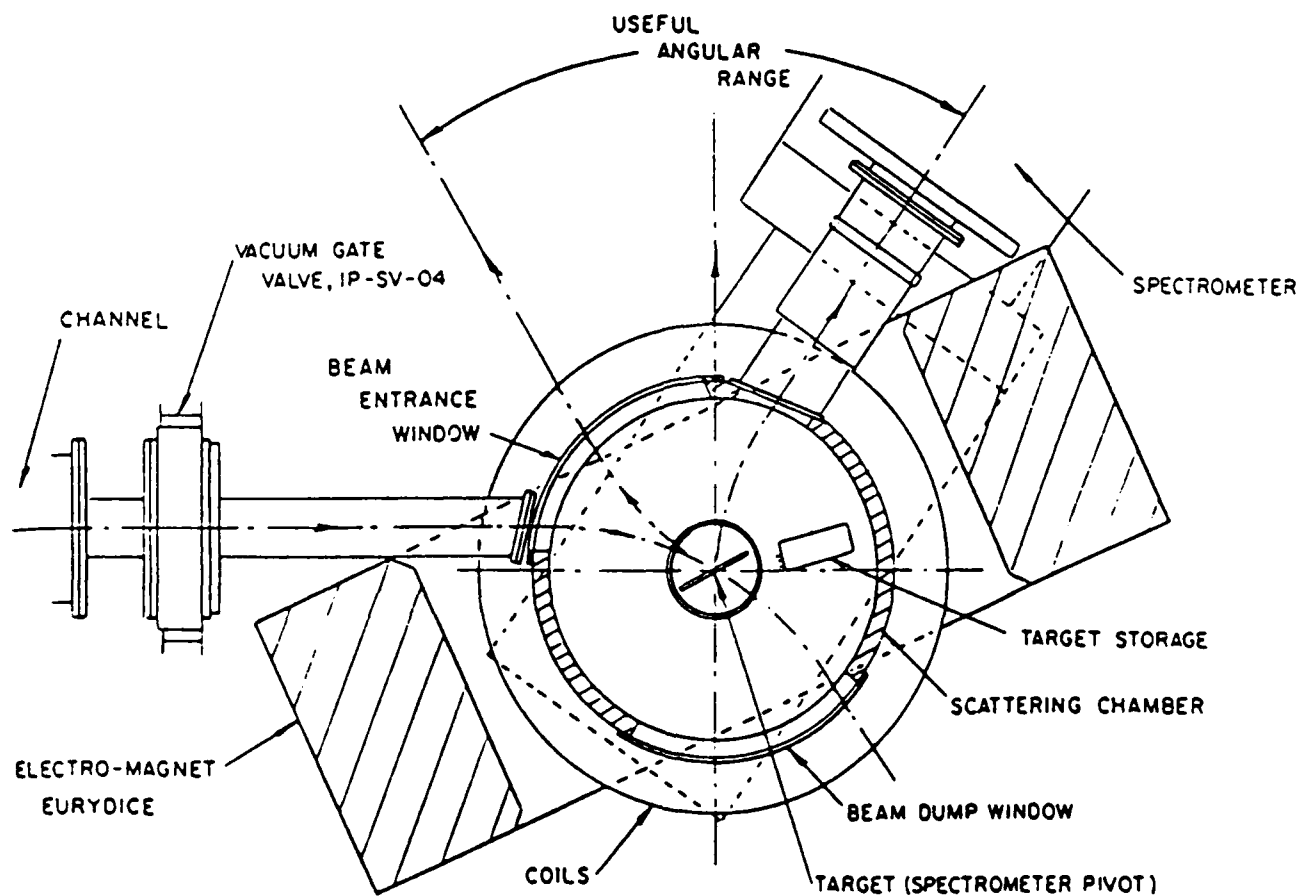


Figure 9: Top view of the circular magnet in place in the system.

$T_\pi$ (MeV)	Pion Flux <sup>a</sup> ( $\times 10^7 \pi/s$ )		Beam Content <sup>b</sup>			
	$\pi^+$	$\pi^-$	$\pi$	p	$\mu$	e
100	6.7	1.8	100	~35	15	50
200	22.0	4.7	100	~400	5	8
300	26.0	4.5	100	~650	2	2

<sup>a</sup>Normalized to a primary proton beam average current of 1 mA.

<sup>b</sup>The relative beam contaminant numbers are normalized to the pion numbers.

Table 2: EPICS channel beam pion flux and composition [LA-80, Bo-84].

At the channel's focal plane (which corresponds to the center of the scattering chamber) there is a target positioning apparatus which holds up to four targets in a vertical array. The target holder can be raised or lowered in order to move various targets into place and may also be rotated with respect to the beam. The angle the target makes with the beam is usually half the scattering angle such that the path length through the target is minimized, thereby minimizing straggling effects and maximizing resolution.

A mobile ionization chamber that serves as a beam monitor is located just outside the vacuum chamber at the beam exit window. The monitor is divided in half to allow positioning of the beam on target. Another larger ionization chamber used in the normal EPICS configuration, located on the

floor, is also utilized as a monitor. Other beam monitors include measurements indicating the intensity of the primary proton beam and the extent of its interactions with the pion production target of the EPICS channel.

The spectrometer itself, shown in Fig. 10, consists of three quadrupole magnets (QM01-QM03), two dipole magnets (BM05-BM06), and two focal plane detector systems described later. The spectrometer rotates through the angles  $-10^\circ$  to  $120^\circ$  pivoting around a point at the focal plane of the channel. The purpose of the quadrupole triplet is to provide an inverted image of the scattering target such that the coordinate  $x$  at the plane of the detector system is inverted and proportional to the vertical position of the scattering event at the target, the coordinate  $y$  at the same plane is horizontal and proportional to the scattering angle at the target, and the coordinate  $z$  traces the center path line through the spectrometer. The dipole magnets vertically disperse the beam by an amount  $4 \text{ cm}/\%$ , and the useful momentum bite of the spectrometer is  $\pm 6\%$ . Table 3 shows the specifications for the spectrometer itself and Fig. 11 illustrates the optics of the spectrometer in schematic fashion and the coordinate system used in defining the particle trajectories.

This figure also shows the location of the various other components of the spectrometer. The front focal plane detector system consists of four multiwire proportional drift chambers (F1-F4) where F4 is located at the focal plane of the quadrupole triplet, while a similar rear focal plane detector system (R5-R6,R9-R10) has R5 located at the rear focal plane. These detector systems are followed by a plastic scintillator (S2), a slab of lucite used as a

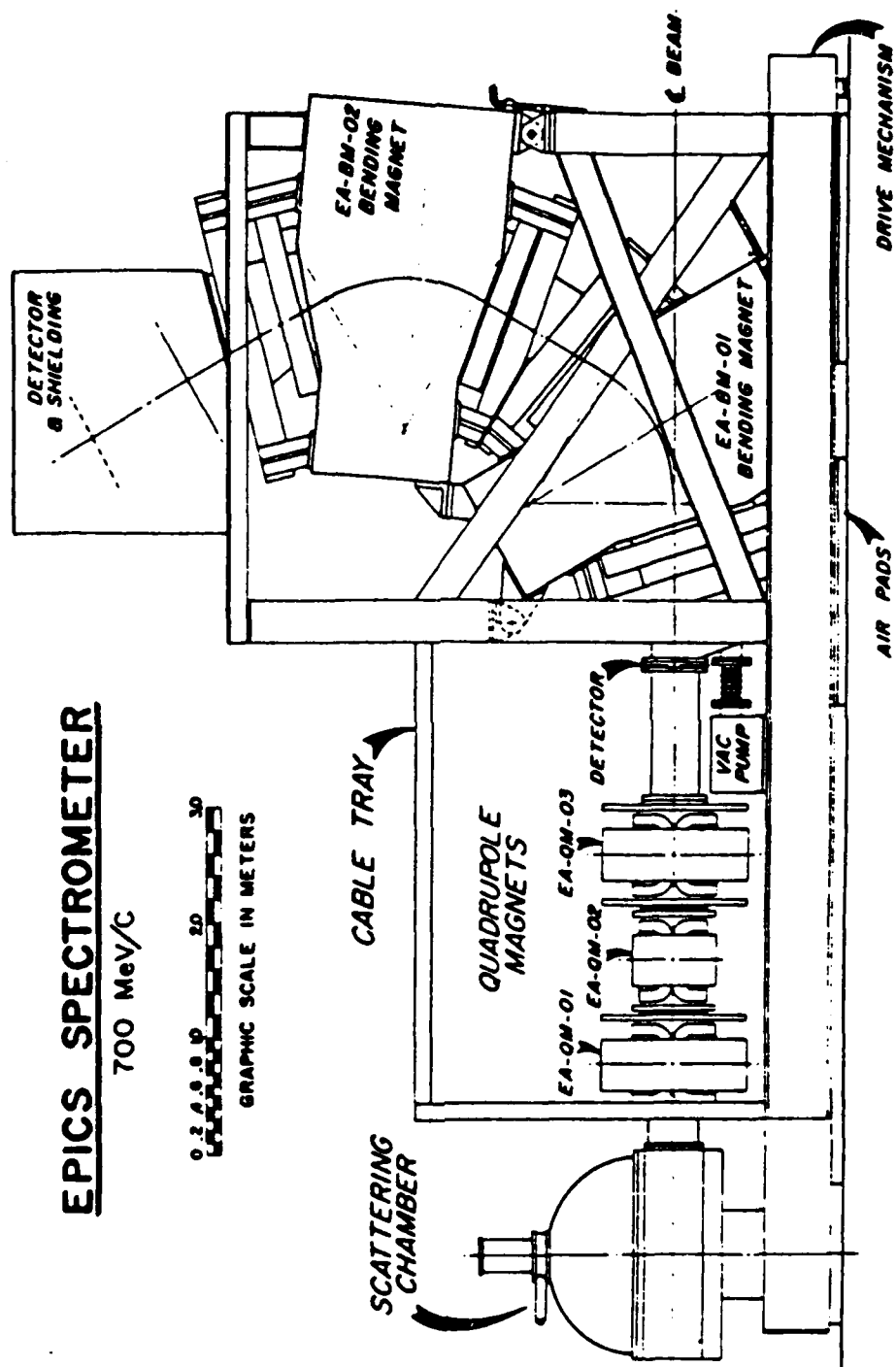


Figure 10: The EPICS spectrometer.

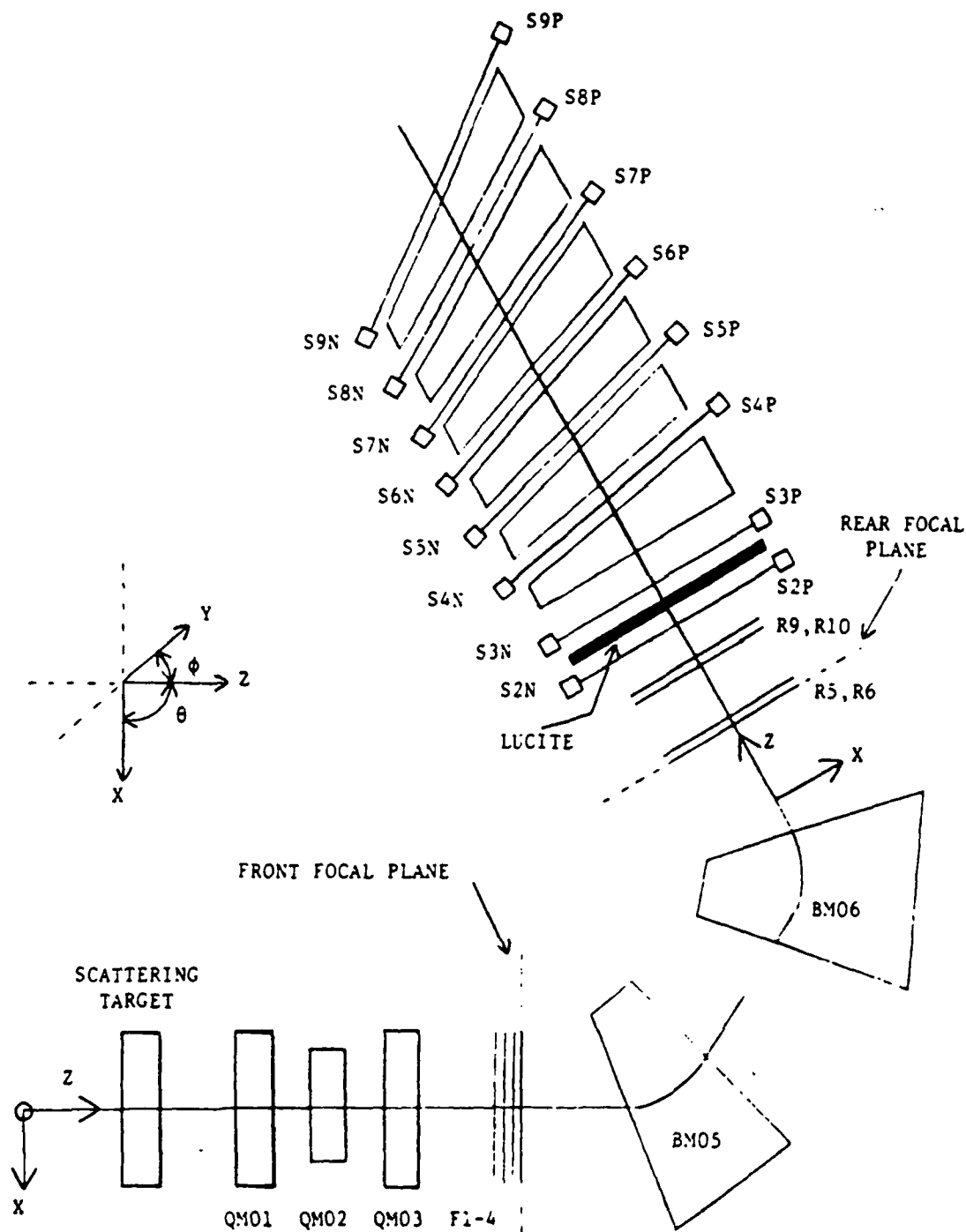


Figure 11: Schematic view of the EPICS spectrometer optics and detector system.

Solid angle	~10 msr
$\Delta p/p$	14%
Momentum range	100-750 MeV/c
Flight path	~125 cm
Dispersion	4 cm/%

Table 3: EPICS spectrometer specifications [LA-80].

proton absorber for  $\pi^+$  particles, another scintillator (S3), and finally a series of graphite blocks and scintillators which serve as a muon rejection system. This system is described more fully in the next section.

## 2.2 Detector System and Beam Monitoring

The multiwire proportional drift chambers mentioned earlier must be able to measure the position and angle of the passing particle in order to determine the momenta of the incident and scattered particles. From this information it is possible to reconstruct the kinematics of the interaction. The chambers provide a resolution of  $125 \mu\text{m}$  (FWHM) and can operate at counting rates up to 1 MHz. The four chambers making up the front detector system consist of eight signal planes, two orthogonal sets of four planes each, and are used to obtain the vertical and horizontal position ( $x, y$ ) and angle ( $\theta, \phi$ ) information. Each set of four signal planes having the wires in the same direction are set up as two pairs of planes. The pairs are separated by 10 cm, while the two

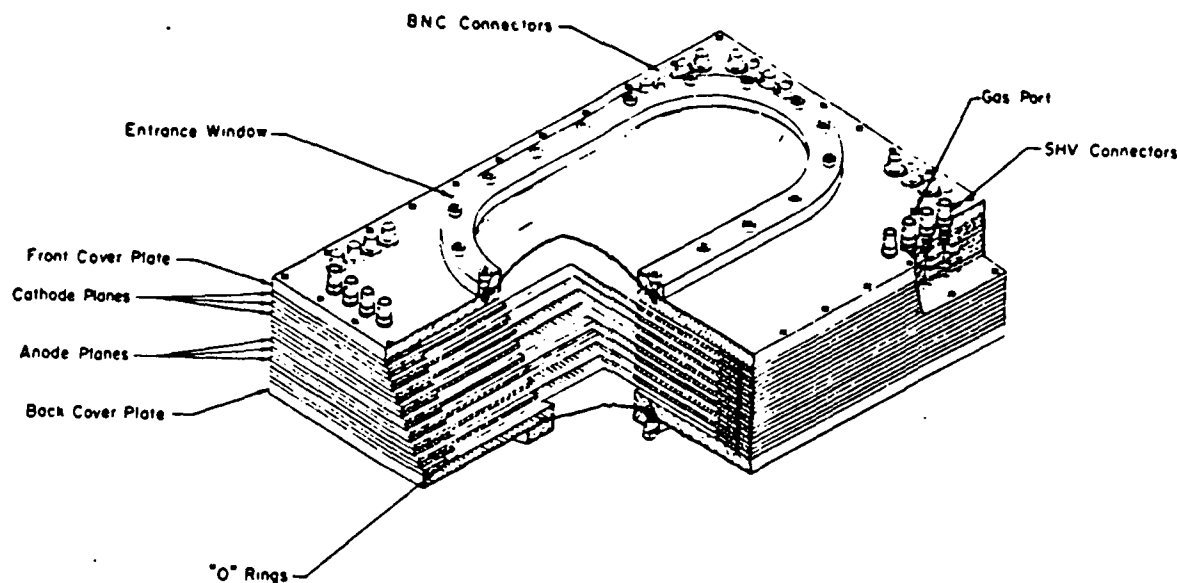


Figure 12: Assembly view of the EPICS front chamber.

signal planes within each pair have a separation of 1 cm and are offset by one-half of a wire spacing. This chamber has an active area of  $20 \times 30$  cm, and is operated in a vacuum. An assembly view of the EPICS front chamber is given in Fig. 12. The rear detector assembly is identical to the forward assembly.

The signal planes are set in an alternating gradient pattern where the anode wires are at positive high voltage ( $\sim 2150$  V) and spaced 8 mm apart, while the cathode wires are at a negative voltage ( $\sim 200$  V), centered between the anode wires. A time difference and time sum from these two signals, anode and cathode (where the cathode signal is processed to look as an anode signal), is created and used to determine the particles position relative to the wires of the signal planes. The angular information is determined using the

10 cm spacing of the pairs of signal planes. Therefore, an abundance of information comes from these detector systems, namely the quantities  $x_f$ ,  $y_f$ ,  $\theta_f$ ,  $\phi_f$ ,  $x_r$ ,  $y_r$ ,  $\theta_r$ , and  $\phi_r$  ( $f$  and  $r$  denoting front and rear). A more rigorous and complete description of these assemblies, their calibration, and operation can be found in the references [At-81, Mo-82, Iv-79].

The two scintillators, S2 and S3, following the rear detector assembly are separated by a slab of lucite during  $\pi^+$  data acquisition so that protons are absorbed and not misidentified as possible events. The signals from these two scintillators are used for particle identification by measuring the time-of-flight between pulse heights. The time-of-flight is linearly proportional to the energy loss in the scintillators and thus proportional to  $(ZeE/pc^2)^2$  where  $E$  is the total energy of the particle,  $p$  is the momentum, and  $Ze$  is the charge [Me-66]. Thus these scintillators help to distinguish particles of different mass and charge.

Following these scintillators is a series of scintillators separated by graphite wedges of varying thickness, the muon rejector. The wedge shape of the graphite absorbers compensates for the variation of momentum across the rear focal plane. The muon rejector is designed to eliminate the muon background produced by the decay of pions not yet reaching the front focal plane. Since muons and pions have identical charges, if they both have the same momenta then they both reach the rear focal plane, however, the energy of the pion is much greater than that of the muon and thus has a shorter range in matter. The first wedge is of the correct thickness to remove 100 MeV pions but not muons. The second wedge removes 140 MeV pions but not muons,



and so on. The signals from the scintillators following a carbon wedge are then used to eliminate muons above a certain threshold from event contention.

In order to properly calculate the pion elastic and inelastic differential scattering cross sections the data must be normalized for the number of incident particles. Three monitors are used for this: (1) an ionization chamber (IC1) located downstream of the scattering target monitors the EPICS channel beam current, (2) an ionization chamber (BOT) located within the pion production target cell monitors the primary beam current, and (3) a charge integrating toroidal coil (1ACM02) located upstream of the pion production target also monitoring primary beam current. The primary beam current monitors are gated with the beam pulse so that they are active only during data acquisition. For this experiment it was determined through a series of cross checks that the most reliable current monitor was the BOT, and it was this monitor's pulses that were used for the normalization calculations.

### 2.3 Data Acquisition and Event Analysis

The data acquisition and analysis system for EPICS consists of an on-line MicroVax computer running on the DEC VAX/VMS system, several CAMAC crates and electronic modules, a VAX/CAMAC interface unit, and the LAMPF data acquisition software package described in detail in [Am-79]. Signals from all of the spectrometer's components are processed through the circuit shown in Fig. 13 consisting of various NIM modules, discriminators,

meantimers, analog-to-digital converters (ADC's), and time-to-digital converters (TDC's). The signal processing culminates in the CAMAC system which digitizes all information to be passed on to the computer via the interface unit. The software system then controls the reading of this data and the writing of data words for each event to magnetic tape (and may also do some on-line data processing as time permits).

Once the data words for an event are read into the computer, the processing of the data is completed on an event-by-event basis using an analyzer software program in conjunction with an experiment-specific test file and an experiment-specific graphics display package. The goal of the data processing is to determine which events are good pion events and to calculate the excitation energy given to the target nucleus by these pions. The main program examines each event calling subroutines to calculate the necessary quantities from the data signals and trajectory information. The test file (described in greater detail below) is then employed to perform user-specified tests of these quantities, determining which are good events. The missing mass associated with each event is then calculated and the data is arranged into bins for subsequent storage as histograms used by the graphics display system.

The first calculation performed by the analyzer is the particle identification test (PID). The PID test consists of an indirect gate on the mean energy loss in scintillators S2 and S3 and another on the time-of-flight between S2 and S3. This eliminates protons from consideration but not muons. Upon passing this test the analyzer proceeds to calculate the positions  $x_f$ ,  $y_f$ ,  $\theta_f$ ,  $\phi_f$ ,  $x_r$ ,  $y_r$ ,  $\theta_r$ , and  $\phi_r$  using drift-time and drift-difference tests on the

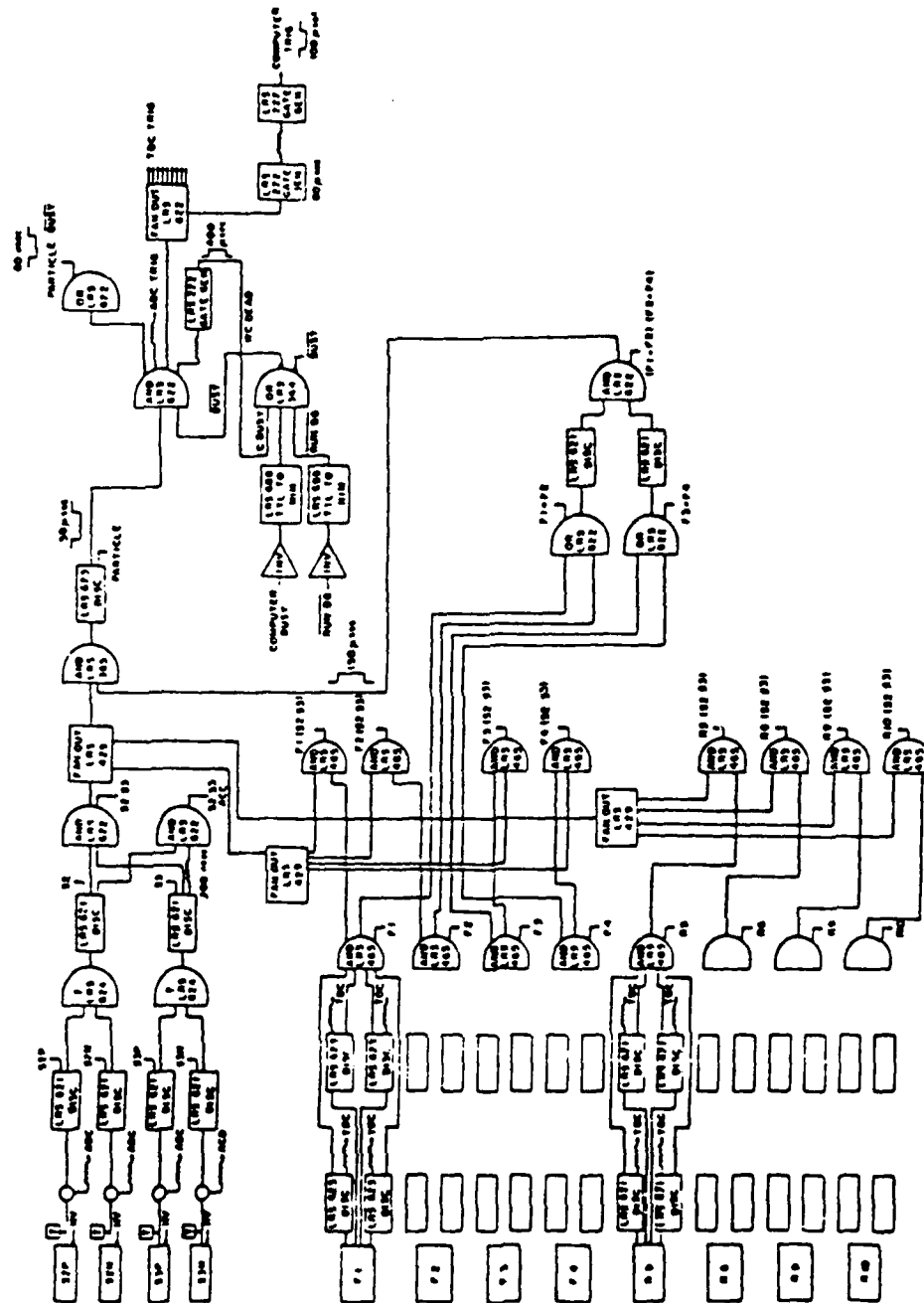


Figure 13: Block diagram of the electronics for the EPICS data acquisition system.

multiwire proportional drift chamber signals. These tests compare the positions calculated for the four chamber planes to a straight line trajectory and eliminates events where two particles passed through the chambers simultaneously and pion events which created knock-on electrons with the group of four chamber planes.

From the position information above the next step is to calculate the values  $x_{tgt}$ ,  $y_{tgt}$ ,  $\theta_{tgt}$ , and  $\phi_{tgt}$ . To first order

$$x_{tgt} = -x_f \quad (9)$$

where aberrations in the quadrupole magnets cause higher order terms due to the impossibility of designing magnets such that their central rays are perfectly described. Optimization techniques are employed to account for these anomalies.

The incident momentum of any event detected can be calculated from  $x_{tgt}$  by,

$$P_{inc} = P_c(\delta_c + 1) \quad (10)$$

where  $P_c$  is the incident pion channel central momentum, calculated from the channel magnet settings, and,

$$\delta_c = x_{tgt}/D_c \quad (11)$$

where  $D_c$  is the dispersion of the channel (see Table 1). The scattered momentum, likewise, can be calculated from  $x_r$  by,

$$P_f = P_s(\delta_s + 1) \quad (12)$$

where  $s$  denotes those values referenced to the spectrometer with,

$$\delta_s = \frac{x_f + x_r}{D_s}. \quad (13)$$

The missing mass,  $Q$ , is calculated from these values as the incident energy minus the energy of the outgoing pion after the recoil of the nucleus is taken into account. Thus

$$Q = [(E_{\text{inc}} - E_{\text{final}} + M)^2 - P^2]^{1/2} - M \quad (14)$$

where  $M$  and  $P$  are the mass and recoil momentum of the target nucleus.

Quantities such as  $x_{\text{tgt}}$ ,  $y_{\text{tgt}}$ , and  $Q$  are processed, as mentioned earlier, into histograms as shown in Figs. 14, 15, 16, and 17, where gates may be set in order to cut out background and other spurious data. The yields of the peaks in the missing mass spectra (histograms) can be converted to absolute cross sections the procedure for which is described later.

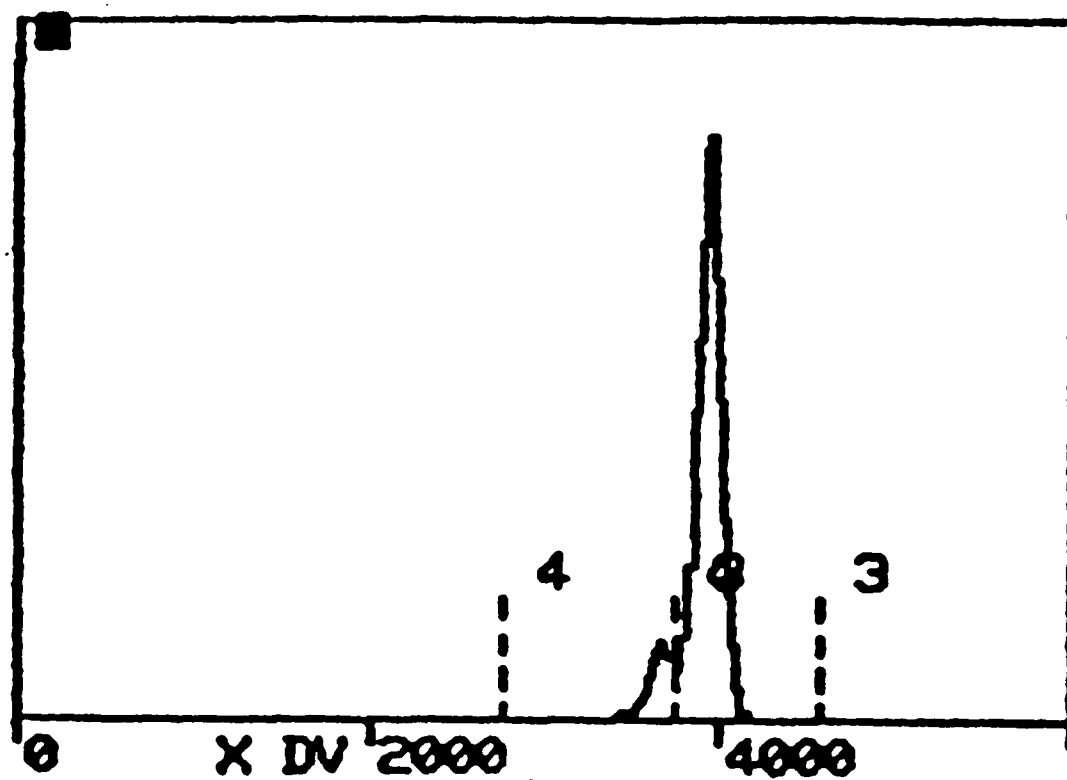


Figure 14: On-line time-of-flight histogram. Muons are between the left gates while pions are between the right.

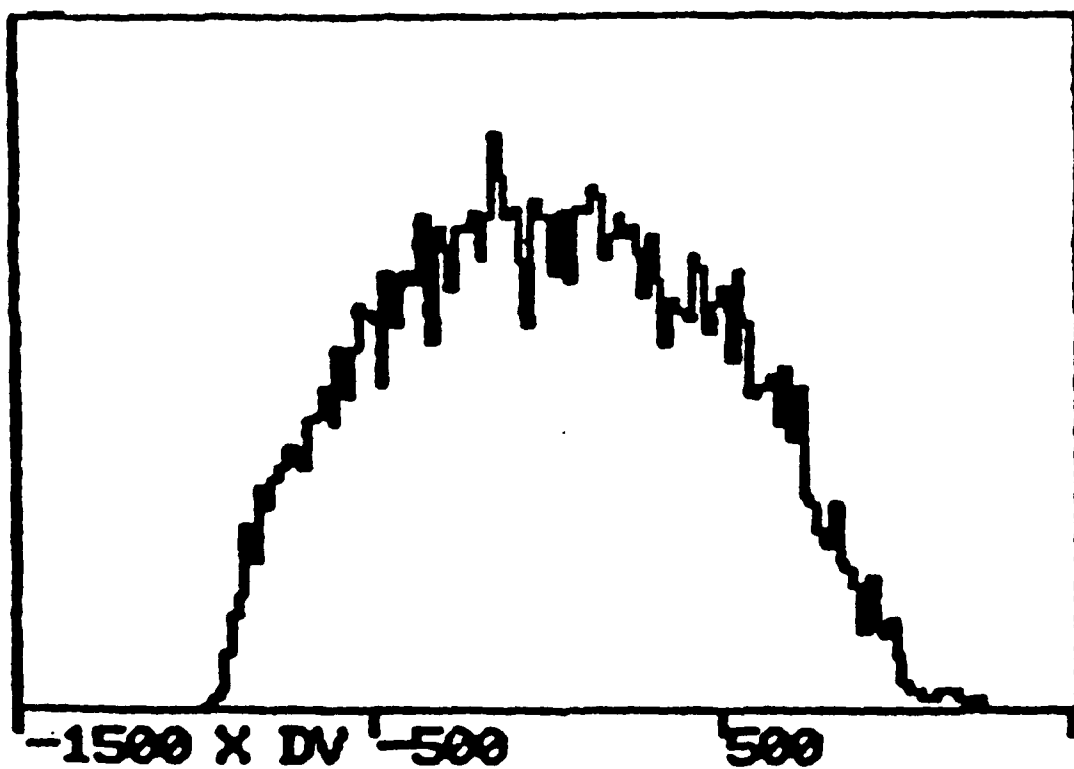


Figure 15: On-line  $x_{tgt}$  histogram.

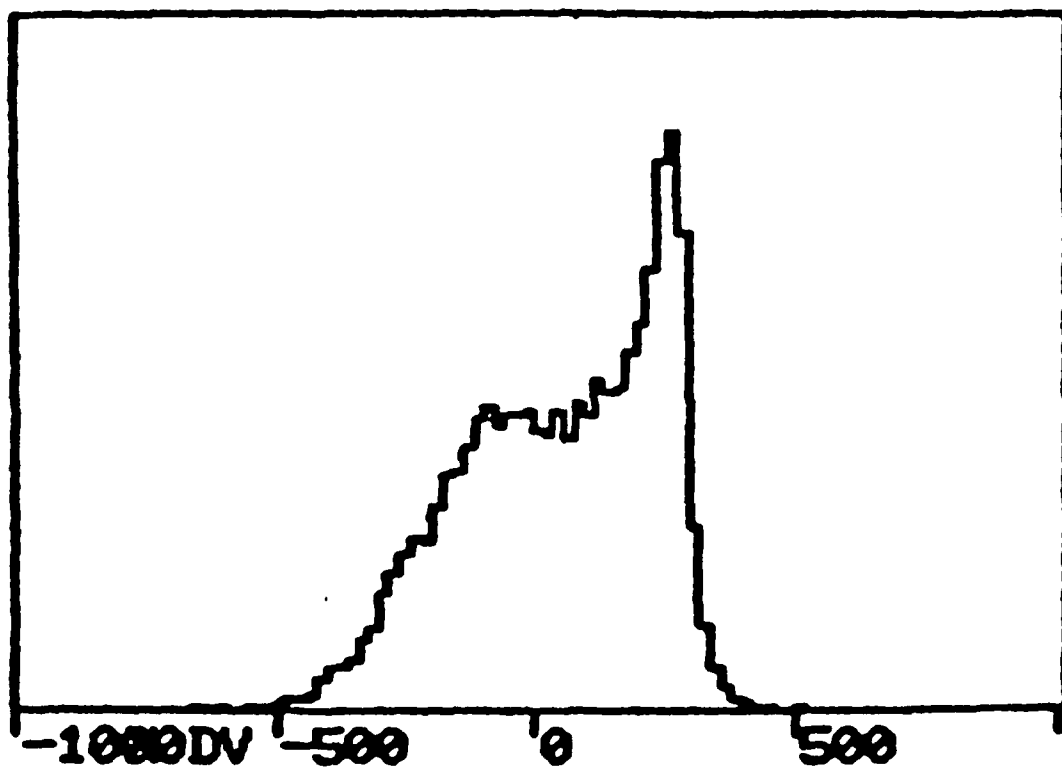


Figure 16: On-line  $y_{tgt}$  histogram.



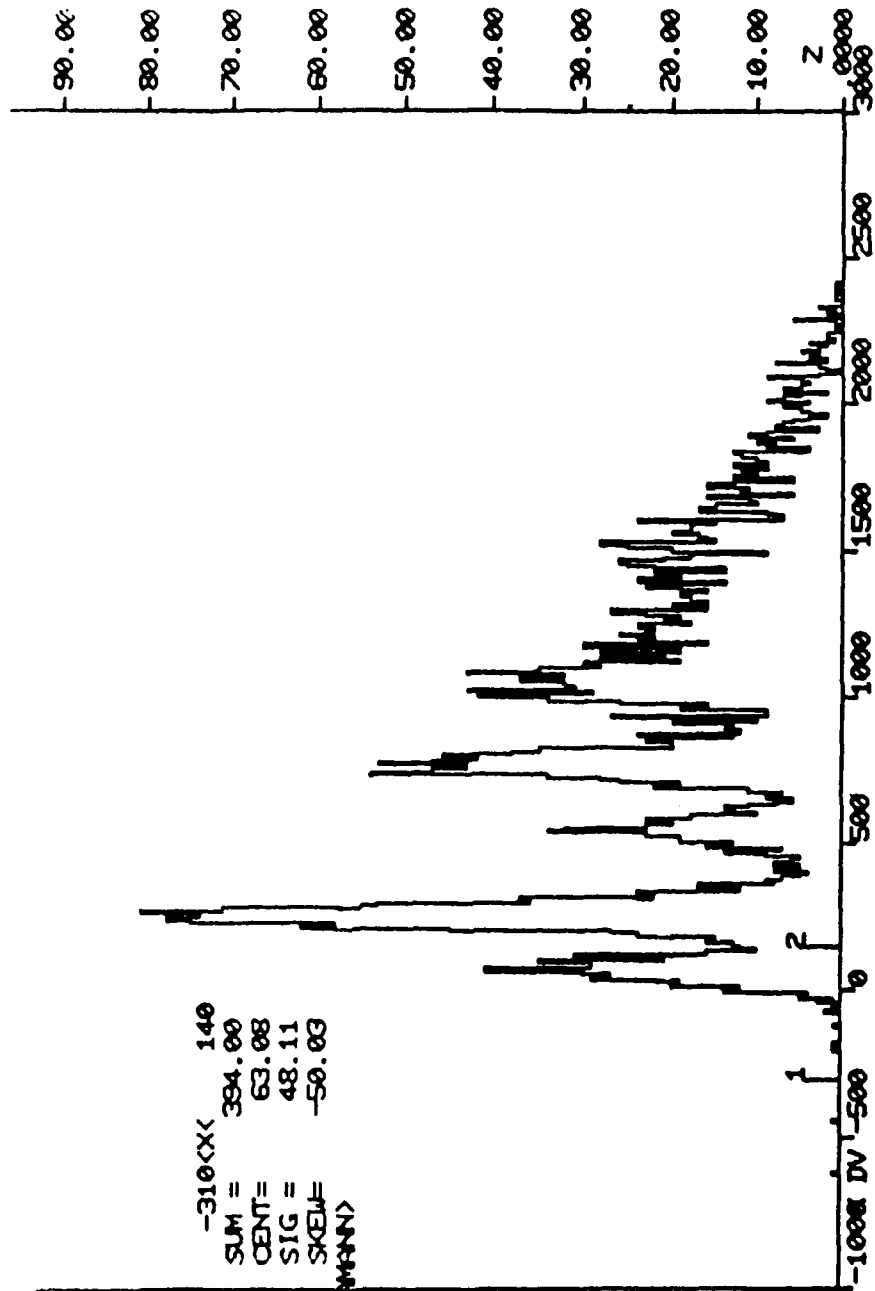


Figure 17: Typical Q-value spectrum (missing mass histograms, MMP1) showing the ground state and the first three excited states of  $^{28}\text{Si}$ .

### 3 Data Reduction and Results

In this experiment differential cross sections were measured for  $\pi^+$  and  $\pi^-$  elastic scattering of  $^{40}\text{Ca}$  and  $^{28}\text{Si}$  at incident pion energies ranging from 100 to 260 MeV at a scattering angle of  $175^\circ$ . Differential cross sections were also measured for  $\pi^+$  and  $\pi^-$  inelastic scattering to the  $2^+$ , 1.78 MeV,  $4^+$ , 4.62 MeV, and  $3^-$ , 6.88 MeV states of  $^{28}\text{Si}$  at incident pion energies of 130, 180, and 226 MeV and scattering angles between  $115^\circ$  and  $175^\circ$  in  $6^\circ$  increments. The  $^{40}\text{Ca}$  target had an areal density of  $515.7 \text{ mg/cm}^2$  while the  $^{28}\text{Si}$  target had an areal density of  $150 \text{ mg/cm}^2$ . The  $\text{CH}_2$  target used for the hydrogen normalization data had an areal density of  $165 \text{ mg/cm}^2$  and the  $^{12}\text{C}$  target used during the acceptance scan runs had an areal density of  $302 \text{ mg/cm}^2$ .

#### 3.1 Peak Extraction of Missing Mass Spectra

Pion elastic and inelastic cross sections are calculated from the peak areas extracted from the missing mass histograms of good pion events. These histograms contain only those events which have passed the tests previously described. Each missing mass histogram contains good pion events for the full angular acceptance of the spectrometer, or  $\theta_s \pm \sim 1.5^\circ$ , where  $\theta_s$  is the scattering angle for which the spectrometer has been set.

The peak areas for the elastic peaks of  $^{40}\text{Ca}$ ,  $^{28}\text{Si}$ ,  $^{12}\text{C}$ , and  $^1\text{H}$  (from the  $\text{CH}_2$  normalization target), and the inelastic peaks of the first three excited states of  $^{28}\text{Si}$  were extracted from their respective Q-value spectra (miss-

ing mass histograms) using the lineshape oriented fitting program NEWFIT. NEWFIT allows the simultaneous fitting of several peaks, each with a separate lineshape. Each peak may be treated as *floating*, where NEWFIT may vary the centroid independently of the others, or *constrained* to a fixed value or in reference to another peak. That is, the centroids of a group of peaks may be constrained to have fixed separations but the position of the group may shift. NEWFIT automatically determines the background from the displayed region of the histogram as a polynomial whose order is specified by the user. NEWFIT then determines the best fit background for the histogram and subtracts it from the spectrum. The remaining spectrum is assumed to contain the peaks of interest and are fitted with user-specified lineshapes. These fits have many variables to choose from such as (1) the determination of the centroid (floating or constrained), (2) the cutoff energy, (3) the lineshape (simple, Lorentzian, Gaussian), (4) the widths of the lineshapes, and (5) the tails the lineshapes are folded with (REF, exponential, different tails on either side of the peak). This program may have a weakness when dealing with peaks strongly correlated with background or where the background is very large with respect to the data in that it may underestimate the yield, but such was not the case for the data here.

To determine the areas for the elastic peak of  $^{40}\text{Ca}$ , the Q-value spectra were fitted in the region -3.0 to 3.0 MeV with a first order polynomial background using a single, floating, symmetric Lorentzian lineshape to adjust for the offset. An example of a fit to the Ca data for an incident pion energy of  $T_\pi=170$  MeV is shown in Fig. 18. To determine the areas for the elas-

tic and inelastic peaks to the first three excited states of  $^{28}\text{Si}$ , the Q-value spectra were fitted in the region -3.0 to 9.0 MeV with a first order polynomial background and all four peaks constrained to be at 0.0, 1.78, 4.62, and 6.88 MeV after the 0.0 MeV peak was floated to find the proper energy offset. An example of a fit to the Si data for an incident pion energy of  $T_\pi=100$  MeV is shown in Fig. 19. The peaks in this case were all fit with symmetric Lorentzians of variable widths. The lineshapes were determined for all spectra taken at all incident pion energies because the resolution varied with energy from 1.8 MeV (FWHM) at  $T_\pi=100$  MeV to 2.3 MeV (FWHM) at  $T_\pi=260$  MeV for the  $^{40}\text{Ca}$  target and 1.0 MeV (FWHM) at  $T_\pi=100$  MeV to 1.4 MeV (FWHM) at  $T_\pi=240$  MeV for the  $^{28}\text{Si}$  target.

### 3.2 Cross Section Calculations

The differential scattering cross section in the center-of-mass system is characterized by the following,

$$\frac{d\sigma}{d\Omega} = \frac{J}{N_{\text{tgt}}} \frac{N_s dt}{N_i dt d\Omega} \quad (15)$$

where  $J$  is the Jacobian of the transformation from the laboratory to the center-of-mass system,  $N_{\text{tgt}}$  is the number of independent scattering centers in the target which are intercepted by the beam,  $N_s dt$  is the number of pions scattered at an angle  $\theta$  into the solid angle  $d\Omega$  in the time interval  $dt$ , and  $N_i dt$  is the number of pions crossing the unit area perpendicular to the channel beam in the time interval  $dt$  (number of incident pions).

The term  $N_s dt$  is a corrected value of the peak yields extracted from the

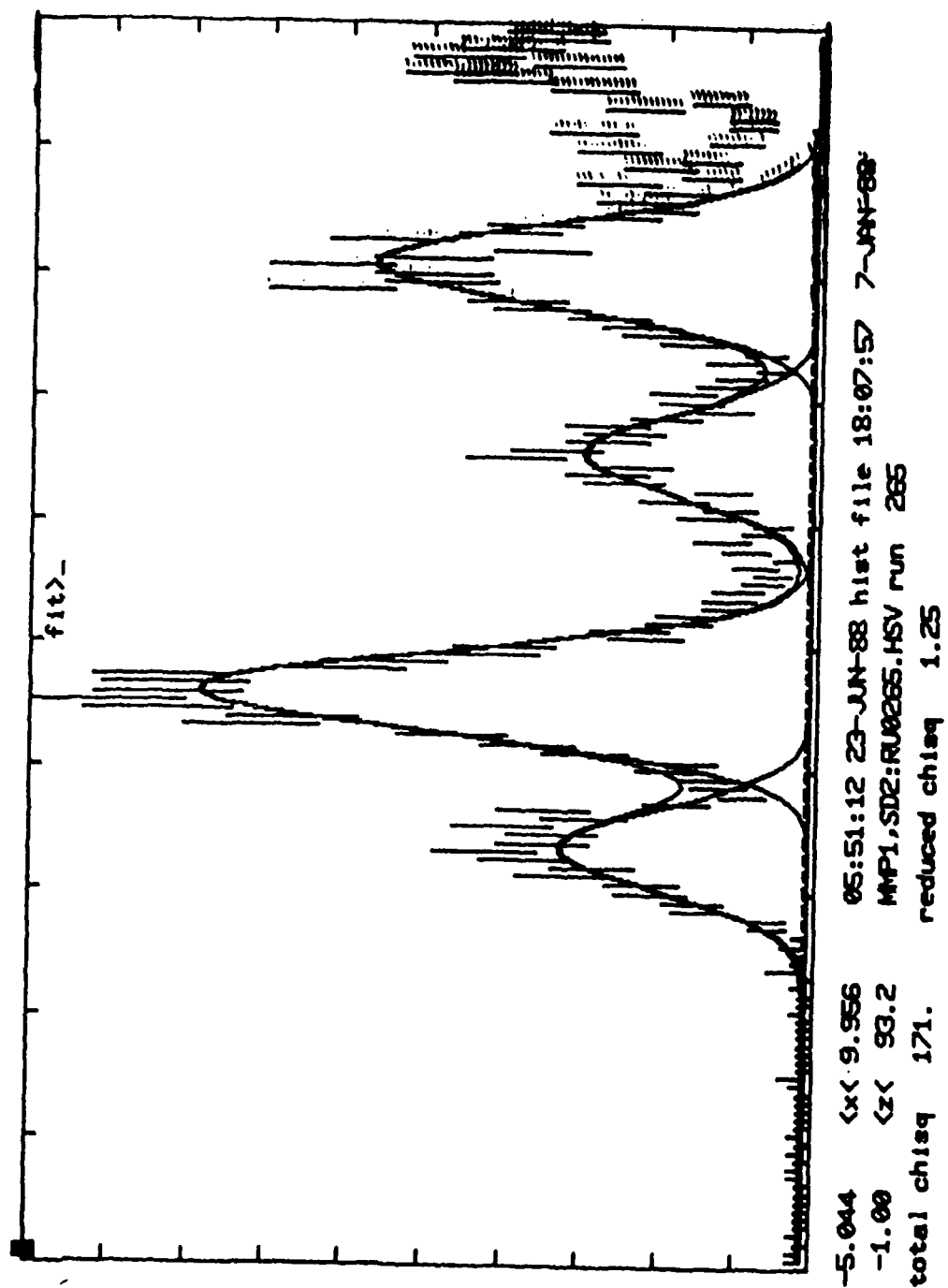


Figure 18: An example of a fit to the Ca data for an incident pion energy of  $T_{\pi}=170$  MeV.

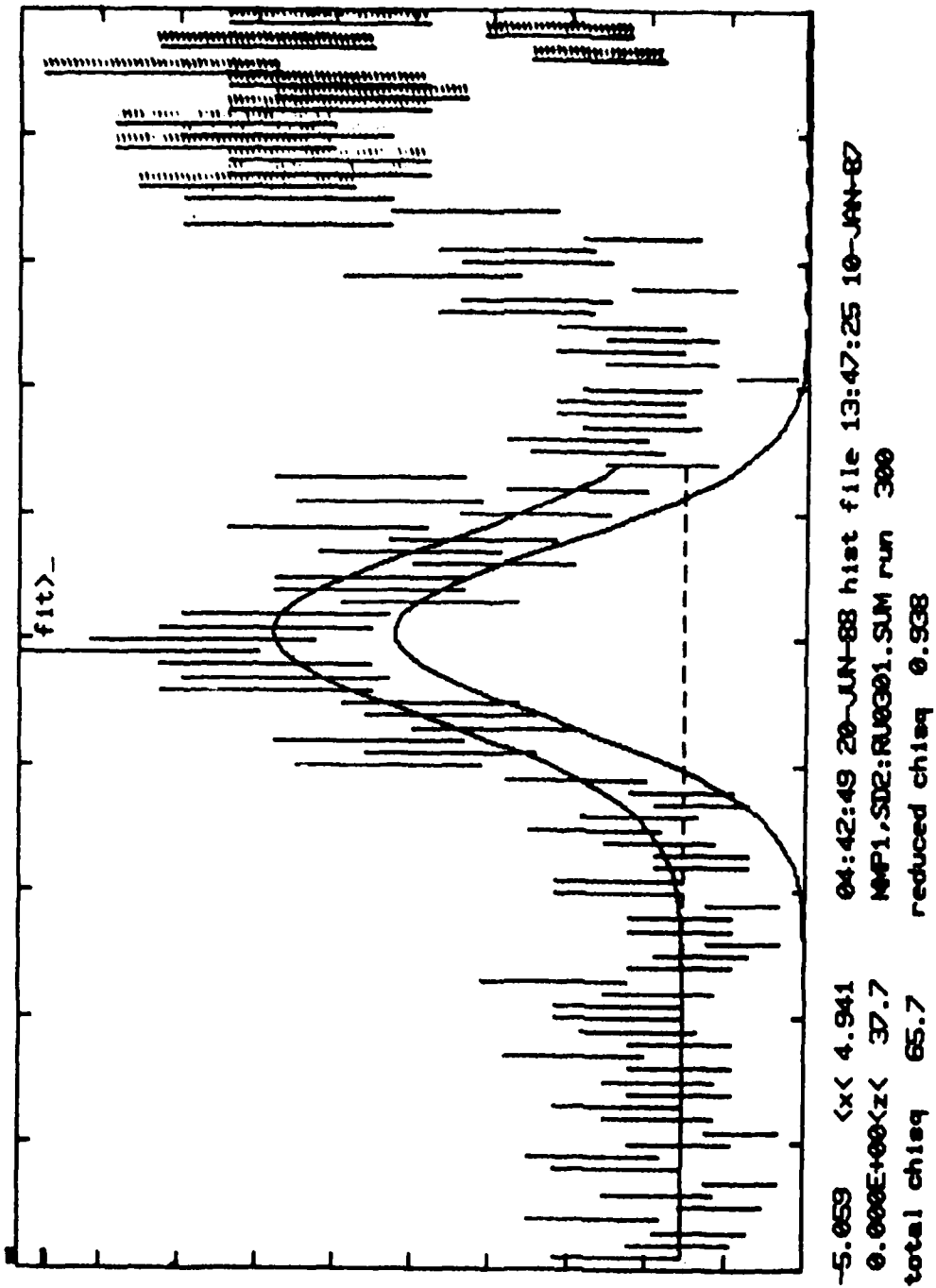


Figure 19: An example of a fit to the Si data for an incident pion energy of  $T_\pi=100$  MeV.

missing mass histograms

$$N_s = PA \cdot CF \quad (16)$$

where PA is the peak area and CF is a correction factor compensating for inefficiencies in the data acquisition system and is given by

$$\frac{1}{CF} = CLT \cdot CREFF \cdot CHEFF \cdot LE \cdot SF \cdot SACORR \quad (17)$$

CLT is the computer live time, the ratio of the number of hardware trigger signals, to the total number of trigger signals and is a measure of the computer's rate of data taking. DREFF is the drift efficiency of the multiwire proportional drift chambers and corrects for those events producing signals in all chamber planes but not passing the drift difference tests. CHEFF is the chamber efficiency and is the product of the sixteen individual chamber efficiencies, each given by,

$$CHEFF_i = \frac{\text{all chambers OK}}{\text{all chambers but } i \text{ OK}} \quad (18)$$

LE is the fraction of analyzed events, which, since *all* the events are replayed and analyzed, is equal to unity. SF corrects for the pions that decay after the scattering target and before scintillator S3, and is computed as

$$SF = e^{-t/\tau'} \quad (19)$$

where

$$t = \frac{\gamma L m_\pi}{p_\pi} \quad (20)$$

and

$$\tau' = \gamma \tau_\pi \quad (21)$$

where  $p_\pi$  is the relativistic momentum of the pion,  $m_\pi$  is the rest mass of the pion,  $\tau_\pi$  is the mean lifetime of the pion,  $\gamma = 1/(1 - v^2/c^2)^{1/2}$ , and  $L$  is the path length from the scattering target to S3 which, corrected to first order in  $\delta_s$ , for varying pathlengths,  $L = (12.28 - 0.035\delta_s)$  meters. SACORR is a correction factor for the variation of the spectrometer's solid angle as a function of  $\delta_s$ . This correction factor is determined by measuring the yield of a state (usually an elastic peak) for  $-6\% \leq \delta_s \leq 6\%$ . The  $\delta_s$  is varied in gradations by varying the spectrometer field settings. Then a  $^{12}\text{C}$  target was used to measure the pion elastic scattering yield at each gradation. The usual procedure is then to take experimental data where  $\delta_s$  is set to correspond to the flat region of the spectrometer's solid angle variation versus  $\delta_s$  curve (acceptance curve). This procedure minimizes solid angle correction errors. The acceptance curve for this experiment is shown in Fig. 20 and tabulated data for the acceptance scan is in the Appendix. The experiment was run with  $\delta_s$  set at 2%.

The quantity  $N_i dt$  is given by the relation

$$N_i dt = \frac{\text{CM}}{A} \alpha \cos \theta_{tgt} \quad (22)$$

where CM indicates the number of scaled counts from the current monitor, which in this experiment is the monitor BOT described earlier,  $\cos \theta_{tgt}$  corrects for the scattering target not being perpendicular to the channel beam,  $A$  is the target area intercepted by the beam, and  $\alpha$  is a proportionality factor since the beam monitors are only relative monitors of the pion current.



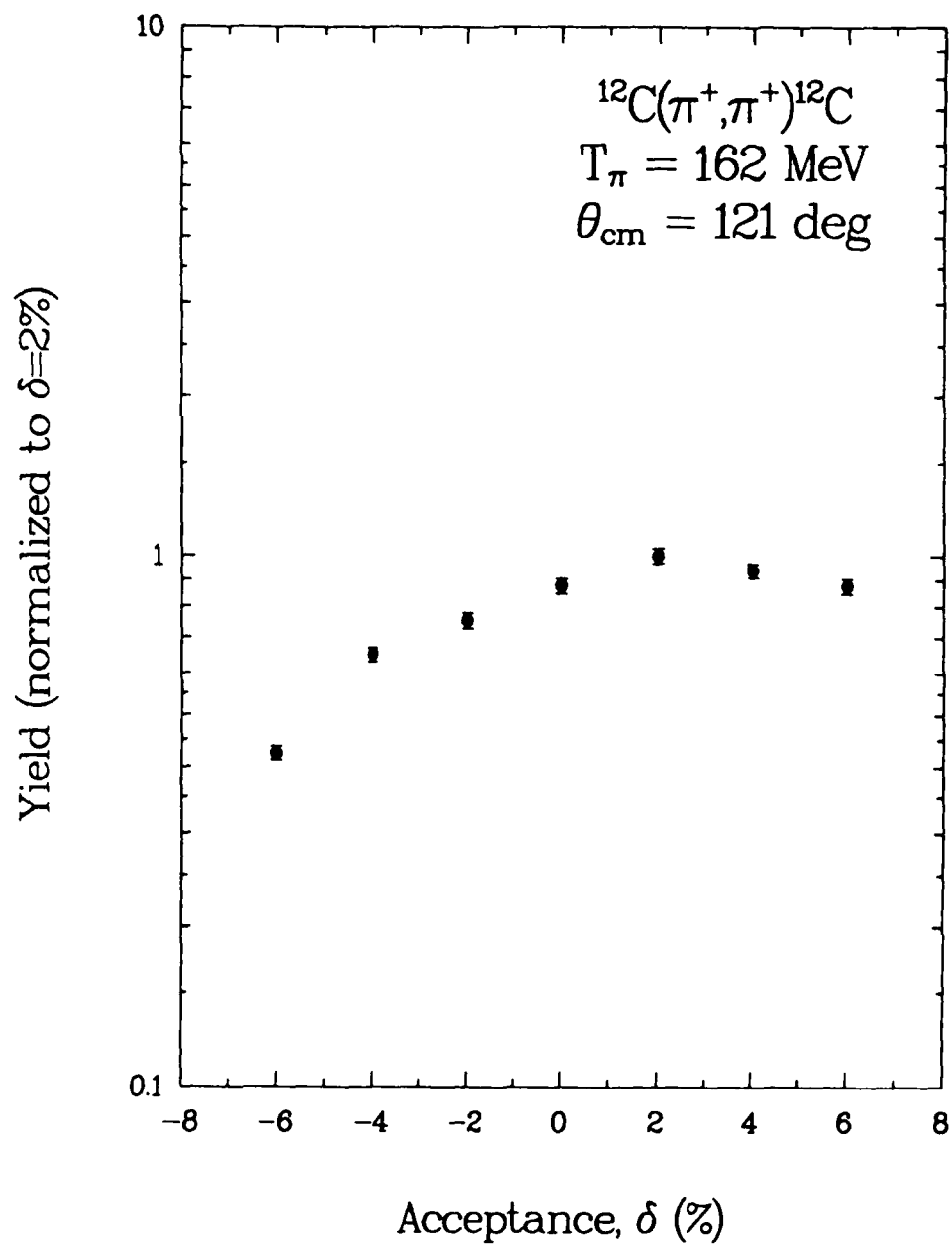


Figure 20: Acceptance curve for scan of  $\delta$ , settings for the pion elastic scattering yield from  $^{12}\text{C}$ .

Finally,

$$N_{tgt} = AN_{s.c.}T_{tgt} \quad (23)$$

where  $A$  is the target area,  $T_{tgt}$  is the target thickness, and  $N_{s.c.}$  is the number of scattering centers per unit volume calculated as

$$N_{s.c.} = \frac{N_0\rho}{M_{tgt}} \quad (24)$$

with  $N_0$  as Avogadro's number,  $\rho$  as the target density, and  $M_{tgt}$  as the mass of the target in grams/mole.

The differential cross section can now be written as

$$\frac{d\sigma}{d\Omega} = \frac{(PA \cdot \text{NORM3})JM_{tgt}}{(\text{areal density})N_0\alpha d\Omega} \quad (25)$$

where

$$\text{NORM3} = \frac{CF}{CM \cos \theta_{tgt}} \quad (26)$$

and the areal density is  $\rho T_{tgt}$ . Since neither  $\alpha$  nor  $d\Omega$  is known, the normal procedure is to determine the absolute magnitude of the differential scattering cross section by measuring a known differential scattering cross section. Therefore, for each incident pion energy, spectra were measured for  $\pi^+p$  scattering with  $\text{CH}_2$  targets of the same dimensions as the  $^{40}\text{Ca}$  and  $^{28}\text{Si}$  targets. Using the Coulomb-corrected phase-shift predictions from the computer code CROSS [Bu-un], which uses the phase shifts of Rowe, Salomon, and Landau [Ro-78], to determine  $d\sigma/d\Omega_H$  we can define the value  $\alpha d\Omega$  as

$$\alpha d\Omega = \frac{14}{2} \frac{(PA_H \cdot \text{NORM3}_H)J_H M_H}{(\text{areal density})_{\text{CH}_2} N_0 (d\sigma/d\Omega)_H} \quad (27)$$

where the 14/2 corrects for one mole of  $\text{CH}_2$  containing two grams of hydrogen and twelve grams of carbon. The energy-dependent factor  $\alpha$  is shown in Fig. 21 for  $\pi^-$  at  $120^\circ$  and in Fig. 22 for  $\pi^+$  at  $130^\circ$  and  $150^\circ$ . These data points were curve fitted to get an energy-dependent function for  $\alpha$ . Now the differential scattering cross section looks like

$$\left(\frac{d\sigma}{d\Omega}\right)_{\text{tgt}} = \frac{12}{14} \left(\frac{d\sigma}{d\Omega}\right)_H \frac{(\text{areal density})_{\text{CH}_2} (\text{PA} \cdot \text{NORM3})_{\text{tgt}} J_{\text{tgt}}}{(\text{areal density})_{\text{tgt}} (\text{PA} \cdot \text{NORM3})_H J_H} \quad (28)$$

This is the equation used to make the cross section calculations found in the following presentation of data.

The equation above points out where the likely sources of error may be found. The error bars presented in the data are errors due only to the statistical and fitting errors in the extracted peak areas estimated by NEWFIT. There are additional uncertainties which are estimated to be a total of  $\sim \pm 7\%$  due to several sources. The chamber efficiencies have uncertainties of  $\pm 3\%$ , the pion survival fraction from the path length corrections,  $\pm 3\%$ , and the spectrometer's solid angle variation with momentum in the spectrometer,  $\pm 2\%$ . This last uncertainty was probably an overestimation since the pion events of the elastic and inelastic peaks in the Q-value spectra had  $\delta_s$ 's corresponding to the flat region of the spectrometer's acceptance curve. Further uncertainties include a  $\pm 3\%$  error in the channel beam monitoring, and  $\pm 3\%$  in the normalization to the  $\pi^+$  elastic scattering from hydrogen.

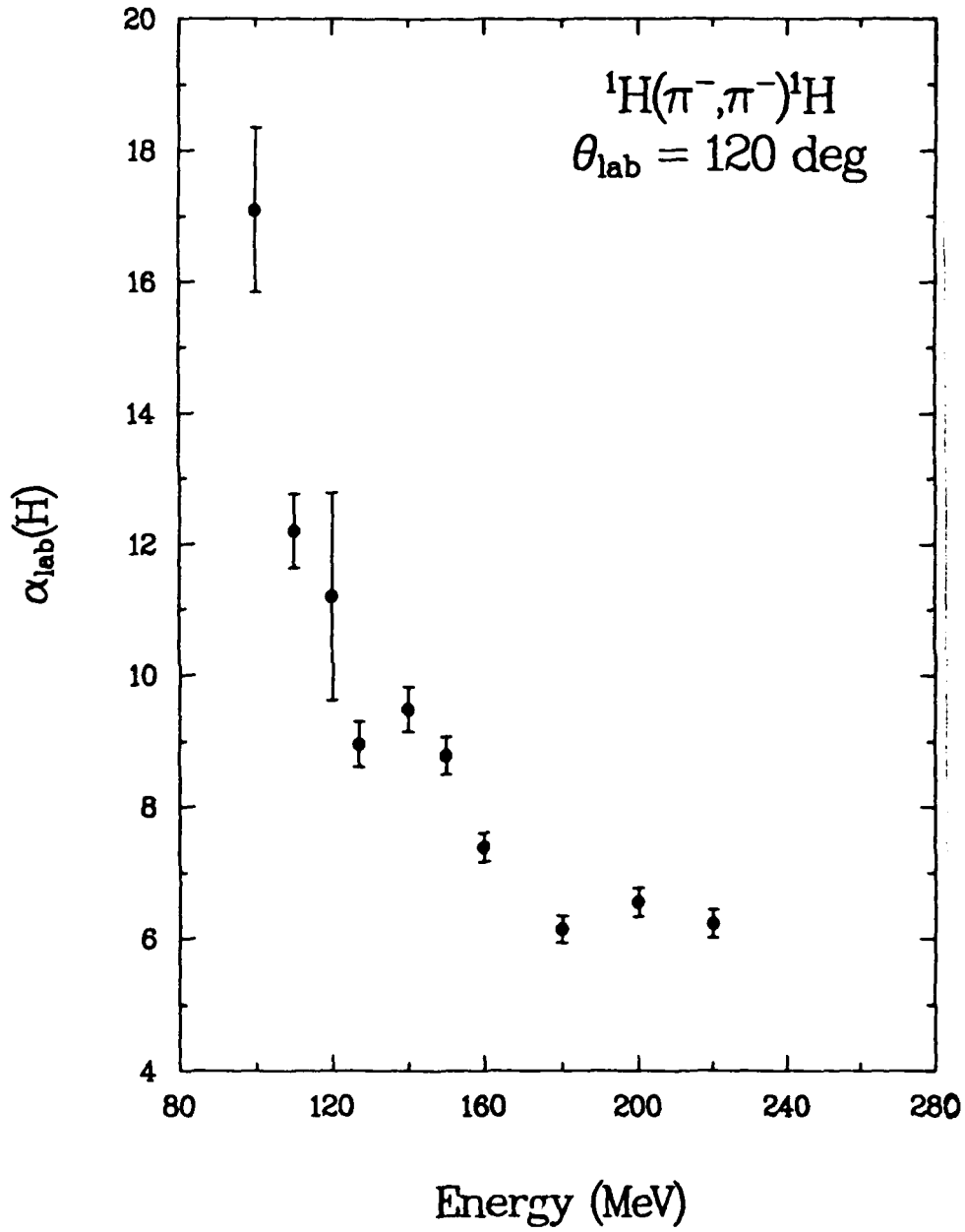


Figure 21: Hydrogen normalization curves for  $\pi^-$  at  $\theta_{\text{lab}} = 120^\circ$ .

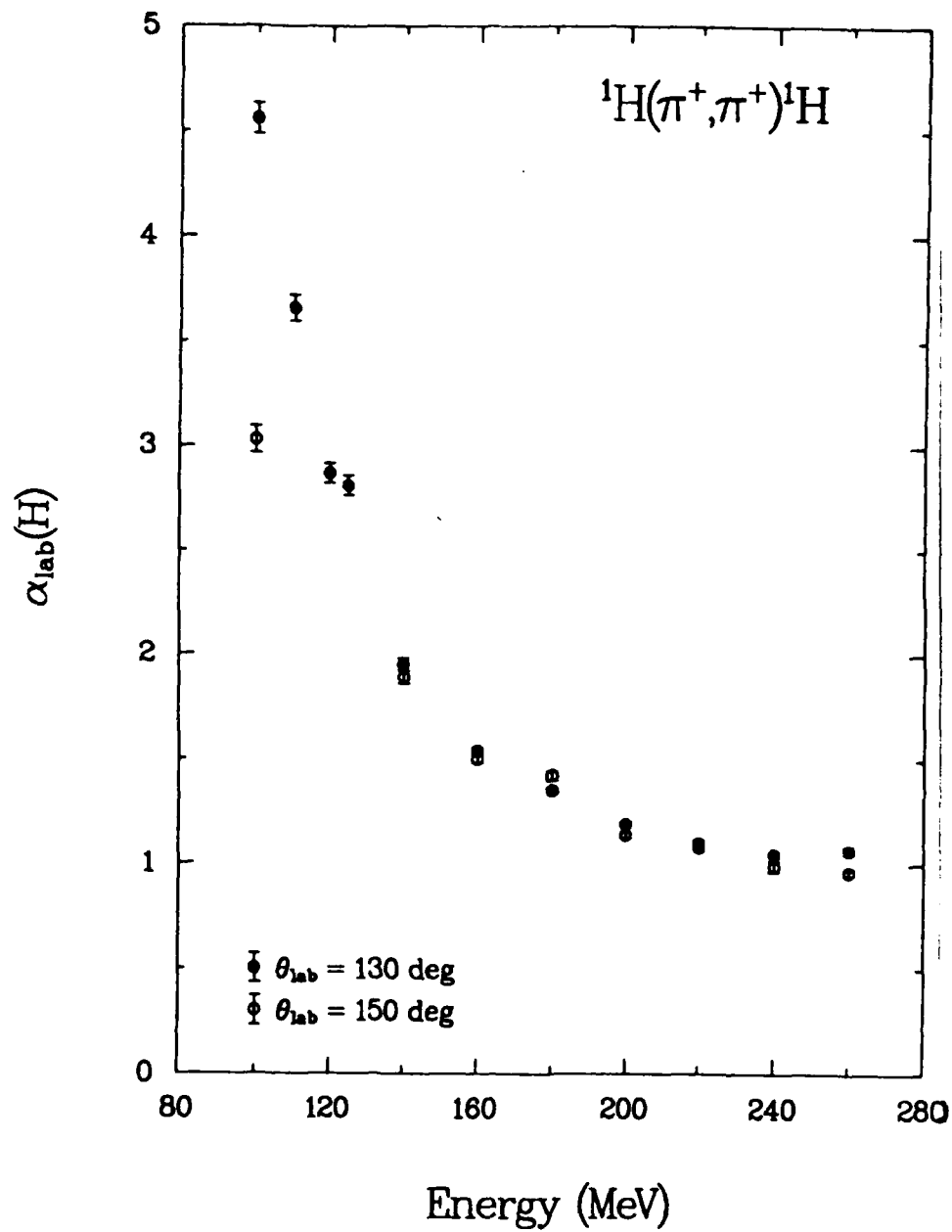


Figure 22: Hydrogen normalization curves for  $\pi^+$  at  $\theta_{\text{lab}} = 130^\circ$  and  $150^\circ$ .

### 3.3 Data Presentation

The data are presented in tabular form in the Appendix and in graphical form in the figures in this section. The scattering angles at which this data was taken is in keeping with the objective of the experiment, that is, the measurement of large angle scattering data. The incident pion energies range from 100 to 260 MeV, thus covering nearly the entire energy region of the  $\Delta(1232)$  resonance. The targets,  $^{28}\text{Si}$  and  $^{40}\text{Ca}$ , were chosen because these are  $N=Z$  nuclei for which the theoretical models are valid. These nuclei are simple to treat theoretically because they do not contain additional spin terms. Also, with a spin-zero target, the higher the  $Z$  of the target the easier it is to see the small differences between  $\pi^+$  and  $\pi^-$  scattering effects.  $^{40}\text{Ca}$  was used in particular because it is the highest  $N=Z$  atom available.

Figure 23 shows an energy distribution of the differential cross sections for  $\pi^+$  and  $\pi^-$  elastic scattering from  $^{40}\text{Ca}$  at the angle  $\theta_{cm}=175^\circ$ . The distribution exhibits a decreasing cross section with increasing energy and displays peaking at  $\sim 140$  and  $\sim 180$  MeV for  $\pi^+$  and at  $\sim 120$  MeV for  $\pi^-$ . Figure 24 shows an energy distribution of the differential cross sections for  $\pi^+$  and  $\pi^-$  elastic scattering from  $^{28}\text{Si}$  at the angle  $\theta_{cm}=175^\circ$ . Again the distribution exhibits a decreasing cross section with increasing energy but displays peaking at  $\sim 110$  and  $\sim 155$  MeV for  $\pi^+$ , however, there isn't enough data for  $\pi^-$  to determine the existence of a peak. Figures 25–27 show similar energy distributions for the first three excited states of  $^{28}\text{Si}$  ( $2^+$ , 1.78 MeV,  $4^+$ , 4.62 MeV,  $3^-$ , 6.88 MeV). The same decreasing trend in the cross section

is apparent in each distribution, though, any structure that may be inherent in the distribution disappears with higher excited states.

The angular distributions of the differential cross sections for  $\pi^+$  elastic scattering from  $^{28}\text{Si}$  at incident pion energies of  $T_\pi=130, 180,$  and  $226$  MeV are shown in Figs. 28-30. For comparison, cross sections from [Pr-79] measured at smaller angles is plotted to show continuity in the angular distribution. Since no theoretical calculations are available for  $^{28}\text{Si}$  at this time we may consider the trend of the aforementioned cross sections as it has been accurately predicted by currently existing codes which are known to be valid at forward scattering angles. We find in the elastic scattering case a well matched angular distribution across all three incident pion energies. The forward angle data for  $T_\pi$  is a bit spotty, however, theoretical predictions show a peak between two minimums at  $100^\circ$  and  $140^\circ$  and thus, taking the variation of data in this region into account the transition to the backangle data doesn't look too bad.

Figures 31-33 show the angular distributions of the differential cross sections for  $\pi^+$  inelastic scattering to the  $2^+, 1.78$  MeV level of  $^{28}\text{Si}$  at incident pion energies of  $T_\pi=130, 180,$  and  $226$  MeV. As for the elastic scattering case forward angle data is presented along with backangle data for continuity. For this excited state there is too large a gap in the data for  $T_\pi=130$  MeV to recognize any continuity and the data for  $T_\pi=226$  MeV make it difficult to spot a trend although the magnitudes seem to be joining. There is a good match in spectral shape for  $T_\pi=180$  MeV but the magnitude seems a factor of two different.

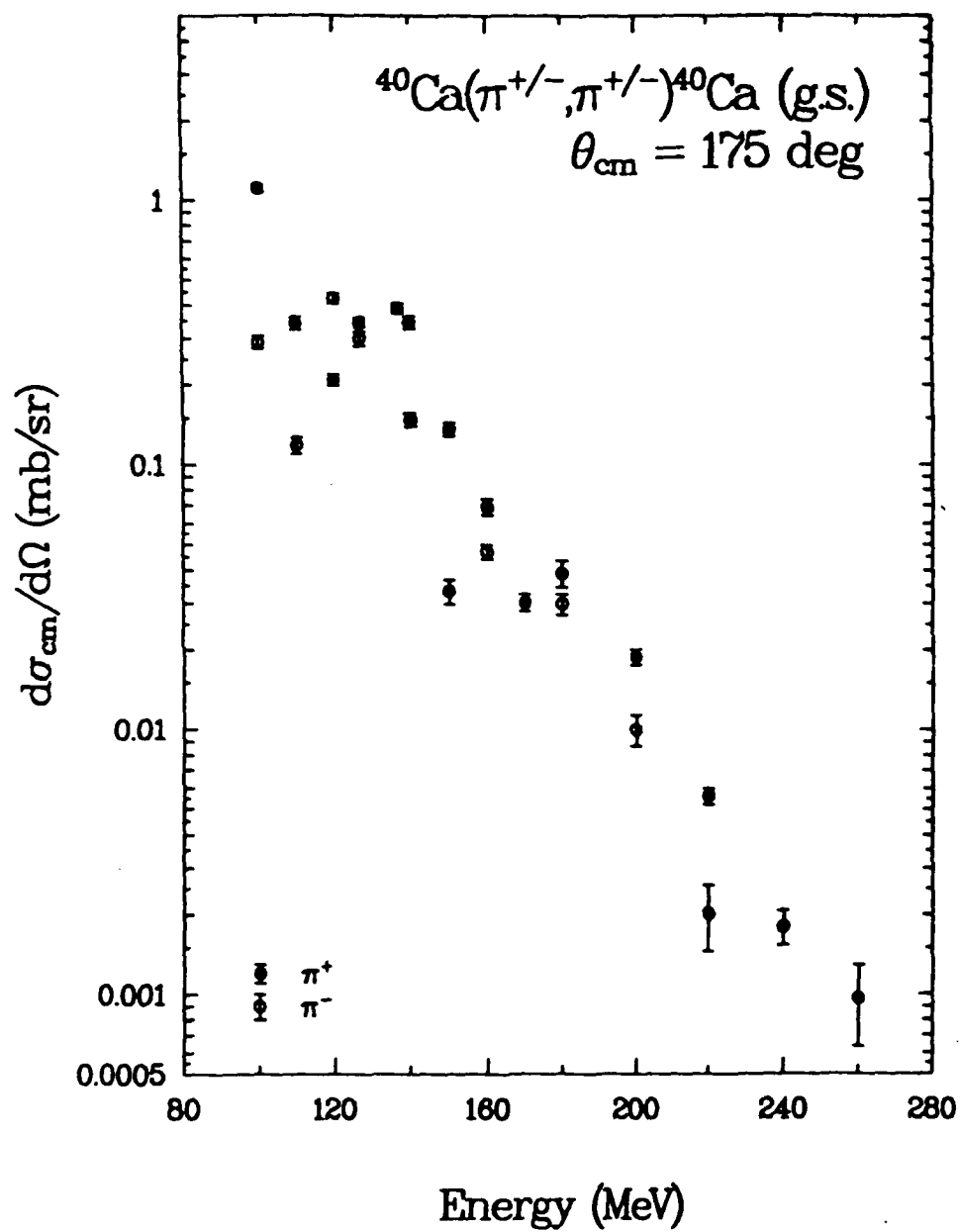


Figure 23: Energy distribution of the differential cross sections for  $\pi^+$  and  $\pi^-$  elastic scattering from  $^{40}\text{Ca}$  at the angle  $\theta_{\text{cm}} = 175^\circ$ .



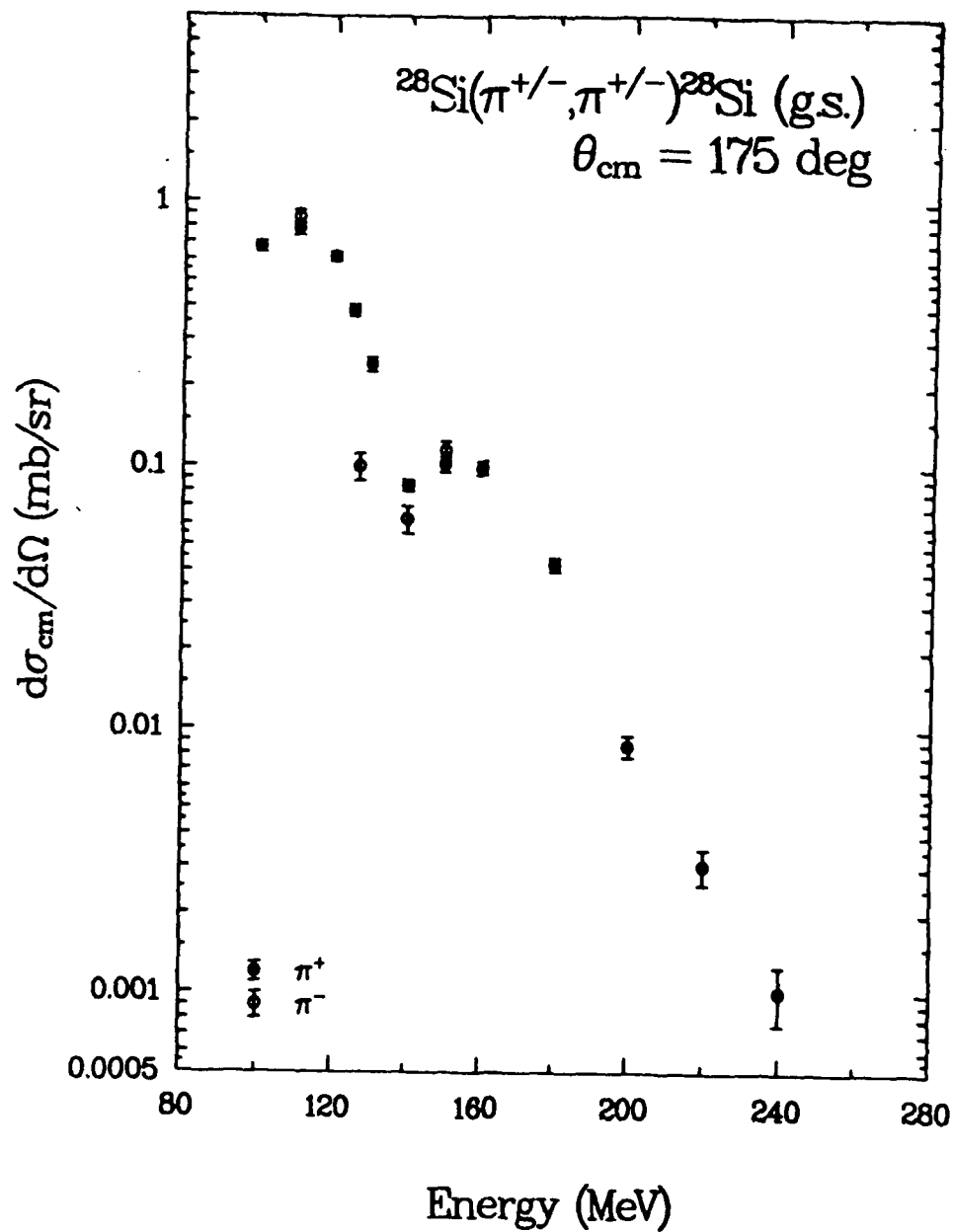


Figure 24: Energy distribution of the differential cross sections for  $\pi^+$  and  $\pi^-$  elastic scattering from  $^{28}\text{Si}$  at the angle  $\theta_{\text{cm}} = 175^\circ$ .

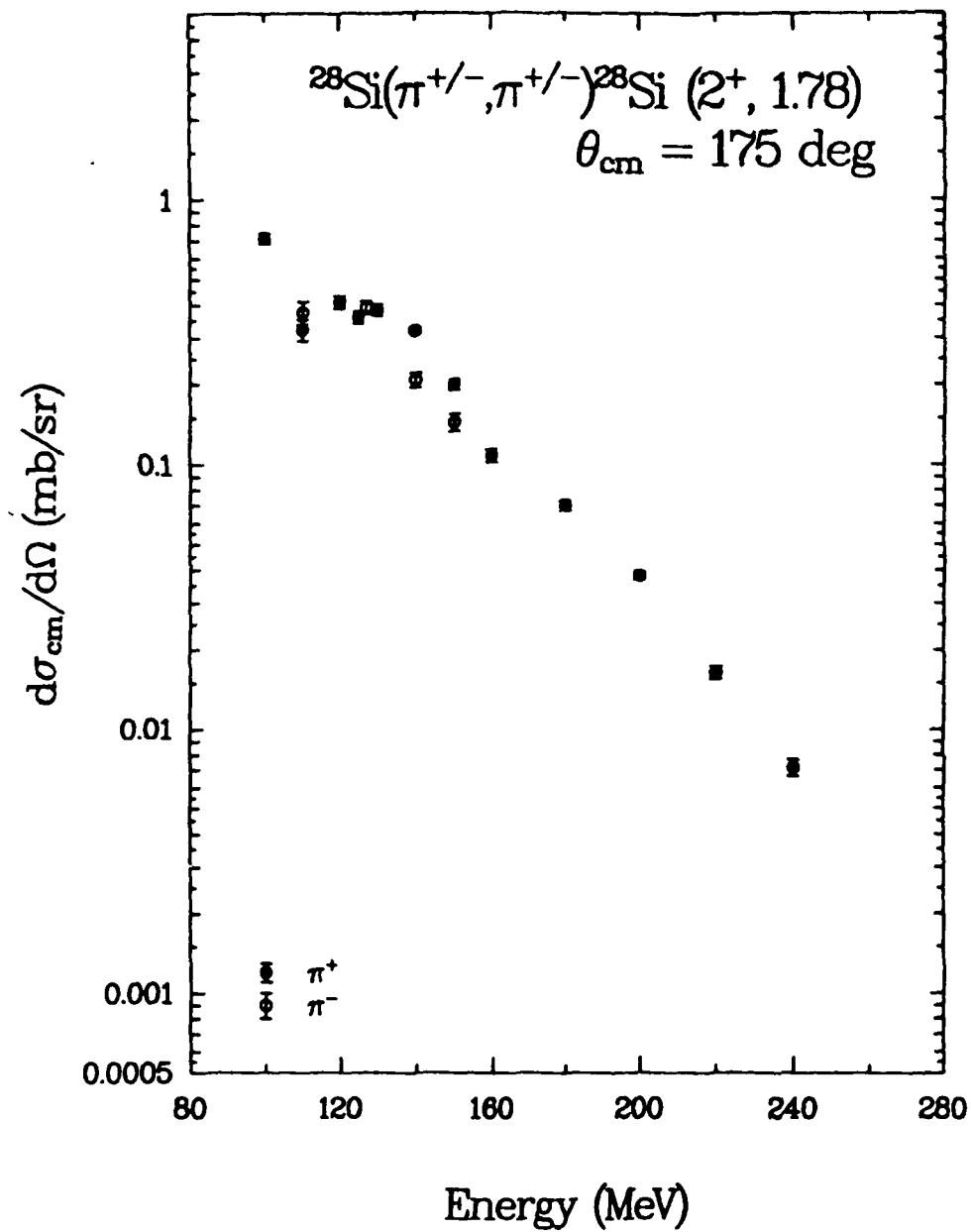


Figure 25: Energy distribution of the differential cross sections for  $\pi^+$  and  $\pi^-$  inelastic scattering to the  $2^+$ , 1.78 MeV excited state of  $^{28}\text{Si}$  at the angle  $\theta_{\text{cm}} = 175^\circ$ .

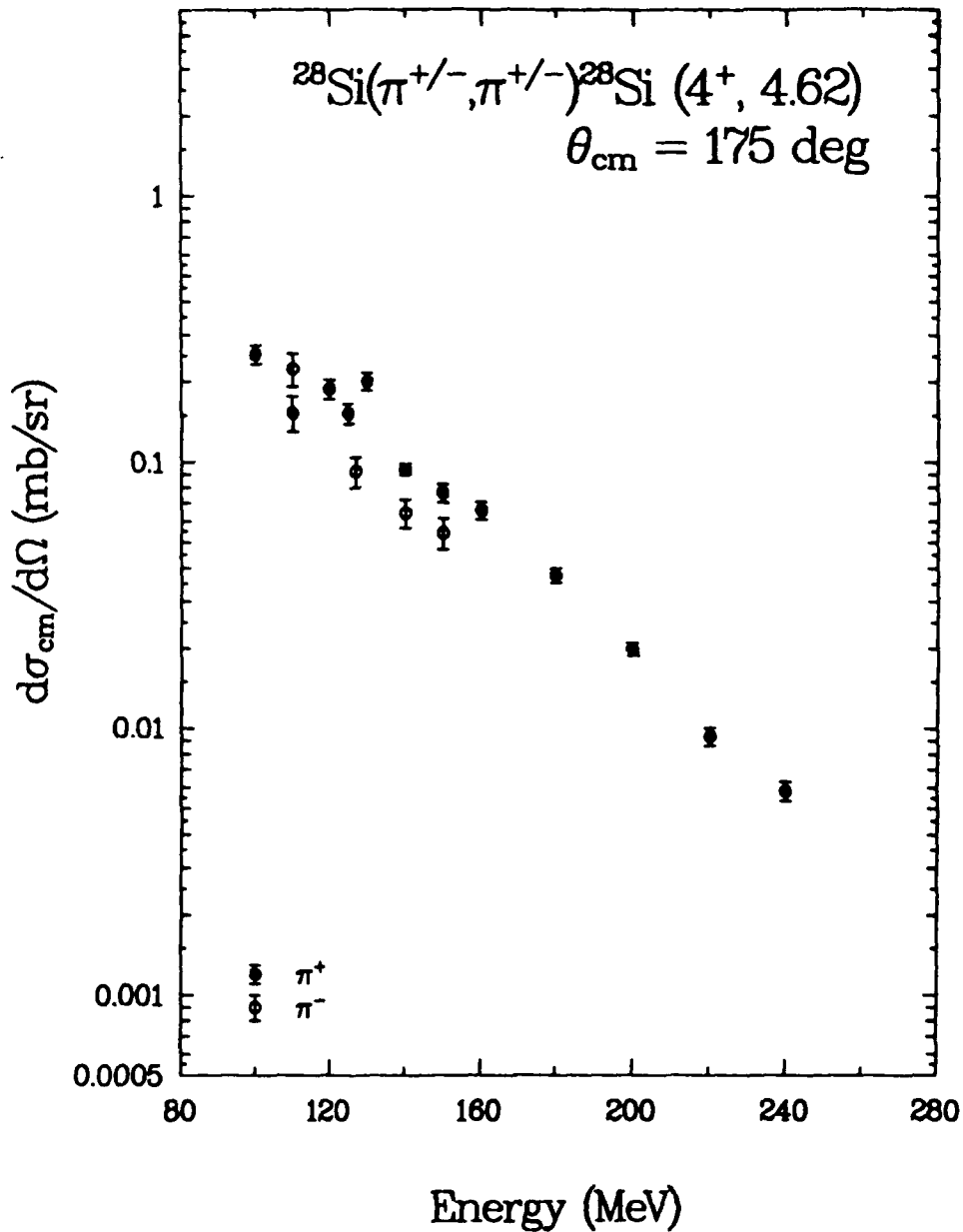


Figure 26: Energy distribution of the differential cross sections for  $\pi^+$  and  $\pi^-$  inelastic scattering to the  $4^+$ , 4.62 MeV excited state of  $^{28}\text{Si}$  at the angle  $\theta_{\text{cm}} = 175^\circ$ .

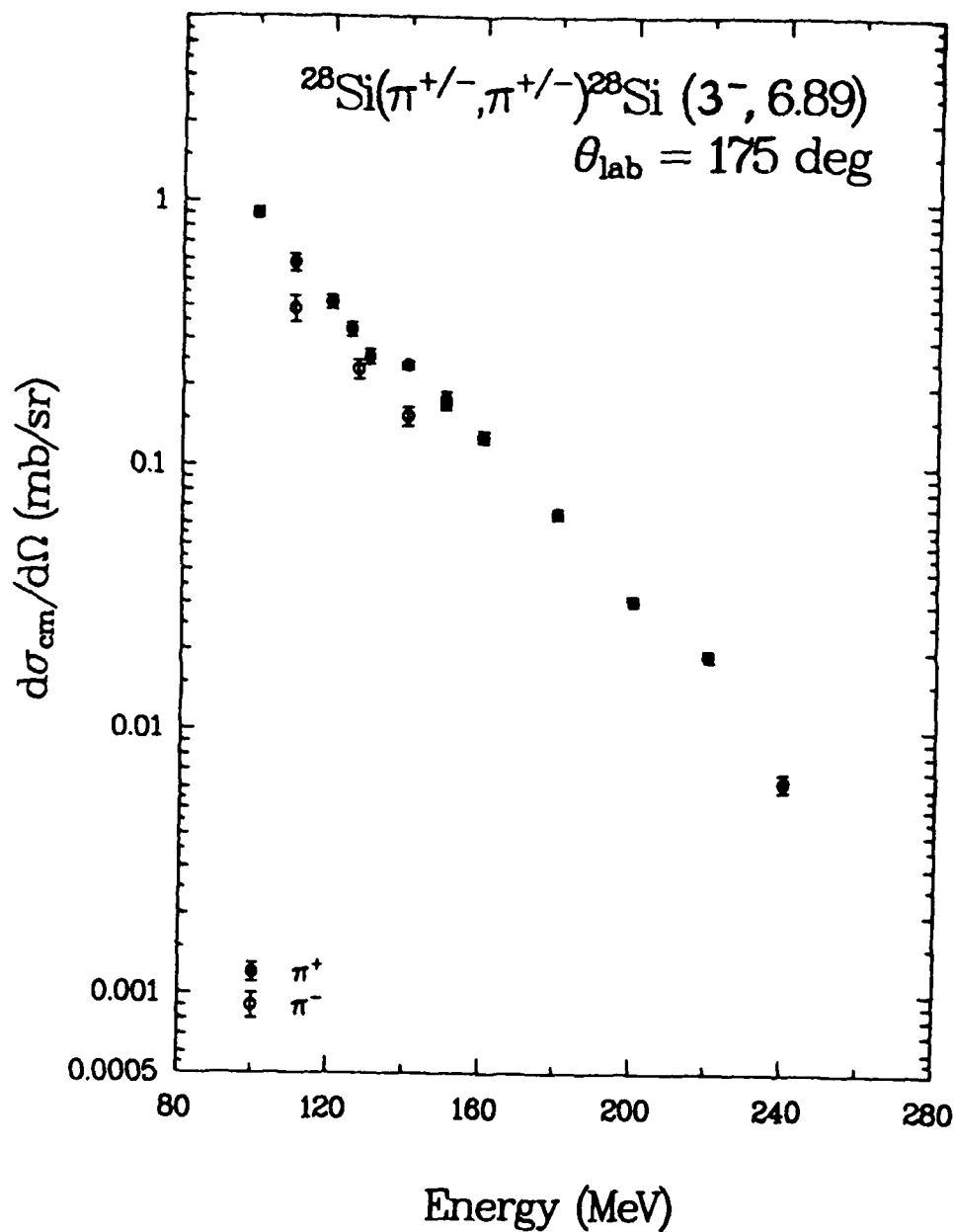


Figure 27: Energy distribution of the differential cross sections for  $\pi^+$  and  $\pi^-$  inelastic scattering to the  $3^-$ , 6.88 MeV excited state of  $^{28}\text{Si}$  at the angle  $\theta_{\text{cm}} = 175^\circ$ .

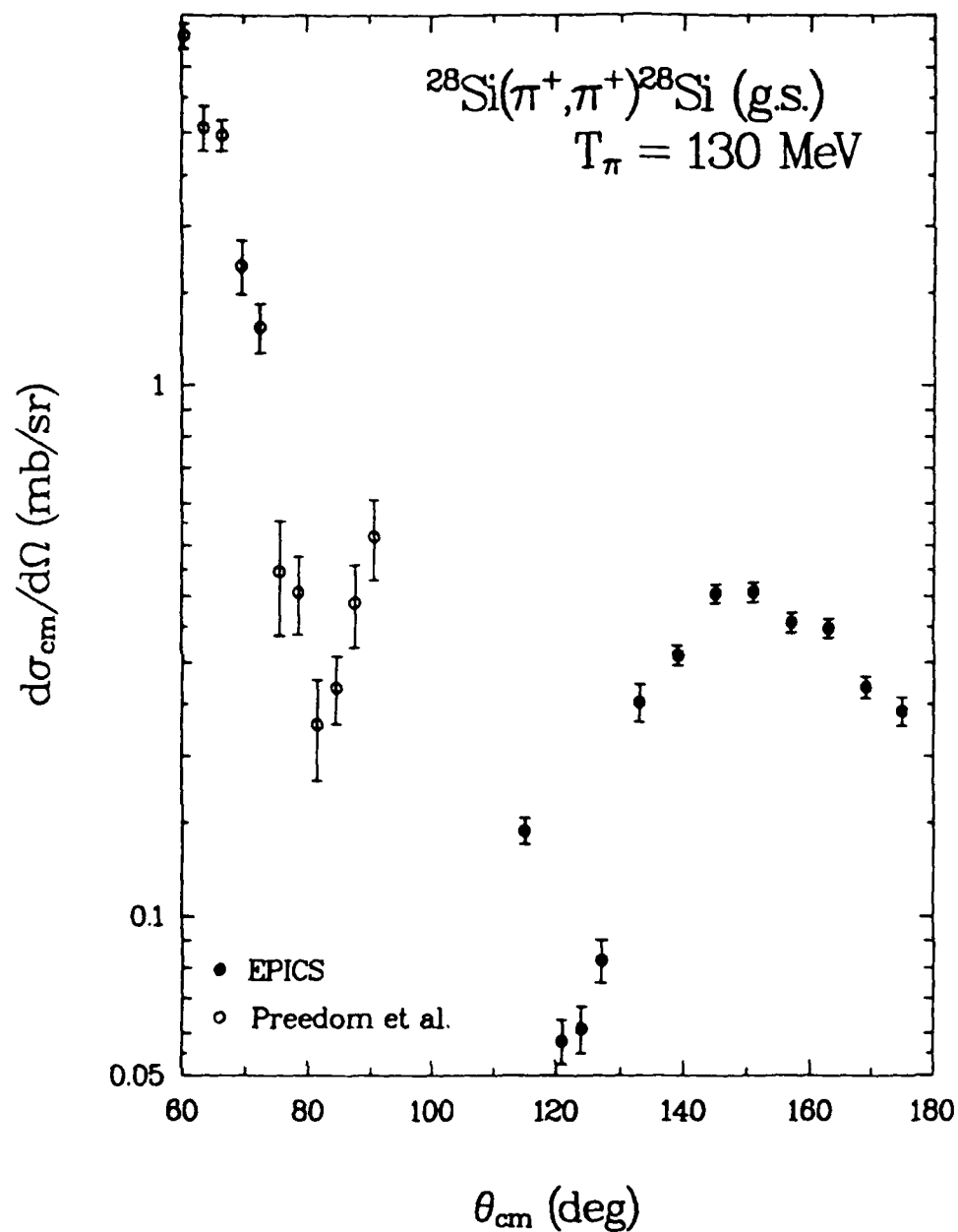


Figure 28: Angular distribution of the differential cross sections for  $\pi^+$  elastic scattering from  $^{28}\text{Si}$  at the energy  $T_\pi=130$  MeV.

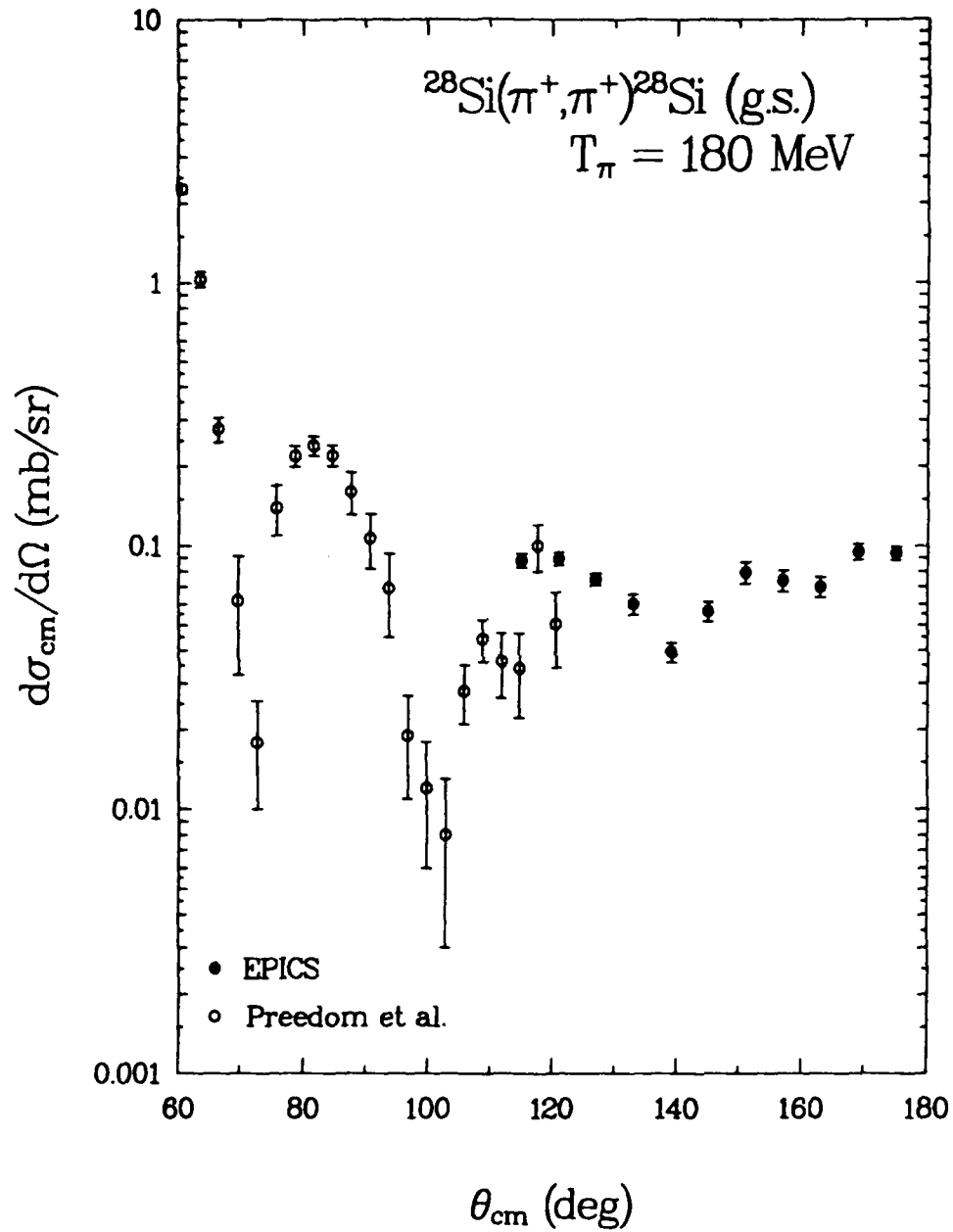


Figure 29: Angular distribution of the differential cross sections for  $\pi^+$  elastic scattering from  $^{28}\text{Si}$  at the energy  $T_\pi=180$  MeV.

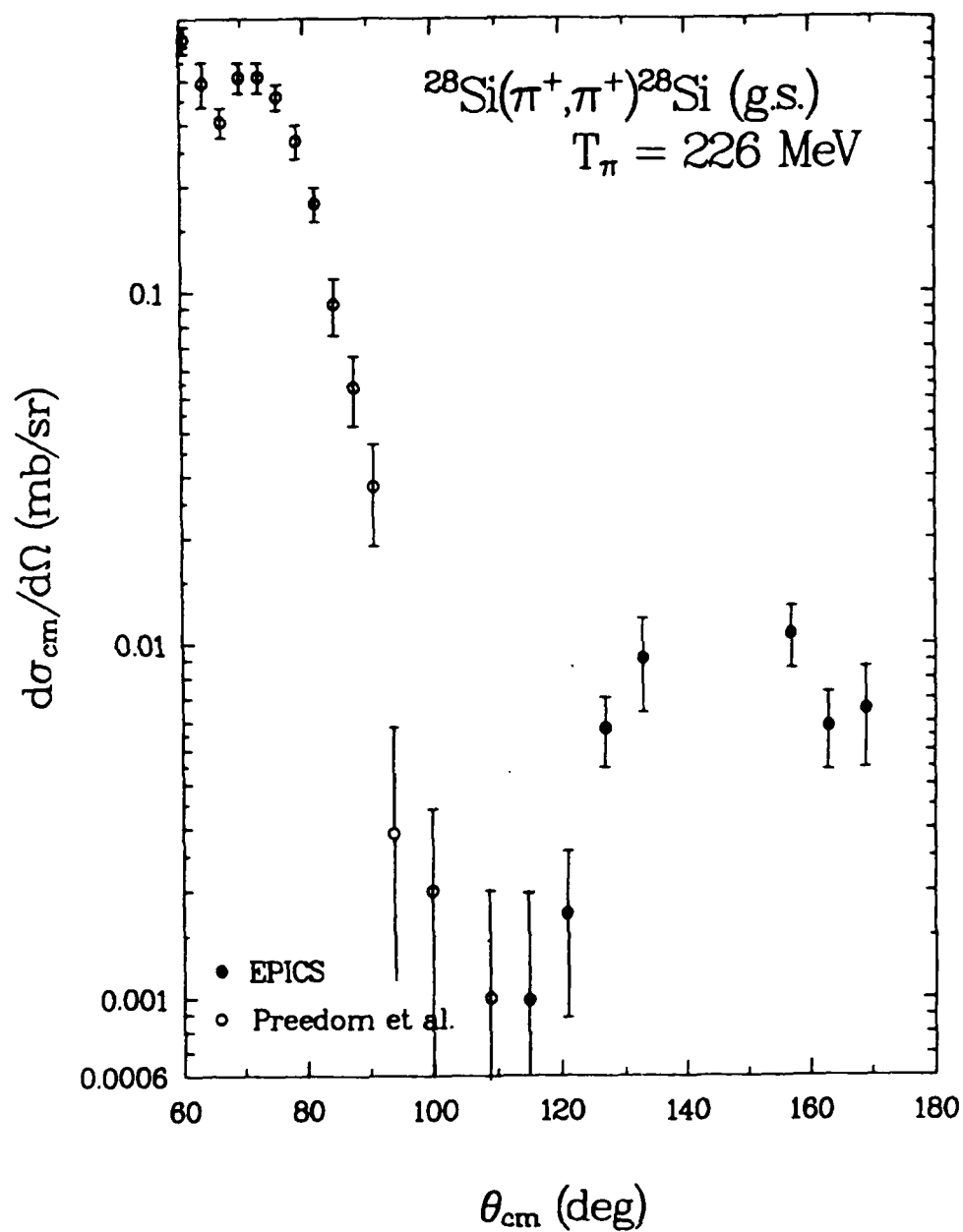


Figure 30: Angular distribution of the differential cross sections for  $\pi^+$  elastic scattering from  $^{28}\text{Si}$  at the energy  $T_\pi=226$  MeV.

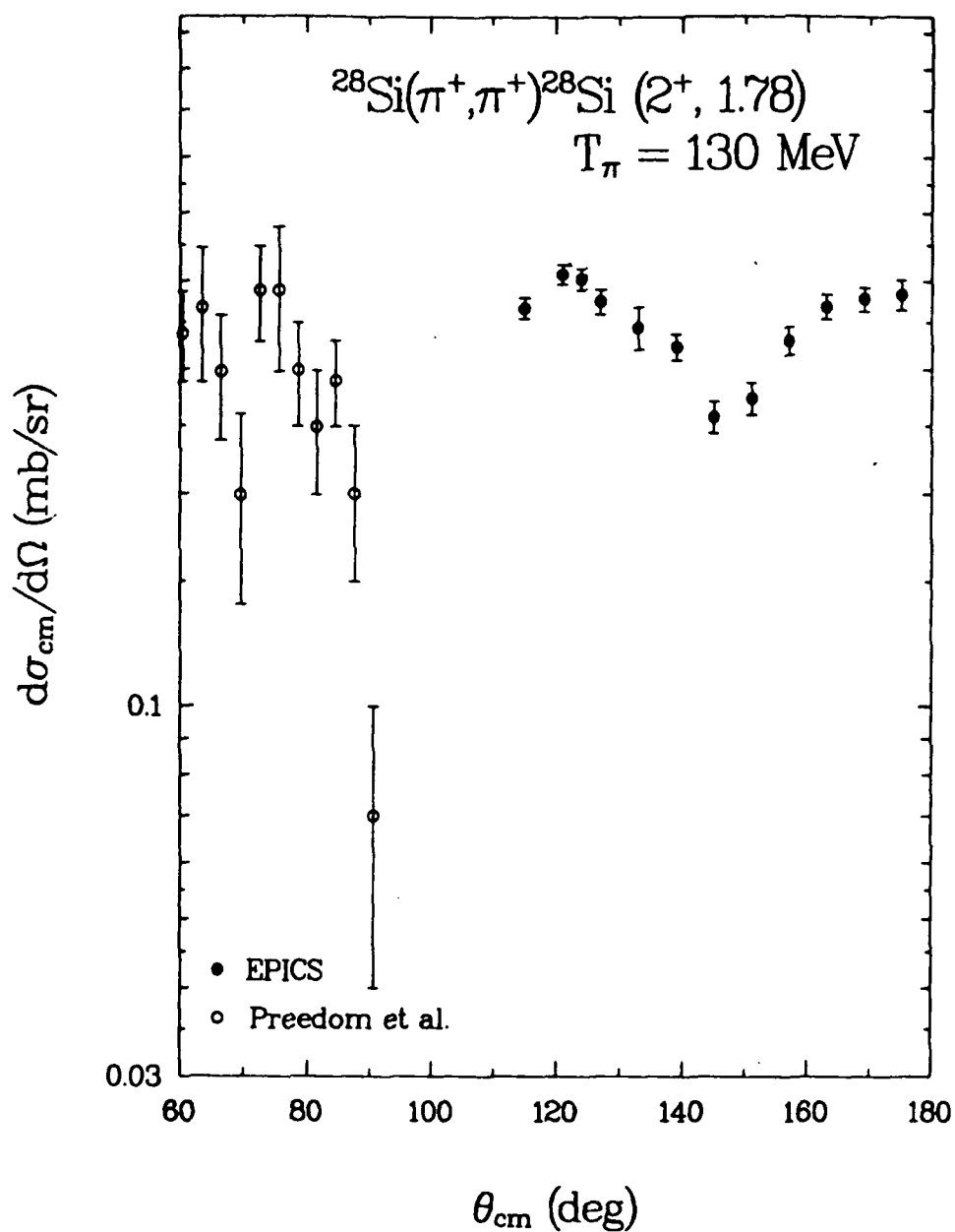


Figure 31: Angular distribution of the differential cross sections for  $\pi^+$  inelastic scattering to the  $2^+$ , 1.78 MeV level of  $^{28}\text{Si}$  at the energy  $T_\pi = 130 \text{ MeV}$ .



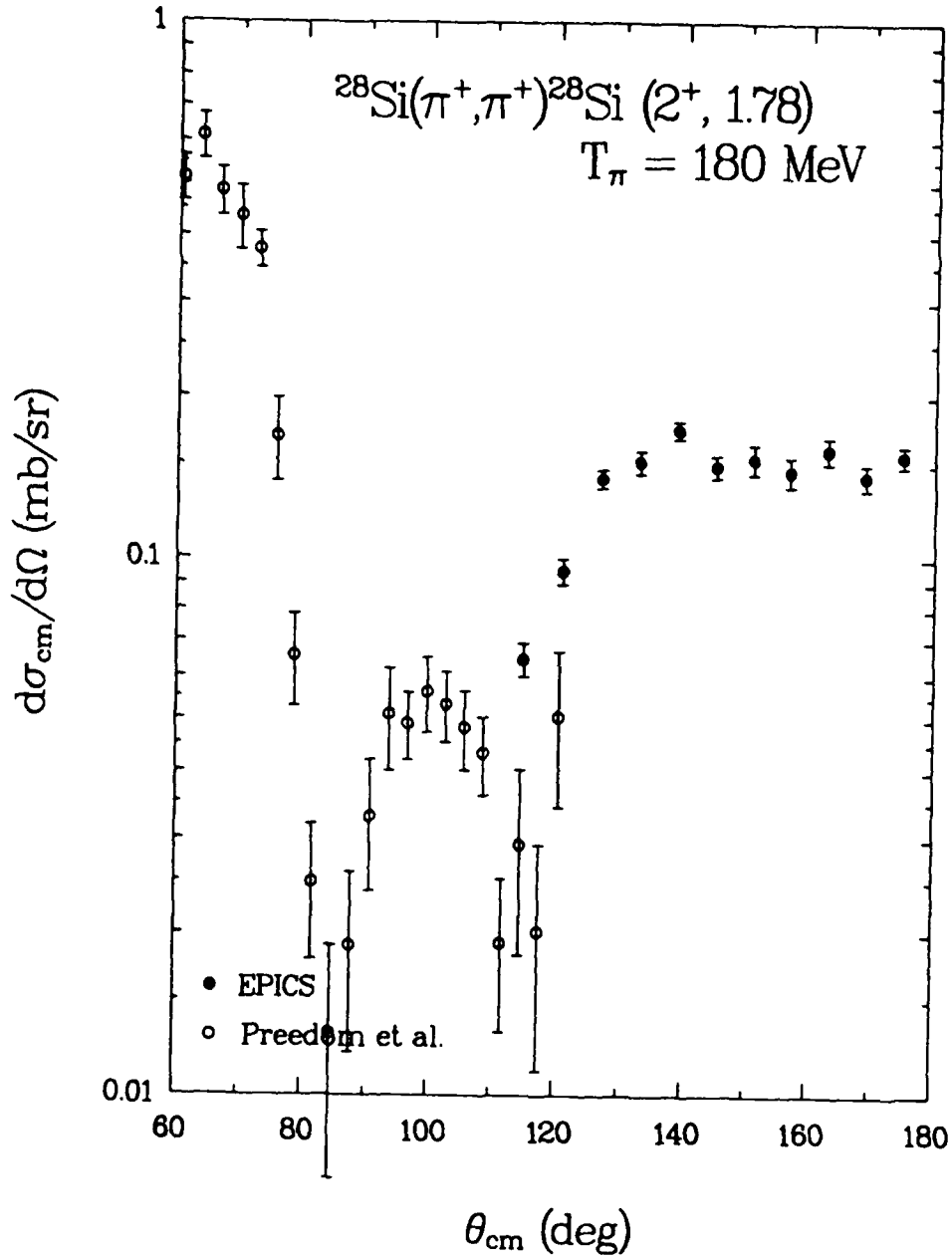


Figure 32: Angular distribution of the differential cross sections for  $\pi^+$  inelastic scattering to the  $2^+$ , 1.78 MeV level of  $^{28}\text{Si}$  at the energy  $T_\pi=180$  MeV.

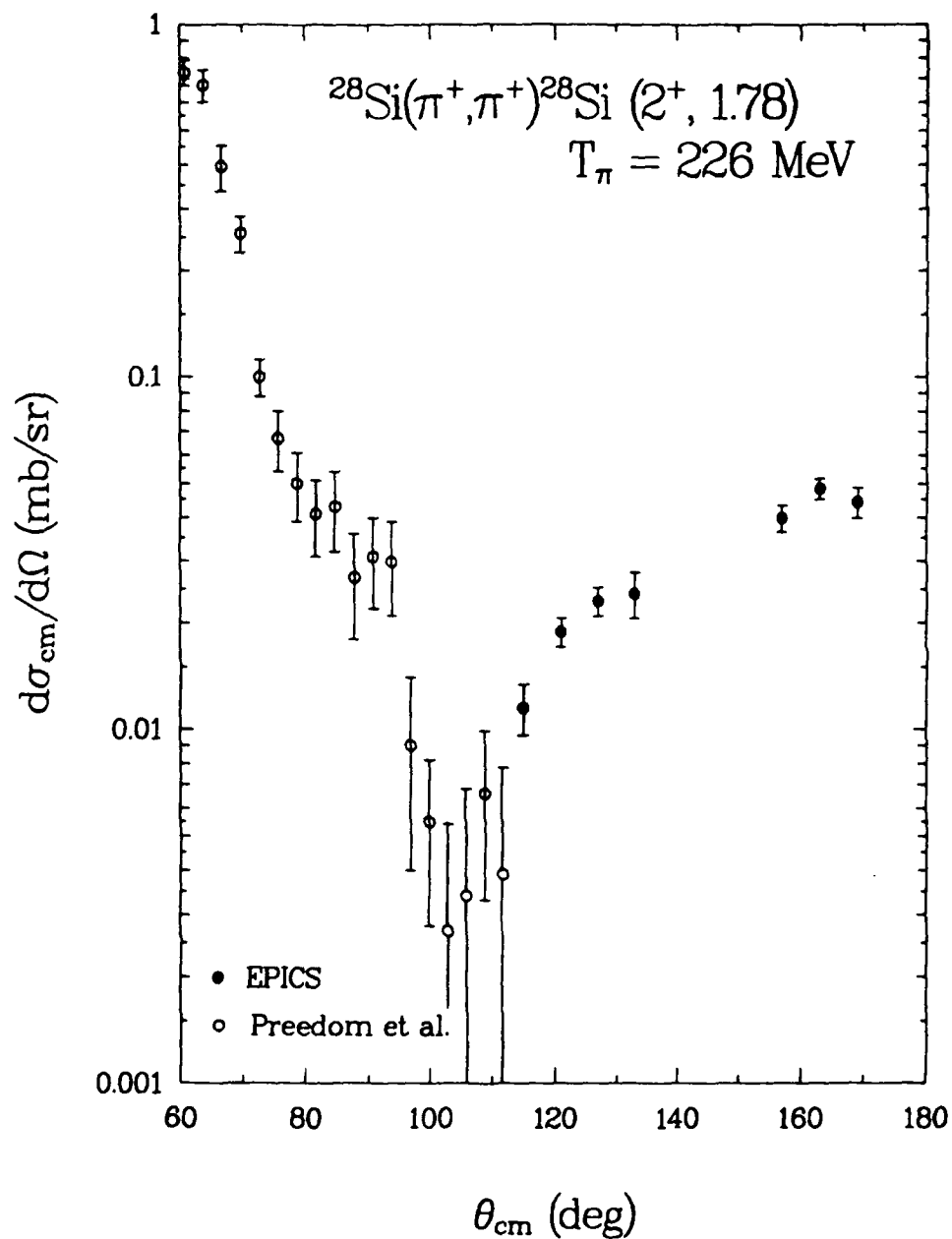


Figure 33: Angular distribution of the differential cross sections for  $\pi^+$  inelastic scattering to the  $2^+$ , 1.78 MeV level of  $^{28}\text{Si}$  at the energy  $T_\pi=226 \text{ MeV}$ .

The angular distributions of the differential cross sections for  $\pi^+$  inelastic scattering to the  $4^+$ , 4.62 MeV level of  $^{28}\text{Si}$  at incident pion energies of  $T_\pi=130, 180,$  and  $226$  MeV are shown in Figs. 34-36. These figures also contain previously obtained forward angle data for comparison. As was the case for the  $2^+$  state the data for  $T_\pi=130$  MeV is too sparse to determine continuity in the data. For  $T_\pi=226$  MeV, however, there seems to be good agreement. But for  $T_\pi=180$  MeV the  $120^\circ$  cross section doesn't seem to fit the an otherwise smooth transition between forward and backangle data.

Figures 37-39 show the angular distributions of the differential cross sections for  $\pi^+$  inelastic scattering to the  $3^-$ , 6.88 MeV level of  $^{28}\text{Si}$  at incident pion energies of  $T_\pi=130, 180,$  and  $226$  MeV. A final comparison of forward and backangle data shows that the data trend for  $T_\pi=130$  MeV is again unobtainable. This time the agreement seems to be found at  $T_\pi=226$  MeV while the spectrum for  $T_\pi=180$  MeV doesn't match at all.

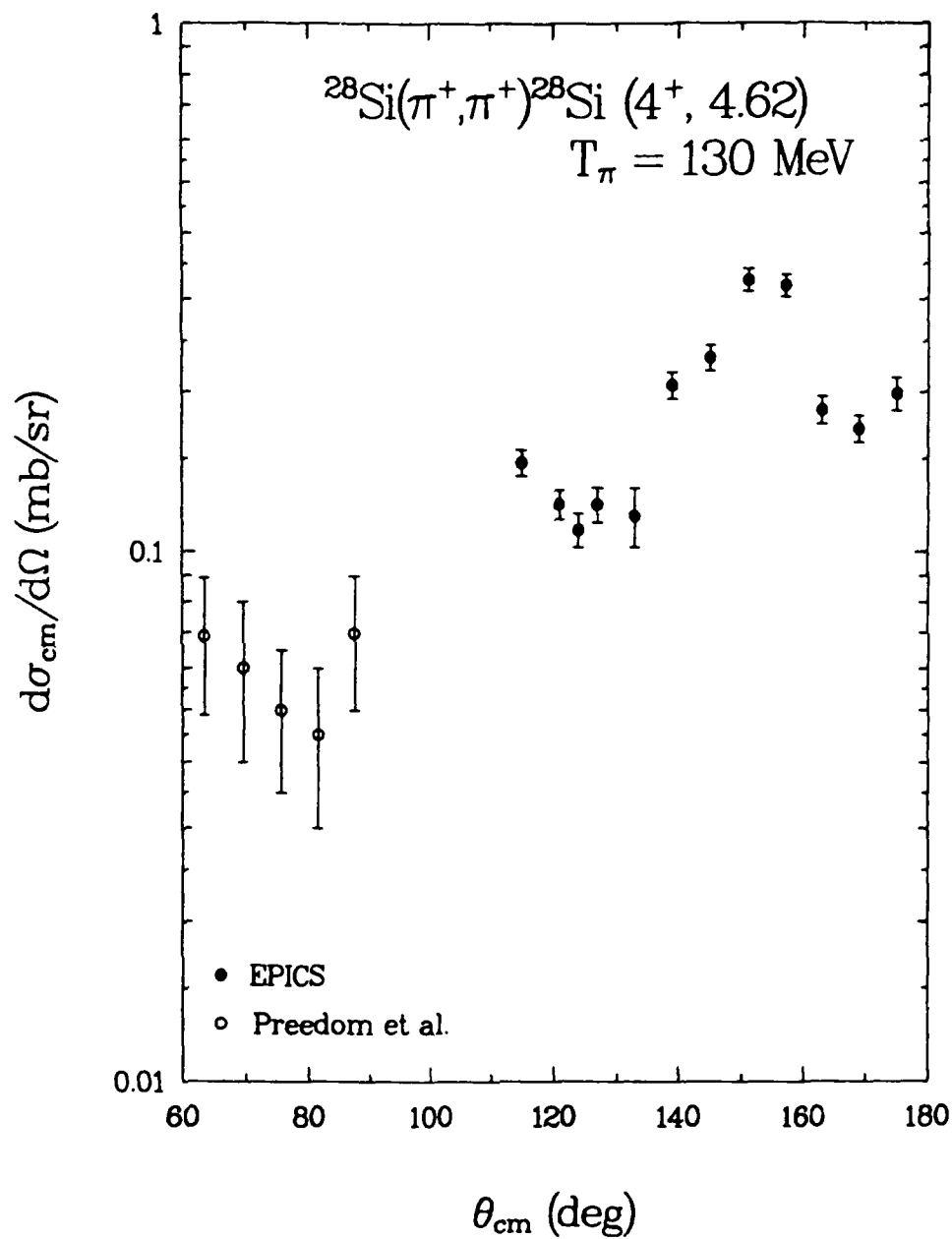


Figure 34: Angular distribution of the differential cross sections for  $\pi^+$  inelastic scattering to the  $4^+$ , 4.62 MeV level of  $^{28}\text{Si}$  at the energy  $T_\pi=130$  MeV.

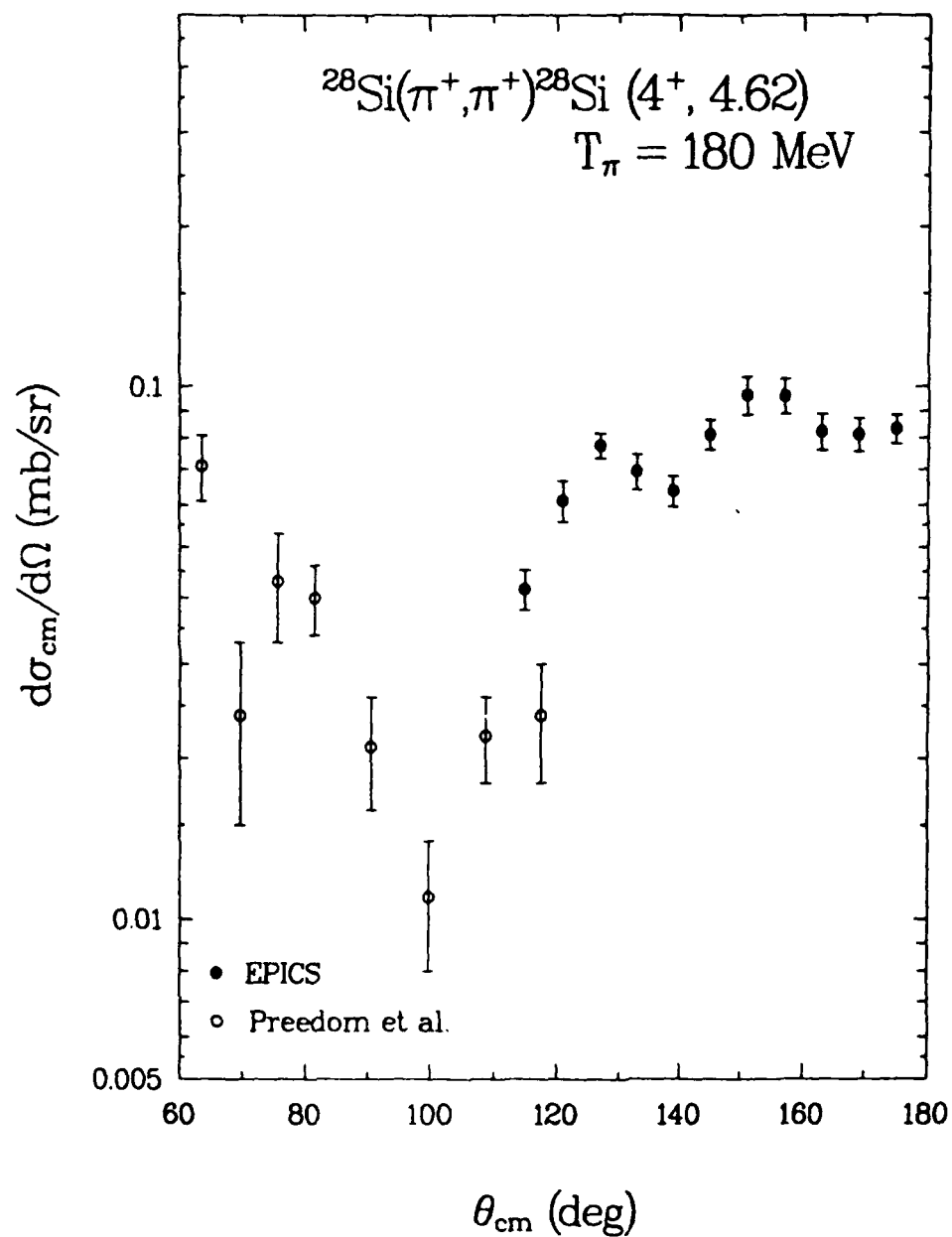


Figure 35: Angular distribution of the differential cross sections for  $\pi^+$  inelastic scattering to the  $4^+$ , 4.62 MeV level of  $^{28}\text{Si}$  at the energy  $T_\pi=180$  MeV.

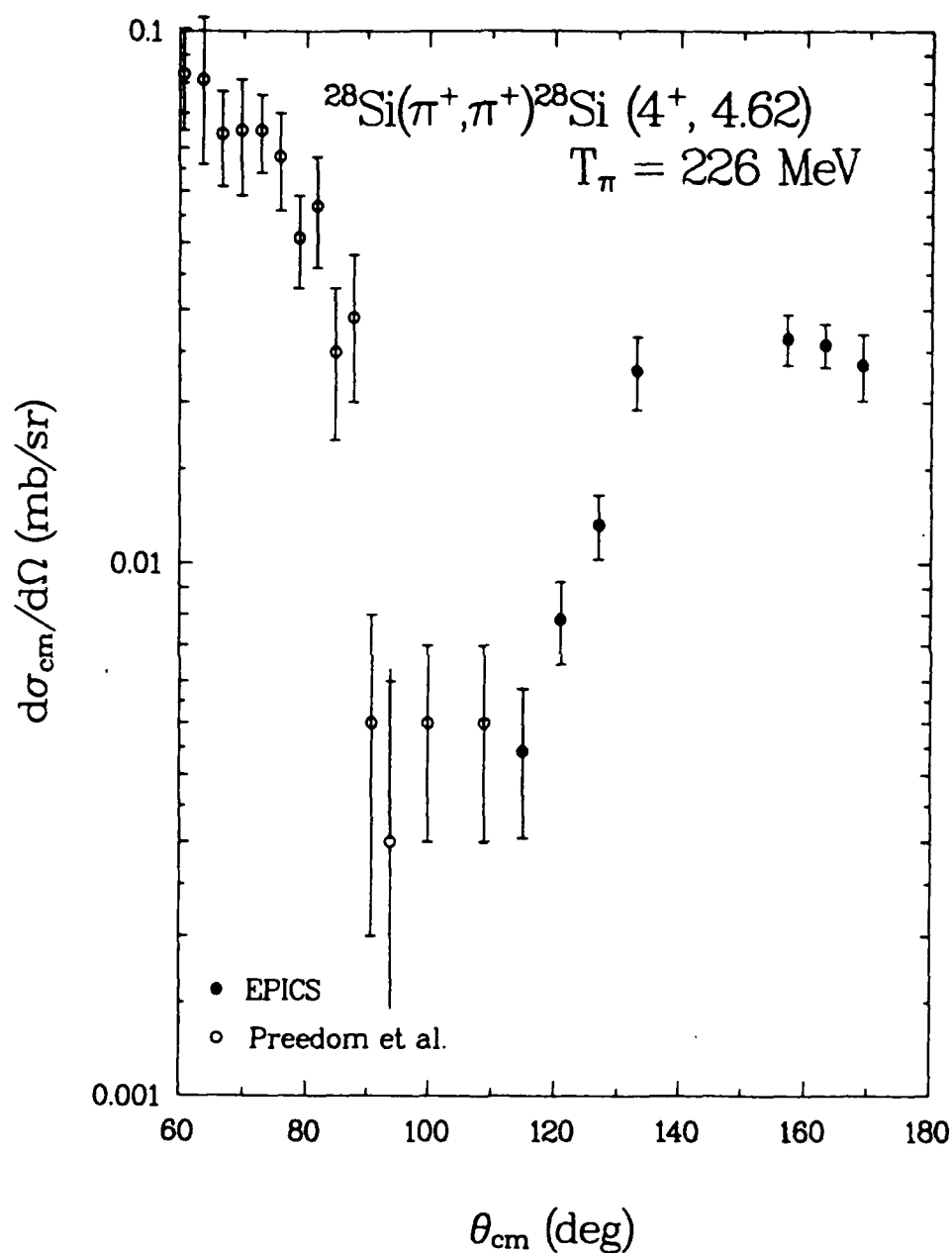


Figure 36: Angular distribution of the differential cross sections for  $\pi^+$  inelastic scattering to the  $4^+$ , 4.62 MeV level of  $^{28}\text{Si}$  at the energy  $T_\pi = 226 \text{ MeV}$ .

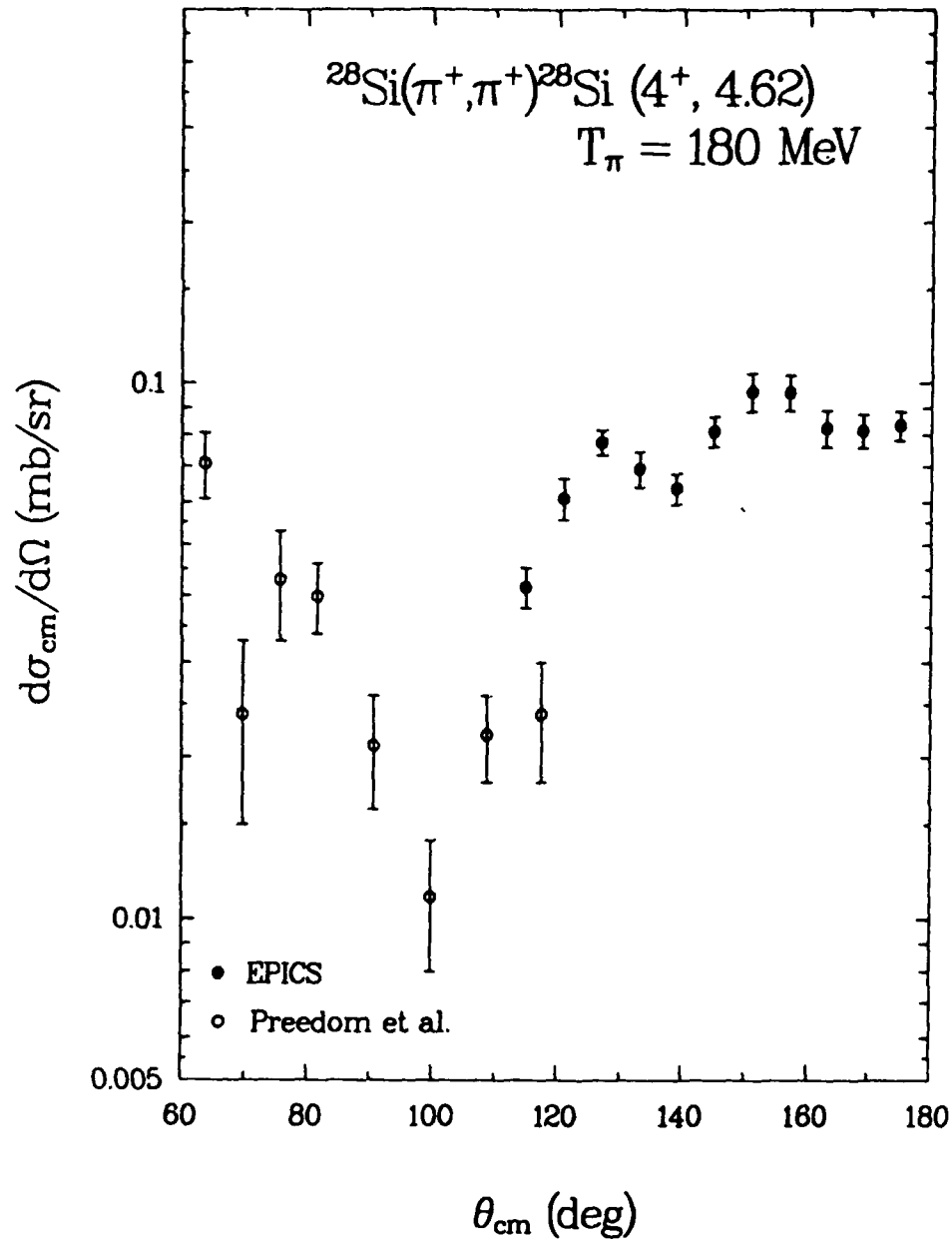


Figure 35: Angular distribution of the differential cross sections for  $\pi^+$  inelastic scattering to the  $4^+$ , 4.62 MeV level of  $^{28}\text{Si}$  at the energy  $T_\pi=180$  MeV.

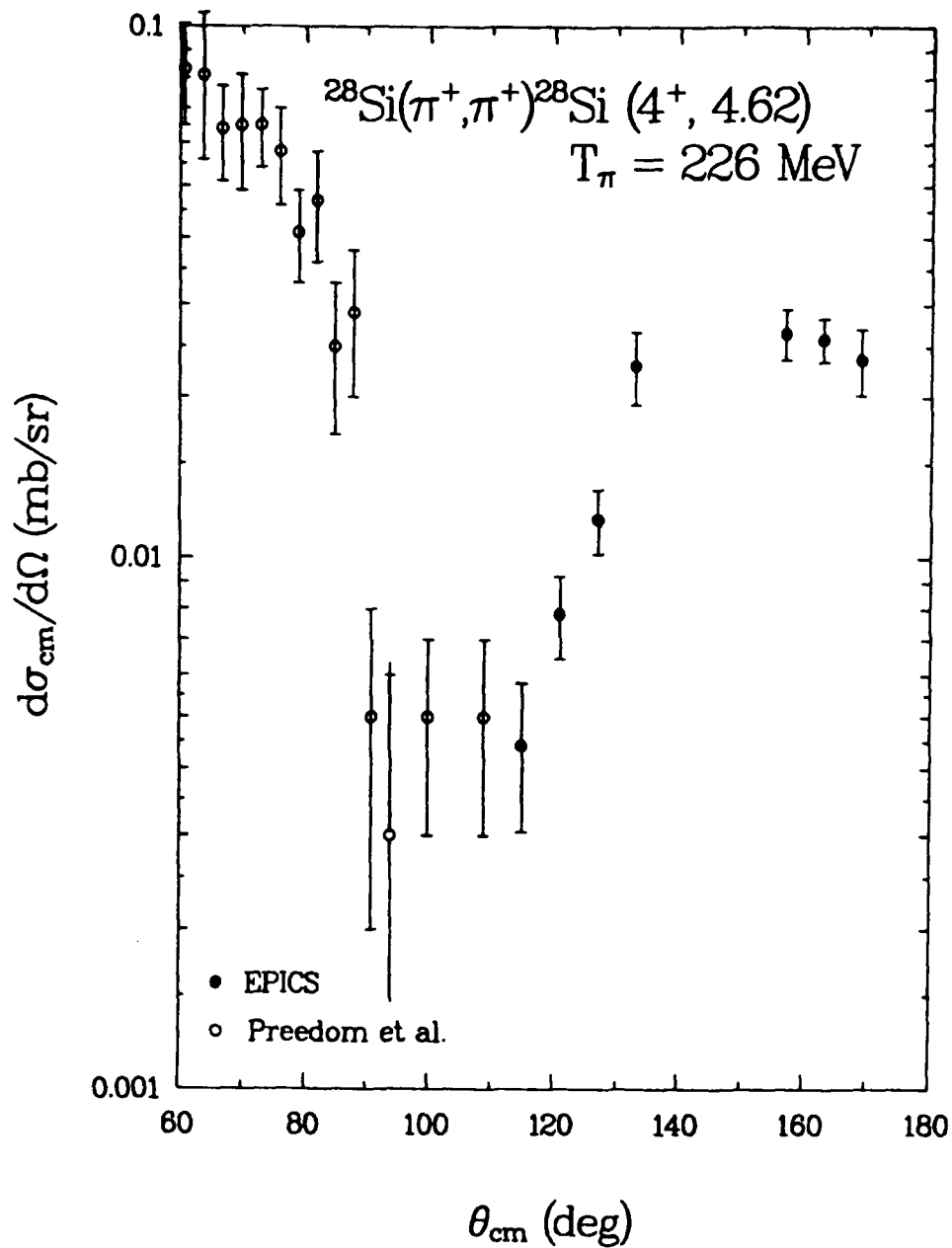


Figure 36: Angular distribution of the differential cross sections for  $\pi^+$  inelastic scattering to the  $4^+$ , 4.62 MeV level of  $^{28}\text{Si}$  at the energy  $T_\pi = 226 \text{ MeV}$ .



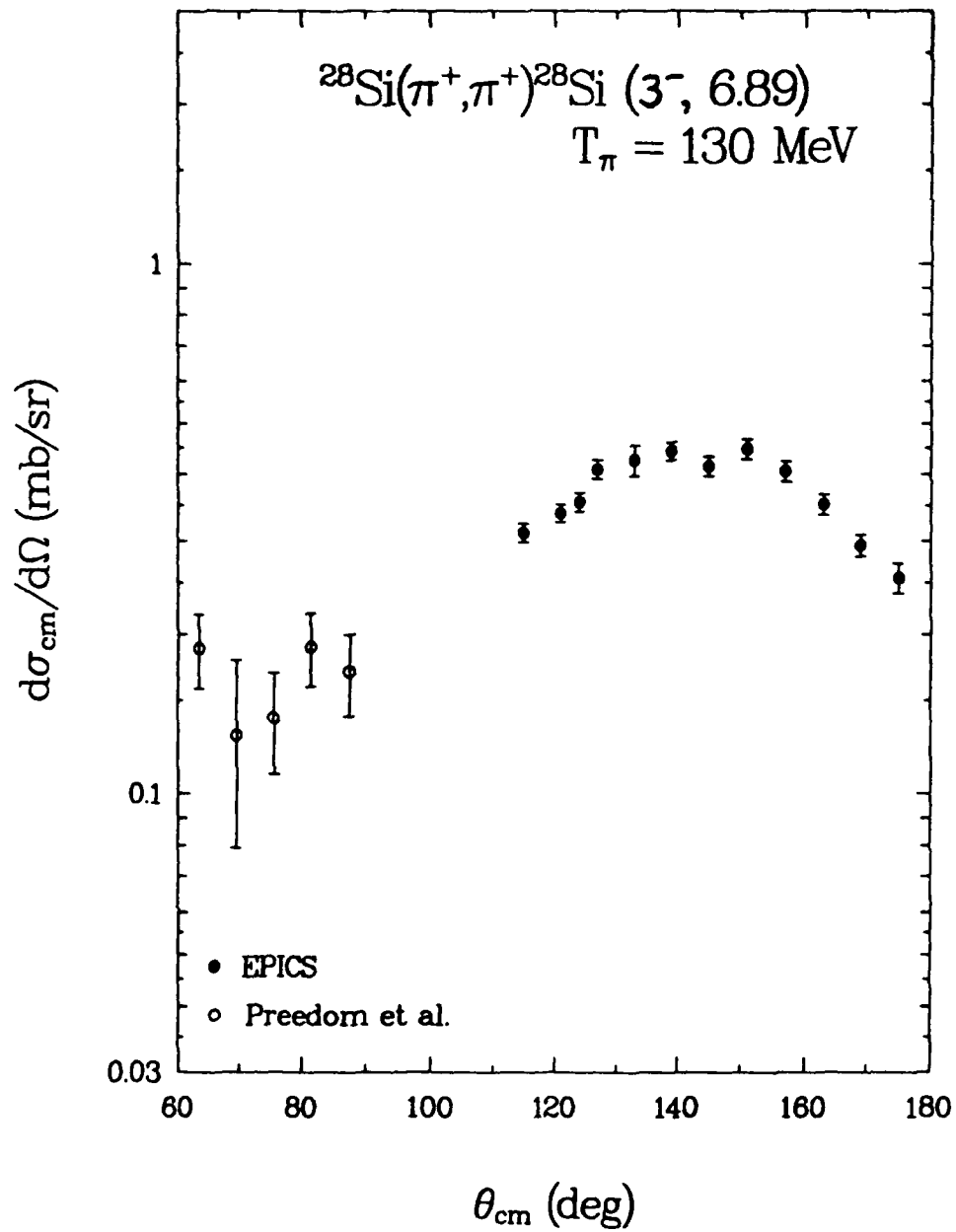


Figure 37: Angular distribution of the differential cross sections for  $\pi^+$  inelastic scattering to the  $3^-$ , 6.88 MeV level of  $^{28}\text{Si}$  at the energy  $T_\pi = 130$  MeV.

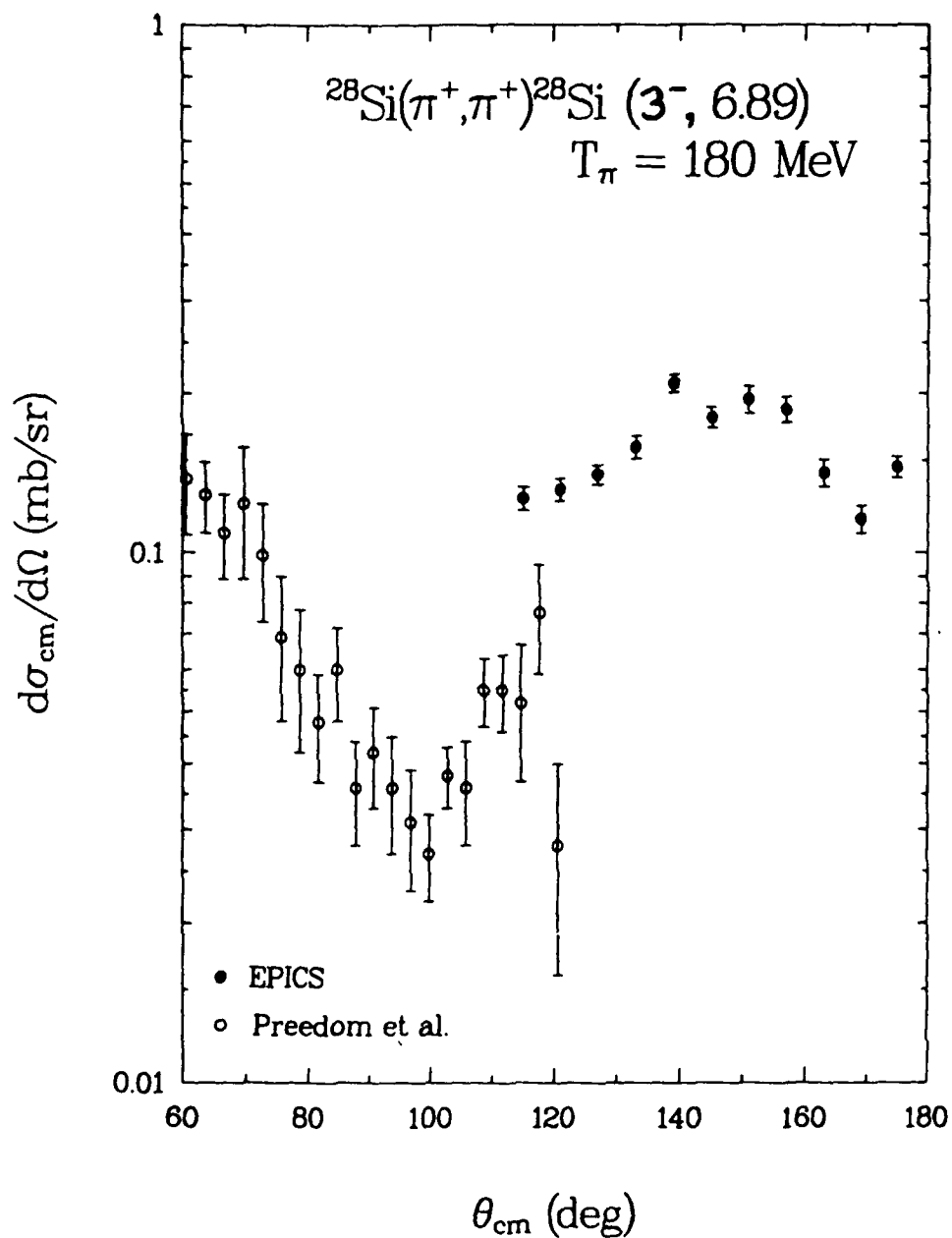


Figure 38: Angular distribution of the differential cross sections for  $\pi^+$  inelastic scattering to the  $3^-$ , 6.88 MeV level of  $^{28}\text{Si}$  at the energy  $T_\pi = 180 \text{ MeV}$ .

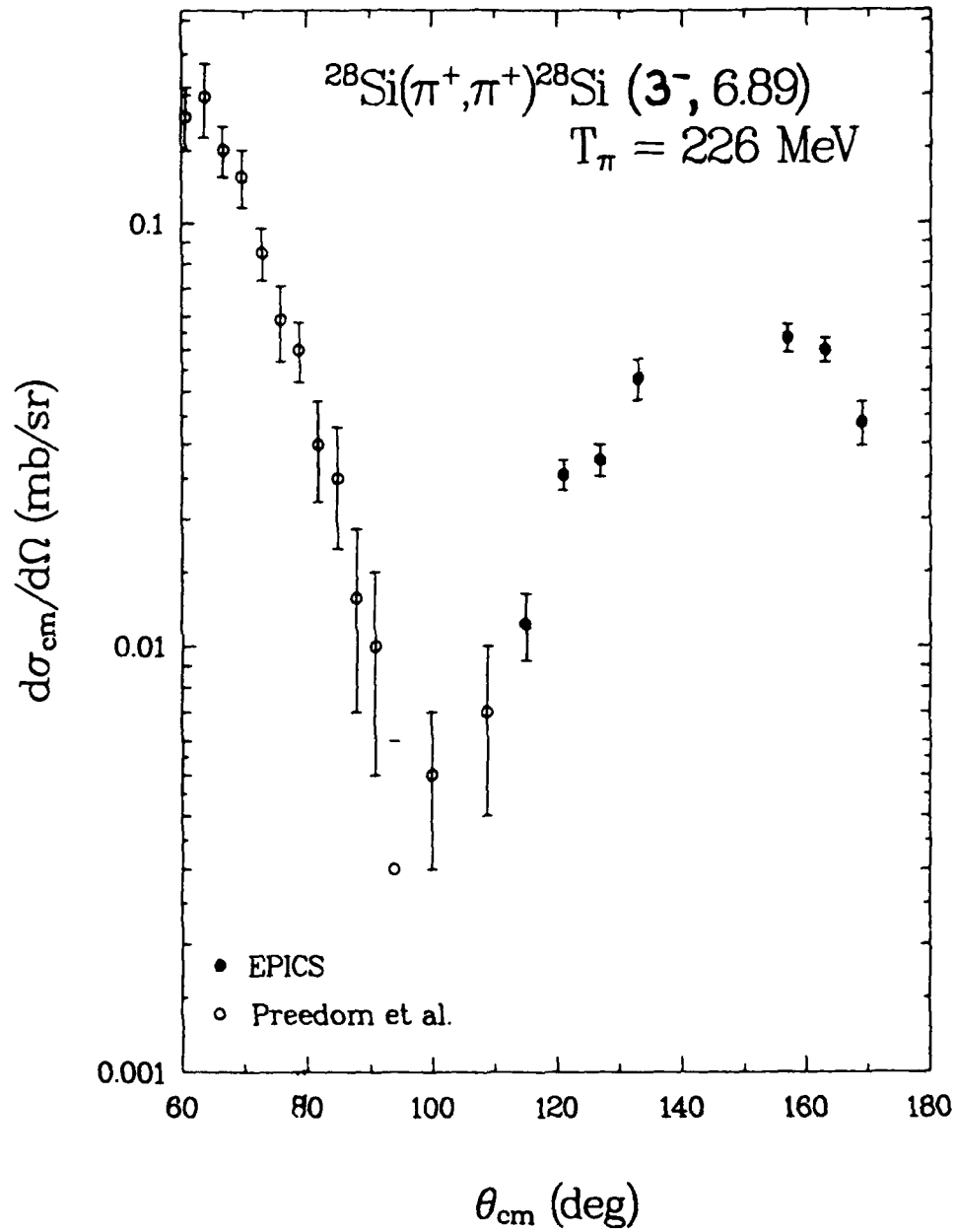


Figure 39: Angular distribution of the differential cross sections for  $\pi^+$  inelastic scattering to the  $3^-$ , 6.88 MeV level of  $^{28}\text{Si}$  at the energy  $T_\pi = 226 \text{ MeV}$ .

## 4 Summary

Using the EPICS system at the Clinton P. Anderson Meson Physics Facility,  $\pi^+$  and  $\pi^-$  elastic scattering differential cross sections have been obtained for  $^{40}\text{Ca}$  and  $^{28}\text{Si}$ . Differential cross sections have also been obtained for  $\pi^+$  inelastic scattering to the first three excited states of  $^{28}\text{Si}$  ( $2^+$ , 1.78 MeV,  $4^+$ , 4.62 MeV, and  $3^-$ , 6.88 MeV). Angular distributions of these cross section measurements were taken at large angles,  $115^\circ \leq \theta_{cm} \leq 175^\circ$ , and then compared to similar data taken at forward scattering angles. The elastic scattering displayed a good match between the two data sets at three different energies spanning the  $\Delta(1232)$  resonance region, thus providing a continuous spectrum over this energy range. The comparisons for the excited states, however, didn't fare quite as well. This was due partly to a lack of sufficient data points at incident pion energies both at the low and the high range.

Energy distributions of the above cross sections were also compiled at a scattering angle of  $175^\circ$ . These were typically found to be as expected, that is, with the exception of some small amount of spectral structure, an exponentially decreasing cross section with increasing energy. As discussed in the Introduction, theoretical predictions for pion scattering at very large angles is difficult, and current modeling is not sufficient to explain the data measured to date. Using what seems to be the most promising model, that being the delta-hole approach, in conjunction with the data presented here, as well as the results from any future large angle experiments, large angle scattering mechanisms may begin to become apparent. This will ultimately

lead to a better understanding of the entire scattering process and the development of more appropriate theoretical models for all types of nuclear scattering processes.

## 5 Appendix

This appendix consists of tabulated values of measured and calculated parameters used in the calculation of the differential cross sections. Table 4 is the tabulated data for the acceptance scan run. Table 5 contains tabulated values for the hydrogen normalization runs. Finally, Tables 6-16 contain the differential cross sections displayed in graphical form in the text.

Acceptance Scan

Target: 12C  
 $\Theta$  (lab): 120.0°  
 $\Theta$  (cm): 121.3°  
 $T\pi$  (MeV): 162.0 (+)

Delta	Norm3	Peak Area	Yield	Norm. Yield
-5.98%	7.08E-05	1.16E+03 +/- 3.45E+01	8.19E-02 +/- 2.44E-03	4.24E-01 +/- 1.26E-02
-4.01%	1.13E-04	1.11E+03 +/- 3.40E+01	1.26E-01 +/- 3.84E-03	6.51E-01 +/- 1.99E-02
-2.01%	1.49E-04	9.79E+02 +/- 3.21E+01	1.46E-01 +/- 4.78E-03	7.55E-01 +/- 2.48E-02
0.00%	1.76E-04	9.60E+02 +/- 3.18E+01	1.69E-01 +/- 5.60E-03	8.77E-01 +/- 2.90E-02
1.99%	1.92E-04	1.00E+03 +/- 3.25E+01	1.93E-01 +/- 6.25E-03	1.00E+00 +/- 3.24E-02
3.99%	1.41E-04	1.29E+03 +/- 3.67E+01	1.81E-01 +/- 5.17E-03	9.40E-01 +/- 2.68E-02
5.99%	1.70E-04	9.98E+02 +/- 3.24E+01	1.70E-01 +/- 5.50E-03	8.79E-01 +/- 2.85E-02

Table 4: Tabular values of the measured and calculated parameters used to determine the acceptance curve.

Θ lab = 120 deg

T (+/-)	Norm3	Peak Area	Yield	σ(H,lab)	α <sub>lab</sub> (H)
220 -	1.54E-04	1.10E+03 +/- 3.75E+01	1.70E-01 +/- 5.79E-03	1.06E+00	6.23E+00 +/- 2.12E-01
200 -	1.63E-04	1.16E+03 +/- 3.83E+01	1.88E-01 +/- 6.22E-03	1.23E+00	6.56E+00 +/- 2.17E-01
180 -	1.88E-04	1.10E+03 +/- 3.71E+01	2.08E-01 +/- 6.98E-03	1.28E+00	6.15E+00 +/- 2.07E-01
160 -	9.86E-05	1.50E+03 +/- 4.48E+01	1.48E-01 +/- 4.42E-03	1.10E+00	7.39E+00 +/- 2.20E-01
150 -	7.73E-05	1.37E+03 +/- 4.39E+01	1.06E-01 +/- 3.39E-03	9.31E-01	8.79E+00 +/- 2.81E-01
140 -	7.59E-05	1.16E+03 +/- 4.20E+01	8.82E-02 +/- 3.19E-03	7.48E-01	8.48E+00 +/- 3.06E-01
127 -	5.04E-05	1.16E+03 +/- 4.47E+01	5.82E-02 +/- 2.25E-03	5.22E-01	8.96E+00 +/- 3.47E-01
120 -	4.85E-04	7.70E+01 +/- 1.09E+01	3.73E-02 +/- 5.28E-03	4.17E-01	1.12E+01 +/- 1.58E+00
110 -	2.64E-05	9.09E+02 +/- 4.19E+01	2.40E-02 +/- 1.11E-03	2.92E-01	1.22E+01 +/- 5.61E-01
100 -	3.01E-05	3.86E+02 +/- 2.83E+01	1.16E-02 +/- 8.52E-04	1.99E-01	1.71E+01 +/- 1.25E+00

Θ lab = 130 deg

260 +	8.70E-04	4.91E+03 +/- 7.47E+01	4.27E+00 +/- 6.50E-02	4.55E+00	1.07E+00 +/- 1.62E-02
240 +	5.85E-04	1.05E+04 +/- 1.08E+02	6.12E+00 +/- 6.32E-02	6.40E+00	1.05E+00 +/- 1.08E-02
220 +	7.34E-04	1.12E+04 +/- 1.11E+02	8.25E+00 +/- 8.16E-02	8.93E+00	1.08E+00 +/- 1.07E-02
200 +	1.27E-03	7.93E+03 +/- 9.30E+01	1.00E+01 +/- 1.18E-01	1.20E+01	1.19E+00 +/- 1.40E-02
180 +	8.65E-04	1.25E+04 +/- 1.16E+02	1.08E+01 +/- 1.00E-01	1.46E+01	1.35E+00 +/- 1.26E-02
160 +	7.76E-04	1.26E+04 +/- 1.16E+02	9.78E+00 +/- 9.00E-02	1.50E+01	1.54E+00 +/- 1.41E-02
140 +	1.61E-03	4.08E+03 +/- 6.57E+01	6.55E+00 +/- 1.06E-01	1.28E+01	1.95E+00 +/- 3.15E-02
125 +	9.47E-04	3.84E+03 +/- 6.38E+01	3.63E+00 +/- 6.04E-02	1.02E+01	2.81E+00 +/- 4.67E-02
120 +	8.12E-04	3.99E+03 +/- 6.54E+01	3.24E+00 +/- 5.31E-02	9.31E+00	2.87E+00 +/- 4.70E-02
110 +	5.47E-04	3.81E+03 +/- 6.37E+01	2.08E+00 +/- 3.48E-02	7.62E+00	3.66E+00 +/- 6.12E-02
100 +	3.14E-04	4.28E+03 +/- 6.77E+01	1.34E+00 +/- 2.12E-02	6.11E+00	4.56E+00 +/- 7.22E-02

Θ lab = 150 deg

260 +	8.57E-04	6.31E+03 +/- 9.45E+01	5.40E+00 +/- 8.10E-02	5.22E+00	9.66E-01 +/- 1.45E-02
240 +	3.91E-03	1.88E+03 +/- 4.79E+01	7.34E+00 +/- 1.87E-01	7.28E+00	9.92E-01 +/- 2.53E-02
220 +	2.19E-03	4.18E+03 +/- 7.21E+01	9.16E+00 +/- 1.58E-01	1.01E+01	1.10E+00 +/- 1.90E-02
200 +	1.46E-03	8.07E+03 +/- 9.85E+01	1.18E+01 +/- 1.44E-01	1.34E+01	1.14E+00 +/- 1.40E-02
180 +	2.50E-03	4.60E+03 +/- 7.25E+01	1.15E+01 +/- 1.81E-01	1.63E+01	1.42E+00 +/- 2.24E-02
160 +	1.60E-03	6.99E+03 +/- 9.23E+01	1.12E+01 +/- 1.48E-01	1.68E+01	1.50E+00 +/- 1.98E-02
140 +	1.80E-03	4.21E+03 +/- 6.94E+01	7.55E+00 +/- 1.25E-01	1.43E+01	1.89E+00 +/- 3.12E-02
100 +	5.55E-04	4.05E+03 +/- 8.66E+01	2.25E+00 +/- 4.81E-02	6.80E+00	3.03E+00 +/- 6.47E-02

Table 5: Tabular values of the measured and calculated parameters used to determine the hydrogen normalization curves.

		Target: Ca-40	$\Theta$ (lab): 175.00 deg	Target Ratio: 1.607			
		Ex. State: 0.00 MeV	$\Theta$ (cm): 175.05 deg				
T (+/-)	Norm3	Peak Area	$\alpha(H)$	$\xi$	N( $\xi$ )	Jac	$d\sigma_{cm}/d\Omega$
260 +	1.53E-05	2.80E+01 +/- 9.50E+00	1.30E+00	2.00	0.95	1.02	9.66E-04 +/- 3.28E-04
240 +	1.36E-05	7.70E+01 +/- 1.15E+01	9.96E-01	2.00	0.95	1.02	1.80E-03 +/- 2.69E-04
220 +	1.52E-05	2.42E+02 +/- 1.69E+01	8.81E-01	2.00	0.95	1.02	5.61E-03 +/- 3.91E-04
200 +	4.28E-05	2.67E+02 +/- 1.78E+01	9.56E-01	2.00	0.95	1.02	1.88E-02 +/- 1.26E-03
180 +	1.93E-04	9.60E+01 +/- 1.11E+01	1.22E+00	2.01	0.95	1.02	3.89E-02 +/- 4.50E-03
170 +	3.57E-05	3.45E+02 +/- 2.50E+01	1.42E+00	2.00	0.95	1.02	3.02E-02 +/- 2.19E-03
160 +	1.02E-04	2.36E+02 +/- 1.66E+01	1.67E+00	1.99	0.95	1.02	6.94E-02 +/- 4.88E-03
150 +	1.23E-04	3.25E+02 +/- 1.90E+01	1.97E+00	2.00	0.95	1.02	1.36E-01 +/- 7.95E-03
140 +	2.29E-04	3.77E+02 +/- 2.05E+01	2.32E+00	2.00	0.95	1.02	3.45E-01 +/- 1.87E-02
137 +	1.45E-04	6.43E+02 +/- 2.65E+01	2.43E+00	2.00	0.95	1.01	3.91E-01 +/- 1.61E-02
127 +	1.27E-04	5.57E+02 +/- 2.47E+01	2.84E+00	2.00	0.95	1.01	3.45E-01 +/- 1.53E-02
120 +	8.04E-05	4.79E+02 +/- 2.30E+01	3.15E+00	2.00	0.95	1.01	2.09E-01 +/- 1.00E-02
110 +	1.45E-04	3.78E+02 +/- 2.05E+01	3.64E+00	2.00	0.95	1.01	3.42E-01 +/- 1.85E-02
100 +	1.80E-04	8.65E+02 +/- 3.04E+01	4.18E+00	2.00	0.95	1.01	1.11E+00 +/- 3.92E-02
220 -	8.15E-06	2.60E+01 +/- 7.30E+00	5.51E+00	1.98	0.95	1.02	2.02E-03 +/- 5.66E-04
200 -	1.36E-05	7.40E+01 +/- 9.70E+00	5.75E+00	2.01	0.95	1.02	9.97E-03 +/- 1.31E-03
180 -	1.71E-05	1.55E+02 +/- 1.36E+01	6.54E+00	2.00	0.95	1.02	2.99E-02 +/- 2.62E-03
160 -	1.17E-05	2.97E+02 +/- 1.85E+01	7.87E+00	1.99	0.95	1.02	4.71E-02 +/- 2.93E-03
150 -	1.98E-05	1.12E+02 +/- 1.18E+01	8.73E+00	2.00	0.95	1.02	3.34E-02 +/- 3.52E-03
140 -	2.57E-05	3.45E+02 +/- 1.97E+01	9.73E+00	1.99	0.95	1.02	1.48E-01 +/- 8.46E-03
127 -	5.24E-05	2.96E+02 +/- 1.82E+01	1.12E+01	1.99	0.95	1.01	3.00E-01 +/- 1.84E-02
120 -	4.03E-05	5.06E+02 +/- 2.35E+01	1.21E+01	2.00	0.95	1.01	4.25E-01 +/- 1.97E-02
110 -	2.29E-05	2.21E+02 +/- 1.59E+01	1.35E+01	2.02	0.95	1.01	1.18E-01 +/- 8.46E-03
100 -	2.88E-05	3.91E+02 +/- 2.10E+01	1.51E+01	2.00	0.95	1.01	2.91E-01 +/- 1.56E-02

Table 6: Tabular values of the measured and calculated parameters used to determine an energy distribution of the differential cross sections for  $\pi^+$  and  $\pi^-$  elastic scattering from  $^{40}\text{Ca}$ .



		Target: Si-28	$\Theta$ (lab): 175.00 deg	Target Ratio: 3.87			
		Ex. State: 0.0 MeV	$\Theta$ (cm): 175.05 deg				
T (+/-)	Norm3	Peak Area	$\alpha(H)$	$\delta$	N ( $\delta$ )	Jac	$d\sigma_{cm}/d\Omega$
240 +	7.58E-06	3.20E+01 +/- 7.90E+00	9.96E-01	2.00	0.95	1.03	1.01E-03 +/- 2.50E-04
220 +	1.09E-05	7.60E+01 +/- 1.17E+01	8.81E-01	1.99	0.95	1.03	3.05E-03 +/- 4.70E-04
200 +	1.20E-05	1.79E+02 +/- 1.70E+01	9.56E-01	2.01	0.95	1.03	8.61E-03 +/- 8.18E-04
180 +	2.35E-05	3.52E+02 +/- 2.12E+01	1.22E+00	1.99	0.95	1.02	4.23E-02 +/- 2.55E-03
160 +	4.28E-05	3.30E+02 +/- 1.98E+01	1.67E+00	2.00	0.95	1.02	9.87E-02 +/- 5.92E-03
150 +	4.65E-05	2.67E+02 +/- 1.81E+01	1.97E+00	2.00	0.95	1.02	1.02E-01 +/- 6.93E-03
140 +	1.82E-05	4.80E+02 +/- 2.39E+01	2.32E+00	2.00	0.95	1.02	8.46E-02 +/- 4.21E-03
130 +	7.30E-05	2.94E+02 +/- 1.83E+01	2.71E+00	1.99	0.95	1.02	2.43E-01 +/- 1.51E-02
125 +	7.57E-05	4.18E+02 +/- 2.14E+01	2.93E+00	2.00	0.95	1.02	3.86E-01 +/- 1.97E-02
120 +	7.73E-05	6.10E+02 +/- 2.56E+01	3.15E+00	2.00	0.95	1.02	6.18E-01 +/- 2.60E-02
110 +	1.62E-04	3.21E+02 +/- 1.86E+01	3.64E+00	2.00	0.95	1.02	7.89E-01 +/- 4.57E-02
100 +	7.26E-05	5.35E+02 +/- 2.39E+01	4.18E+00	2.00	0.95	1.02	6.74E-01 +/- 3.01E-02
150 -	1.88E-05	1.68E+02 +/- 1.37E+01	8.73E+00	2.00	0.95	1.02	1.15E-01 +/- 9.38E-03
140 -	1.91E-05	8.10E+01 +/- 9.80E+00	9.73E+00	2.00	0.95	1.02	6.27E-02 +/- 7.59E-03
127 -	2.47E-05	8.70E+01 +/- 1.06E+01	1.12E+01	2.01	0.95	1.02	1.00E-01 +/- 1.22E-02
110 -	5.66E-05	2.74E+02 +/- 1.71E+01	1.35E+01	1.99	0.95	1.02	8.73E-01 +/- 5.45E-02

Table 7: Tabular values of the measured and calculated parameters used to determine an energy distribution of the differential cross sections for  $\pi^+$  and  $\pi^-$  elastic scattering from  $^{28}\text{Si}$ .

		Target: Si-28	$\Theta$ (lab): 175.00 deg	Target Ratio: 3.87			
		Ex. State: 4.62 MeV	$\Theta$ (cm): 175.05 deg				
T (+/-)	Norm3	Peak Area	$\alpha$ (H)	$\delta$	N ( $\delta$ )	Jac	$d\sigma_{cm}/d\Omega$
240 +	7.68E-06	1.75E+02 +/- 1.45E+01	9.96E-01	0.55	0.92	1.03	5.82E-03 +/- 4.82E-04
220 +	1.10E-05	2.20E+02 +/- 1.69E+01	8.81E-01	0.44	0.91	1.03	9.32E-03 +/- 7.16E-04
200 +	1.22E-05	3.88E+02 +/- 2.15E+01	9.56E-01	0.32	0.91	1.03	1.98E-02 +/- 1.10E-03
180 +	2.40E-05	2.91E+02 +/- 1.81E+01	1.22E+00	0.16	0.90	1.02	3.74E-02 +/- 2.33E-03
160 +	4.39E-05	2.02E+02 +/- 1.52E+01	1.67E+00	-0.02	0.90	1.02	6.55E-02 +/- 4.93E-03
150 +	4.78E-05	1.82E+02 +/- 1.44E+01	1.97E+00	-0.14	0.89	1.02	7.62E-02 +/- 6.03E-03
140 +	1.88E-05	4.82E+02 +/- 2.28E+01	2.32E+00	-0.26	0.89	1.02	9.37E-02 +/- 4.43E-03
130 +	7.56E-05	2.16E+02 +/- 1.53E+01	2.71E+00	-0.42	0.88	1.02	1.99E-01 +/- 1.41E-02
125 +	7.85E-05	1.47E+02 +/- 1.27E+01	2.93E+00	-0.50	0.88	1.02	1.52E-01 +/- 1.32E-02
120 +	8.03E-05	1.64E+02 +/- 1.35E+01	3.15E+00	-0.59	0.87	1.02	1.88E-01 +/- 1.55E-02
110 +	1.70E-04	5.40E+01 +/- 8.10E+00	3.64E+00	-0.79	0.86	1.02	1.53E-01 +/- 2.29E-02
100 +	7.64E-05	1.72E+02 +/- 1.37E+01	4.18E+00	-1.02	0.85	1.02	2.54E-01 +/- 2.03E-02
150 -	1.93E-05	7.20E+01 +/- 9.60E+00	8.73E+00	-0.14	0.89	1.02	5.39E-02 +/- 7.18E-03
140 -	1.97E-05	7.50E+01 +/- 9.10E+00	9.73E+00	-0.27	0.89	1.02	6.41E-02 +/- 7.77E-03
127 -	2.56E-05	7.10E+01 +/- 9.40E+00	1.12E+01	-0.46	0.88	1.02	9.17E-02 +/- 1.21E-02
110 -	5.91E-05	6.10E+01 +/- 8.70E+00	1.35E+01	-0.79	0.86	1.02	2.23E-01 +/- 3.18E-02

Table 9: Tabular values of the measured and calculated parameters used to determine an energy distribution of the differential cross sections for  $\pi^+$  and  $\pi^-$  inelastic scattering to the  $4^+$ , 4.62 MeV state of  $^{28}\text{Si}$ .

		Target: Si-28	$\Theta$ (lab): 175.00 deg	Target Ratio: 3.87			
		Ex. State: 6.88 MeV	$\Theta$ (cm): 175.05 deg				
T (+/-)	Norm3	Peak Area	$\alpha$ (H)	$\delta$	N( $\delta$ )	Jac	$d\sigma_{cm}/d\Omega$
240 +	7.74E-06	1.84E+02 +/- 1.45E+01	9.96E-01	-0.16	0.89	1.03	6.34E-03 +/- 4.99E-04
220 +	1.11E-05	4.30E+02 +/- 2.16E+01	8.81E-01	-0.33	0.88	1.03	1.90E-02 +/- 9.53E-04
200 +	1.24E-05	5.72E+02 +/- 2.50E+01	9.56E-01	-0.51	0.88	1.03	3.06E-02 +/- 1.34E-03
180 +	2.43E-05	4.83E+02 +/- 2.27E+01	1.22E+00	-0.75	0.86	1.02	6.57E-02 +/- 3.09E-03
160 +	4.44E-05	3.69E+02 +/- 1.99E+01	1.67E+00	-1.02	0.85	1.02	1.28E-01 +/- 6.89E-03
150 +	4.85E-05	3.80E+02 +/- 2.01E+01	1.97E+00	-1.20	0.84	1.02	1.71E-01 +/- 9.05E-03
140 +	1.91E-05	1.13E+03 +/- 3.41E+01	2.32E+00	-1.38	0.83	1.02	2.38E-01 +/- 7.19E-03
130 +	7.69E-05	2.54E+02 +/- 1.65E+01	2.71E+00	-1.61	0.82	1.02	2.56E-01 +/- 1.67E-02
125 +	8.00E-05	2.85E+02 +/- 1.73E+01	2.93E+00	-1.73	0.81	1.02	3.25E-01 +/- 1.98E-02
120 +	8.19E-05	3.22E+02 +/- 1.85E+01	3.15E+00	-1.86	0.80	1.02	4.10E-01 +/- 2.35E-02
110 +	1.74E-04	1.82E+02 +/- 1.39E+01	3.64E+00	-2.16	0.78	1.02	5.81E-01 +/- 4.43E-02
100 +	7.85E-05	5.26E+02 +/- 2.33E+01	4.18E+00	-2.51	0.76	1.02	8.98E-01 +/- 3.98E-02
150 -	1.96E-05	2.20E+02 +/- 1.61E+01	8.73E+00	-1.19	0.84	1.02	1.77E-01 +/- 1.30E-02
140 -	2.00E-05	1.65E+02 +/- 1.32E+01	9.73E+00	-1.39	0.83	1.02	1.53E-01 +/- 1.22E-02
127 -	2.60E-05	1.62E+02 +/- 1.33E+01	1.12E+01	-1.67	0.81	1.02	2.30E-01 +/- 1.89E-02
110 -	6.05E-05	9.40E+01 +/- 1.03E+01	1.35E+01	-2.17	0.78	1.02	3.89E-01 +/- 4.26E-02

Table 10: Tabular values of the measured and calculated parameters used to determine an energy distribution of the differential cross sections for  $\pi^+$  and  $\pi^-$  inelastic scattering to the  $3^-$ , 6.88 MeV state of  $^{28}\text{Si}$ .

		Target: Si-28	T (+/-): 130 +	Target Ratio: 3.87	
		Ex. State: 0.00 MeV	$\alpha$ (H): 2.712		
$\Theta$ (cm)	Norm3	Peak Area	$\delta$	N ( $\delta$ ) Jac	$d\sigma_{cm}/d\Omega$
115.53	3.49E-05	3.72E+02 +/- 2.09E+01	2.00	0.95 1.01	1.45E-01 +/- 8.15E-03
121.50	3.55E-05	1.46E+02 +/- 1.41E+01	2.00	0.95 1.01	5.80E-02 +/- 5.60E-03
124.49	4.21E-05	1.30E+02 +/- 1.31E+01	2.00	0.95 1.01	6.12E-02 +/- 6.17E-03
127.47	5.01E-05	1.47E+02 +/- 1.38E+01	2.00	0.95 1.01	8.26E-02 +/- 7.75E-03
133.43	1.26E-04	1.78E+02 +/- 1.46E+01	1.99	0.95 1.01	2.52E-01 +/- 2.06E-02
139.38	4.59E-05	6.00E+02 +/- 2.57E+01	2.00	0.95 1.02	3.09E-01 +/- 1.32E-02
145.34	5.33E-05	6.75E+02 +/- 2.72E+01	2.00	0.95 1.02	4.05E-01 +/- 1.63E-02
151.28	5.84E-05	6.21E+02 +/- 2.62E+01	2.00	0.95 1.02	4.08E-01 +/- 1.72E-02
157.23	5.45E-05	5.81E+02 +/- 2.58E+01	2.00	0.95 1.02	3.57E-01 +/- 1.59E-02
163.17	4.82E-05	6.39E+02 +/- 2.64E+01	1.99	0.95 1.02	3.48E-01 +/- 1.44E-02
169.11	4.45E-05	5.37E+02 +/- 2.46E+01	2.00	0.95 1.02	2.70E-01 +/- 1.24E-02
175.05	7.30E-05	2.94E+02 +/- 1.83E+01	1.99	0.95 1.02	2.43E-01 +/- 1.51E-02

		Target: Si-28	T (+/-): 130 +	Target Ratio: 3.87	
		Ex. State: 1.78 MeV	$\alpha$ (H): 2.712		
$\Theta$ (cm)	Norm3	Peak Area	$\delta$	N ( $\delta$ ) Jac	$d\sigma_{cm}/d\Omega$
115.53	3.54E-05	9.12E+02 +/- 3.11E+01	1.08	0.93 1.01	3.67E-01 +/- 1.25E-02
121.50	3.60E-05	1.00E+03 +/- 3.25E+01	1.07	0.93 1.01	4.10E-01 +/- 1.33E-02
124.49	4.26E-05	8.32E+02 +/- 2.96E+01	1.07	0.93 1.01	4.04E-01 +/- 1.44E-02
127.47	5.08E-05	6.48E+02 +/- 2.63E+01	1.07	0.93 1.01	3.75E-01 +/- 1.52E-02
133.43	1.28E-04	2.36E+02 +/- 1.64E+01	1.06	0.93 1.01	3.44E-01 +/- 2.39E-02
139.38	4.65E-05	6.07E+02 +/- 2.59E+01	1.07	0.93 1.02	3.23E-01 +/- 1.38E-02
145.34	5.40E-05	4.16E+02 +/- 2.15E+01	1.07	0.93 1.02	2.57E-01 +/- 1.33E-02
151.28	5.91E-05	4.03E+02 +/- 2.14E+01	1.07	0.93 1.02	2.73E-01 +/- 1.45E-02
157.23	5.53E-05	5.19E+02 +/- 2.41E+01	1.07	0.93 1.02	3.29E-01 +/- 1.53E-02
163.17	4.89E-05	6.56E+02 +/- 2.65E+01	1.07	0.93 1.02	3.68E-01 +/- 1.49E-02
169.11	4.51E-05	7.29E+02 +/- 2.81E+01	1.07	0.93 1.02	3.78E-01 +/- 1.46E-02
175.05	7.40E-05	4.50E+02 +/- 2.20E+01	1.07	0.93 1.02	3.83E-01 +/- 1.87E-02

Table 11: Tabular values of the measured and calculated parameters used to determine an angular distribution of the differential cross sections for  $\pi^+$  elastic scattering and inelastic scattering to the  $2^+$ , 1.78 MeV state of  $^{28}\text{Si}$  at  $T_\pi=130$  MeV.

		Target: Si-28	T (+/-): 180 +	Target Ratio: 3.87		
		Ex. State: 0.00 MeV	$\alpha(H)$ : 1.22			
$\Theta$ (cm)	Norm3	Peak Area	$\delta$	N ( $\delta$ )	Jac	$d\sigma_{cm}/d\Omega$
115.63	2.26E-05	3.49E+02 +/- 2.03E+01	2.00	0.95	1.01	8.81E-02 +/- 5.12E-03
121.59	2.12E-05	3.76E+02 +/- 2.11E+01	2.00	0.95	1.01	8.93E-02 +/- 5.01E-03
127.55	1.61E-05	4.15E+02 +/- 2.20E+01	1.99	0.95	1.01	7.49E-02 +/- 3.97E-03
133.51	2.83E-05	1.90E+02 +/- 1.66E+01	2.00	0.95	1.02	6.05E-02 +/- 5.29E-03
139.45	1.90E-05	1.85E+02 +/- 1.51E+01	2.00	0.95	1.02	3.96E-02 +/- 3.23E-03
145.40	2.56E-05	1.96E+02 +/- 1.69E+01	2.00	0.95	1.02	5.66E-02 +/- 4.88E-03
151.34	4.69E-05	1.50E+02 +/- 1.40E+01	1.99	0.95	1.02	7.95E-02 +/- 7.42E-03
157.27	3.83E-05	1.71E+02 +/- 1.59E+01	1.99	0.95	1.02	7.41E-02 +/- 6.89E-03
163.20	3.55E-05	1.74E+02 +/- 1.54E+01	2.00	0.95	1.02	7.00E-02 +/- 6.19E-03
169.13	3.02E-05	2.78E+02 +/- 1.90E+01	1.99	0.95	1.02	9.50E-02 +/- 6.50E-03
175.06	2.35E-05	3.52E+02 +/- 2.12E+01	1.99	0.95	1.02	9.40E-02 +/- 5.66E-03

		Target: Si-28	T (+/-): 180 +	Target Ratio: 3.87		
		Ex. State: 1.78 MeV	$\alpha(H)$ : 1.22			
$\Theta$ (cm)	Norm3	Peak Area	$\delta$	N ( $\delta$ )	Jac	$d\sigma_{cm}/d\Omega$
115.63	2.28E-05	2.51E+02 +/- 1.81E+01	1.29	0.94	1.01	6.47E-02 +/- 4.66E-03
121.59	2.14E-05	3.91E+02 +/- 2.18E+01	1.29	0.94	1.01	9.47E-02 +/- 5.28E-03
127.55	1.62E-05	7.65E+02 +/- 2.91E+01	1.29	0.94	1.01	1.41E-01 +/- 5.36E-03
133.51	2.85E-05	4.68E+02 +/- 2.35E+01	1.29	0.94	1.02	1.52E-01 +/- 7.64E-03
139.45	1.91E-05	7.96E+02 +/- 2.93E+01	1.30	0.94	1.02	1.74E-01 +/- 6.40E-03
145.40	2.58E-05	5.06E+02 +/- 2.43E+01	1.29	0.94	1.02	1.49E-01 +/- 7.16E-03
151.34	4.73E-05	2.84E+02 +/- 1.82E+01	1.29	0.94	1.02	1.54E-01 +/- 9.85E-03
157.27	3.86E-05	3.30E+02 +/- 2.02E+01	1.29	0.94	1.02	1.46E-01 +/- 8.93E-03
163.20	3.58E-05	3.89E+02 +/- 2.17E+01	1.29	0.94	1.02	1.60E-01 +/- 8.91E-03
169.13	3.04E-05	4.11E+02 +/- 2.22E+01	1.29	0.94	1.02	1.43E-01 +/- 7.75E-03
175.06	2.37E-05	5.71E+02 +/- 2.56E+01	1.28	0.94	1.02	1.56E-01 +/- 6.97E-03

Table 13: Tabular values of the measured and calculated parameters used to determine an angular distribution of the differential cross sections for  $\pi^+$  elastic scattering and inelastic scattering to the  $2^+$ , 1.78 MeV state of  $^{28}\text{Si}$  at  $T_\pi=180$  MeV.

		Target: Si-28	T (+/-): 226 +	Target Ratio: 3.87	
		Ex. State: 0.00 MeV	$\alpha(H)$ : 0.895		
$\Theta$ (cm)	Norm3	Peak Area	$\delta$	N( $\delta$ ) Jac	$d\sigma_{cm}/d\Omega$
115.72	2.21E-05	4.00E+00 +/- 4.00E+00	2.00	0.95 1.01	9.88E-04 +/- 9.88E-04
121.68	1.19E-05	1.30E+01 +/- 6.40E+00	2.00	0.95 1.01	1.73E-03 +/- 8.51E-04
127.63	1.46E-05	3.50E+01 +/- 7.90E+00	1.94	0.95 1.02	5.76E-03 +/- 1.30E-03
133.58	3.66E-05	2.20E+01 +/- 6.50E+00	2.00	0.95 1.02	9.09E-03 +/- 2.69E-03
157.31	2.08E-05	4.50E+01 +/- 9.00E+00	2.00	0.95 1.03	1.06E-02 +/- 2.12E-03
163.23	1.55E-05	3.30E+01 +/- 8.17E+00	2.00	0.95 1.03	5.82E-03 +/- 1.44E-03
169.15	3.19E-05	1.80E+01 +/- 5.70E+00	2.00	0.95 1.03	6.52E-03 +/- 2.07E-03

		Target: Si-28	T (+/-): 226 +	Target Ratio: 3.87	
		Ex. State: 1.78 MeV	$\alpha(H)$ : 0.895		
$\Theta$ (cm)	Norm3	Peak Area	$\delta$	N( $\delta$ ) Jac	$d\sigma_{cm}/d\Omega$
115.72	2.22E-05	4.60E+01 +/- 7.60E+00	1.41	0.94 1.01	1.15E-02 +/- 1.91E-03
121.68	1.19E-05	1.40E+02 +/- 1.30E+01	1.41	0.94 1.01	1.89E-02 +/- 1.76E-03
127.63	1.47E-05	1.38E+02 +/- 1.31E+01	1.35	0.94 1.02	2.31E-02 +/- 2.19E-03
133.58	3.69E-05	5.80E+01 +/- 8.60E+00	1.42	0.94 1.02	2.43E-02 +/- 3.61E-03
157.31	2.09E-05	1.67E+02 +/- 1.44E+01	1.41	0.94 1.03	3.99E-02 +/- 3.44E-03
163.23	1.56E-05	2.70E+02 +/- 1.76E+01	1.41	0.94 1.03	4.83E-02 +/- 3.15E-03
169.15	3.20E-05	1.20E+02 +/- 1.20E+01	1.42	0.94 1.03	4.42E-02 +/- 4.42E-03

Table 15: Tabular values of the measured and calculated parameters used to determine an angular distribution of the differential cross sections for  $\pi^+$  elastic scattering and inelastic scattering to the  $2^+$ , 1.78 MeV state of  $^{28}\text{Si}$  at  $T_\pi=226$  MeV.

		Target: Si-28	T (+/-): 226 +	Target Ratio: 3.87	
		Ex. State: 4.62 MeV	$\alpha(H)$ : 0.895		
$\Theta$ (cm)	Norm3	Peak Area	$\delta$	N ( $\delta$ ) Jac	$d\sigma_{cm}/d\Omega$
115.72	2.24E-05	1.70E+01 +/- 5.30E+00	0.48	0.91 1.01	4.42E-03 +/- 1.38E-03
121.68	1.20E-05	5.60E+01 +/- 9.90E+00	0.48	0.91 1.01	7.84E-03 +/- 1.39E-03
127.63	1.48E-05	6.80E+01 +/- 9.40E+00	0.42	0.91 1.02	1.18E-02 +/- 1.63E-03
133.58	3.72E-05	5.30E+01 +/- 8.30E+00	0.49	0.91 1.02	2.30E-02 +/- 3.61E-03
157.31	2.11E-05	1.07E+02 +/- 1.17E+01	0.48	0.91 1.03	2.65E-02 +/- 2.90E-03
163.23	1.57E-05	1.39E+02 +/- 1.32E+01	0.48	0.91 1.03	2.58E-02 +/- 2.45E-03
169.15	3.23E-05	6.20E+01 +/- 8.90E+00	0.48	0.91 1.03	2.36E-02 +/- 3.39E-03

		Target: Si-28	T (+/-): 226 +	Target Ratio: 3.87	
		Ex. State: 6.88 MeV	$\alpha(H)$ : 0.895		
$\Theta$ (cm)	Norm3	Peak Area	$\delta$	N ( $\delta$ ) Jac	$d\sigma_{cm}/d\Omega$
115.72	2.26E-05	4.20E+01 +/- 7.50E+00	-0.27	0.89 1.01	1.13E-02 +/- 2.03E-03
121.68	1.21E-05	1.75E+02 +/- 1.44E+01	-0.27	0.89 1.01	2.55E-02 +/- 2.09E-03
127.63	1.50E-05	1.53E+02 +/- 1.30E+01	-0.33	0.88 1.02	2.76E-02 +/- 2.35E-03
133.58	3.75E-05	9.50E+01 +/- 1.05E+01	-0.26	0.89 1.02	4.29E-02 +/- 4.75E-03
157.31	2.12E-05	2.07E+02 +/- 1.52E+01	-0.27	0.89 1.03	5.33E-02 +/- 3.92E-03
163.23	1.59E-05	2.59E+02 +/- 1.68E+01	-0.27	0.89 1.03	5.00E-02 +/- 3.24E-03
169.15	3.26E-05	8.50E+01 +/- 1.00E+01	-0.27	0.89 1.03	3.37E-02 +/- 3.96E-03

Table 16: Tabular values of the measured and calculated parameters used to determine an angular distribution of the differential cross sections for  $\pi^+$  inelastic scattering to the  $4^+$ , 4.62 MeV and  $3^-$ , 6.88 MeV states of  $^{28}\text{Si}$  at  $T_\pi=226$  MeV.

## 6 References

- [Al-77] J. C. Allred, Los Alamos Scientific Laboratory Report LA-6878-MS, (1977).
- [Al-80] J. P. Albanese *et al.*, *Nuc. Phys.*, **A350**, 301 (1980).
- [Am-79] J. F. Amann *et al.*, *IEEE Trans. Nucl. Sci.*, **NS-26**, 4389 (1979).
- [At-81] L. G. Atencio *et al.*, *Nuc. Instr. Meth.*, **187**, 361 (1981).
- [Ba-68] P. Bareyre, C. Bricman, and G. Villet, *Phys. Rev.*, **165**, 1730 (1968).
- [Ba-82] E. Bason *et al.*, *Phys. Lett.*, **118B**, 319 (1982).
- [Bo-84] K. G. Boyer, Los Alamos National Laboratory Report LA-9974-T, (1984).
- [Bu-86] G. R. Burleson *et al.*, *Nuc. Instr. Meth.*, **A247**, 327 (1986).
- [Bu-un] G. R. Burleson and J. F. Amann, computer program CROSS (unpublished).
- [Ca-79] B. Chabloz *et al.*, *Phys. Lett.*, **81B**, 143 (1979).
- [Co-80] W. B. Cottingham *et al.*, *Phys. Rev. Lett.*, **45**, 1828 (1980).
- [De-82] D. Dehnard, *Nuc. Phys.*, **A374**, 377 (1982).
- [Dh-85] K. S. Dhuga *et al.*, *Phys. Rev. C*, **32**, 2208 (1985).
- [Dh-87] K. S. Dhuga *et al.*, *Phys. Rev. C*, **35**, 1148 (1987).
- [Dh-88] K. S. Dhuga and D. J. Ernst, *AIP Conf. Proc.*, **163**, 484 (1988).
- [Ei-74] R. A. Eisenstein and G. A. Miller, *Comput. Phys. Commun.*, **8**, 130 (1974).
- [Ei-80] J. Eisenberg and D. Koltun, *Theory of Meson Interactions with Nuclei*, (John Wiley and Sons, New York, 1980).
- [Ga-48] E. Gardner and C. M. G. Lattes, *Science*, **107**, 270 (1948).
- [Gr-84] S. J. Greene *et al.*, *Phys. Rev. C*, **30**, 3003 (1984).
- [He-58] W. N. Hess, *Revs. Mod. Phys.*, **30**, 368 (1958).



- [Hi-77] M. Hirata, F. Lenz, and K. Yazaki, *Ann. Phys.*, **108**, 116 (1977).
- [In-78] C. H. Q. Ingram *et al.*, *Phys. Lett.*, **76B**, 173 (1978).
- [In-82] C. H. Q. Ingram *et al.*, *Nuc. Phys.*, **A374**, 319 (1982).
- [Iv-79] S. G. Iversen, Los Alamos Scientific Laboratory Report LA-7828-T, (1979).
- [Ja-75] J. D. Jackson, *Classical Electrodynamics, 2nd ed.*, (John Wiley & Sons, New York, 1975).
- [Jo-83] M. B. Johnson and D. J. Ernst, *Phys. Rev. C*, **27**, 709 (1983).
- [Jo-83a] M. B. Johnson and E. R. Siciliano, *Phys. Rev. C*, **27**, 730 (1983).
- [Ka-86] B. Karaoglu and E. J. Moniz, *Phys. Rev. C*, **33**, 974 (1986).
- [Ki-55] L. S. Kisslinger, *Phys. Rev.*, **98**, 761 (1955).
- [Ki-84] R. R. Kiziah, Los Alamos National Laboratory Report LA-10257-T, (1984).
- [La-47] C. M. G. Lattes *et al.*, *Nature*, **159**, 694 (1947).
- [LA-80] "LAMPF Users Handbook", Los Alamos Scientific Laboratory Report MP-DO-1-UHB, (1980).
- [Li-72] M. S. Livingston, Los Alamos Scientific Laboratory Report LA-5000, (1972).
- [Li-77] M. S. Livingston, Los Alamos Scientific Laboratory Report LA-6878-MS, (1977).
- [Li-79] L. C. Liu and C. M. Shakin, *Phys. Rev. C*, **19**, 129 (1979).
- [Ma-69] P. Marmier and E. Sheldon, *Physics and Nuclei of Particles, Vol. I*, (Academic Press, New York, 1969).
- [Me-66] A. C. Melissinos, *Experiments in Modern Physics*, (Academic Press, New York, 1966).
- [Mo-82] C. L. Morris, *Nuc. Instr. Meth.*, **196**, 263 (1982).
- [Oa-87] D. S. Oakley, Los Alamos National Laboratory Report LA-10968-T, (1987).

- [Pe-87] D. H. Perkins, *Introduction to High Energy Physics*, (Addison-Wesley Publishing Company, Inc., Menlo Park, California, 1987).
- [Pr-79] B. M. Preedom *et al.*, *Nuc. Phys.*, **A326**, 385 (1979).
- [Re-85] R. P. Redwine, *Nuc. Phys.*, **A434**, 239 (1985).
- [Ro-78] C. Rowe, M. Salomon, and R. H. Landau, *Phys. Rev. C*, **18**, 584 (1978).
- [Th-77] H. A. Thiessen *et al.*, Los Alamos Scientific Laboratory Report LA-6663-MS, (1977).
- [We-82] D. L. Weiss and D. J. Ernst, *Phys. Rev. C*, **26**, 605 (1982).
- [Yu-35] H. Yukawa, *Proc. Math. Soc. of Jap.*, **17**, 48 (1935).

## VITA

Michael Paul Snell was born in Evanston, Illinois, on August 6, 1961, the son of James Byron and Bette Lou Snell. After completing his education at J.L. McCullough High School, The Woodlands, Texas, in 1979, he entered Texas A & M University in College Station, Texas, where he received the degree of Bachelor of Science in Nuclear Engineering in May, 1983. In August, 1983 he completed Officer Training School in San Antonio, Texas, and was commissioned a Second Lieutenant in the United States Air Force. He was assigned to the Advanced Weapons Office of the Air Force Weapons Laboratory at Kirtland Air Force Base, Albuquerque, New Mexico, where he conducted theoretical studies and experimental efforts in plasma physics and neutral and charged particle beam research. He married Ginger Marie Boehm of Schulenburg, Texas in June, 1984 and his daughter, Casey Jo, was born in June, 1987. In January, 1988 he left the Weapons Laboratory to enter the Graduate School of The University of Texas.

Permanent address: 31018 Cripple Creek Drive North,  
Magnolia, Texas 87355

Current address: United States Air Force Academy, Department of Physics,  
Colorado Springs, Colorado 80840

This thesis was typed by Michael P. Snell.